FEDERAL UNIVERSITY OF ESPÍRITO SANTO
TECHNOLOGY CENTER
GRADUATE PROGRAM IN ELECTRICAL ENGINEERING

LAURA SUSANA VARGAS VALENCIA

SENSOR-TO-BODY CALIBRATION PROCEDURE AND DEFINITION OF ANATOMICAL REFERENCES FOR GAIT ANALYSIS BASED ON INERTIAL SENSORS

VITÓRIA
2015

LAURA SUSANA VARGAS VALENCIA

SENSOR-TO-BODY CALIBRATION PROCEDURE AND DEFINITION OF ANATOMICAL REFERENCES FOR GAIT ANALYSIS BASED ON INERTIAL SENSORS

Dissertation submitted to the Graduate Program in Electrical Engineering from the Technology Center of the Federal University of Espírito Santo, as partial requirement for obtaining Master's Degree in Electrical Engineering

Advisors

Prof. Dr. Anselmo Frizera Neto

Prof. Dr. Teodiano Freire Bastos Filho

VITÓRIA

2015

LAURA SUSANA VARGAS VALENCIA

SENSOR-TO-BODY CALIBRATION PROCEDURE AND DEFINITION OF ANATOMICAL REFERENCES FOR GAIT ANALYSIS BASED ON INERTIAL SENSORS

Dissertation submitted to the Graduate Program in Electrical Engineering from the Technology Center of the Federal University of Espírito Santo, as partial requirement for obtaining Master's Degree in Electrical Engineering

Committee:

Data: June 2015

_____

Prof. Dr. Anselmo Frizera Neto
Advisor. Graduate Program in Electrical Engineering, Federal University of Espirito Santo

_____

Prof. Dr. Teodiano Freire Bastos Filho
Co-Advisor. Graduate Program in Electrical Engineering, Federal University of Espirito Santo

_____

Prof. Dr. Eduardo Rocon de Lima
Neuroengineering and Cognitive Science Group, CSIC, Madrid, Spain.

_____

Prof. Dr. Klaus Fabian Côco
Electrical Engineering Department, Federal University of Espirito Santo

VITÓRIA

2015

Acknowledgments

Firstly, I would like to thank God for allowing me to reach one more achievement in my life.

I would like to thank my parents and my brother for their unconditional love, support and for always telling me not to give up.

My kinder thanks to a special person who encouraged me in the most difficult moments, by supporting me, sharing many great and happy moments in Brazil and helping me to finish this Dissertation.

My best regards to my friends Ana Cecilia and Astrid, my family in Brazil, for their friendship and always cheer me up.

I would like to thank my advisors, Dr. Anselmo Frizera Neto and Dr. Teodiano Bastos Filho, for their guidance, patience and friendship. Also for giving me the opportunity to work in the Intelligent Automation Laboratory group (Laboratorio de Automação Inteligente -LAI) and for trusting in my work.

Thanks to all my other friends, Javier, John Jairo, Sammy, Manuel, Hamilton, Nicolas, Denis and my colleagues and family, and all those who directly or indirectly contributed to this work.

Abstract

Recently, inertial measurement units (IMU) are placed on the human body segments in order to estimate joints kinematics. A fundamental issue in human gait analysis based on IMUs is that sensors' local references frames are misaligned with anatomically-defined body-segments' frames. Thus, this M.Sc. Dissertation proposes the development of a calibration procedure to address the problem of sensor-to-body alignment in order to estimate joint angular kinematics during free walking.

The novel, simple and fast calibration procedure provides tridimensional kinematics of hip, knee and ankle using only four IMUs, without resorting to any additional tools or predefined movements. A method for static assessment of the IMUs was conducted in order to determine the initial state of the system. The algorithms to align the sensors to the body segments, to calculate the joint angles and to detect events such as heel strike and toe off are also presented.

Experiments were performed with five healthy subjects and the results were compared with similar studies found in the literature. The results presented low standard deviations, which means that estimated measures were consistent across trials. The angular patterns are coherent and consistent with those presented in the literature.

This procedure also presents the potential to become an alternative to high-cost camera-based systems allowing the possibility of performing the analysis of human gait in external environments with clinical application in the near future.

Keywords: IMU, gait analysis, sensor-to-body calibration procedure, joint angles.

Resumo

Recentemente, unidades de medição inercial (IMU) são colocadas nos segmentos do corpo humano a fim de estimar a cinemática das articulações. Uma questão fundamental na análise da marcha humana baseado em IMUs é que os sistemas coordenados locais dos sensores estão desalinhados com os sistemas coordenados anatômicos dos segmentos do corpo. Assim, a presente dissertação de Mestrado propõe o desenvolvimento de um procedimento de calibração para resolver o problema de alinhamento do sensor-ao-corpo, a fim de estimar a cinemática angular das articulações durante a marcha livre.

O procedimento de calibração novo, simples e rápido de executar, fornece a cinemática tridimensional do quadril, joelho e tornozelo usando apenas quatro IMUs, sem recorrer a ferramentas adicionais ou movimentos pré-definidos. Um método para a avaliação estática dos IMUS foi conduzido a fim de conhecer o estado inicial do sistema. Os algoritmos para alinhar os sensores aos segmentos corporais, calcular os ângulos de articulações e detectar eventos tais como o contato inicial e retira do pé também são apresentados.

Os experimentos foram realizados com cinco sujeitos sem deficiência da marcha e os resultados foram comparados com estudos semelhantes na literatura. Os resultados apresentaram desvios padrão baixos, o que significa que as medidas estimadas foram consistentes em todos os testes. Os padrões angulares são coerentes e consistentes com aqueles apresentados na literatura.

Este procedimento também apresenta potencial para se tornar uma alternativa dos sistemas baseados em câmera de alto custo, permitindo a possibilidade de realizar a análise da marcha humana em ambientes externos com aplicação clínica no futuro próximo.

Palavras chave: IMU, análise da marcha, procedimento de calibração sensor-ao-corpo, ângulos das articulações.

Resumen

Recientemente, unidades de medición inercial (IMU) se colocan en los segmentos del cuerpo humano con el fin de estimar la cinemática de las articulaciones. Un problema fundamental en el análisis de marcha humana basado en IMUs es que los sistemas coordenados locales de los sensores no están alineados con los sistemas coordenados anatómicos de los segmentos del cuerpo. Por lo tanto, en esta tesis de Maestría se propone el desarrollo de un procedimiento de calibración para abordar el problema de alineación del sensor al cuerpo, con el fin de estimar la cinemática angular de las articulaciones durante marcha libre.

El procedimiento de calibración novedoso, sencillo y rápido proporciona la cinemática tridimensional de la cadera, la rodilla y el tobillo usando sólo cuatro IMUs, sin recurrir a herramientas adicionales o movimientos predefinidos. Inicialmente, se llevó a cabo un método de evaluación estática de los IMUs, con el fin de conocer el estado inicial del sistema. También se presentan los algoritmos para alinear los sensores a los segmentos corporales, calcular los ángulos de las articulaciones y detectar eventos tales como el contacto inicial y despegue del pie.

Se realizaron los experimentos con cinco sujetos sin discapacidades de marcha y los resultados se compararon con estudios similares en la literatura. Los resultados presentaron desviación-estándar baja, lo que significa que las medidas estimadas fueron consistentes entre los ensayos. Los patrones angulares son coherentes y consistentes con los presentados en la literatura.

Este procedimiento también presenta el potencial para convertirse en una alternativa a los sistemas de alto costo basados en cámaras permitiendo la posibilidad de llevar a cabo el análisis de la marcha humana en ambientes externos con aplicación clínica en un futuro cercano.

Palabras clave: IMU, análisis de marcha, procedimiento de calibración sensor-a-cuerpo, ángulos de las articulaciones.

List of Figures

List of Tables

List of Abbreviations and Acronyms

AARM	Acceleration, Angular Rate and Magnetic
AF	Anatomical Frame
AL	Anatomical Landmarks
BAF	Bone-embedded Anatomical Frame
BF	Technic-anatomical frame
CAN	Controller Area Network
CAST	Calibration Anatomical System Technique
COM	Center Of Mass
CP	Cerebral Palsy
CS	Coordinate System
DANE	Departamento Administrativo Nacional de Estadística, Colombia.
DB	Distal Body segment
DCM	Direction Cosine Matrix
DoF	Degree Of Freedom
EKF	Extended Kalman Filter
EMG	Electromyography
ETS	Electromagnetic Tracking System
EXP	Expected angle
FE	Flexion – Extension
FT	Foot
FOV	Field Of View
GA	Gait Analysis
G-CS	Global Coordinate System
GF	Global Frame
GRF	Ground Reaction Force
GT	Greater Trochanter
HS	Heel Strike
IBGE	Instituto Brasileiro de Geografia e Estatística, Brasil.
IC	Inter-IMU Consistency
IHA	Instantaneous Helical Axis
IMU	Inertial Measurement Unit

IMU-F	IMU Frame
ISB	International Society of Biomechanics
JCS	Joint Coordinate System
LAMB	Laboratorio per l'Analisi del Movimento nel Bambino
LE	Lateral femoral Epicondyle
LF	Local Frame
MARG	Magnetic, Angular Rate and Gravity
MEMS	Microelectromechanical Systems
MIMU	Magnetic and Inertial Measurement Unit
NWS	Non-wearable Systems
OA	Osteoarthritis
PB	Proximal Body segment
PD	Parkinson Disease
PV	Pelvis
QTM	Qualisys Track Manager
RA	Rheumatoid Arthritis
RF	Radio Frequency
SC	Self-IMU Consistency
SCI	Spinal Cord Injury
SH	Shank
SU	Sensor Unit
TF	Technical Frame
TH	Thigh
TO	Toe Off
ToF	Time-Of-Flight
VCM	Vicon Clinical Manager
WS	Wearable Systems

List of Symbols

α	Rotation angle around axis x
β	Rotation angle around axis y
γ	Rotation angle around axis z
g	Gravity vector
ω	Angular velocity
θ	Rotation angle around Euler axis (or other axis if specified)
e_1	Fixed axis of proximal body segment
e_2	Fixed axis of distal body segment
e_3	Floating axis
$d_{i,j}$	Difference quaternion between i-th and j-th IMU
$p_{i,k,j}$	Orientation difference between i-th and k-th IMU during j-th box pose
n̂	Euler axis
G_i	Global frame measured by i-th sensor
L_i	Local frame measured by i-th sensor
$J1$	Joint 1
$J2$	Joint 2
S1	Segment 1 (associated with semi-sphere 1)
S2	Segment 2 (associated with semi-sphere 2)
q_i	i-th element of quaternion vector
${}^{A}q_{B}$	Orientation quaternion of B with respect to A
FT	Foot
PV	Pelvis
SH	Shank
TH	Thigh

Contents

Chapter 1. Introduction and Motivation

1.1. Human Locomotion

Walking is the body's natural means of locomotion that involves a change in place, position, and posture relative to some point in the environment (HAMILL; KNUTZEN, 2009). This results from a process that involves the central nervous system, peripheral nerves, muscles, bones and joints (WHITTLE, 2007). Other locomotion modalities include climbing stairs and running. Although walking is the most habitual and essential activity for daily life and social participation, this activity is a complex dynamic task. Its learning takes place in successive stages; consequently, each person shows particular characteristics (MONTERO-ODASSO et al., 2009). The capacity to performance activities of daily living, such as walking, determines a person's functional ability (SENDEN et al., 2012). Also, gait pattern reflects the ability to develop independently in the community.

Gait analysis (GA) is the application of anatomical and biomechanical principles to understand and characterize systematically the human locomotion (WINTER, 2009). Researchers use a variety of techniques to determine kinematic, kinetic and metabolic parameters, muscles mechanics and electromyography according to the applicability.

1.2. Factors Affecting Human Locomotion

Nowadays, there is a global concern over the increasing of elderly population. The document World Population Ageing 2013 (UNITED NATIONS, 2013) reported that older people (aged 60 years or over) increased 2.5 per cent from 1990 to 2013. Such population will continue to grow. Specifically in Brazil and Colombia, older people represent 7.4 per cent (IBGE, 2010) and 2.4 per cent (DANE, 2005) of total population, respectively. This situation warns especially to health workers. Falls, immobility and neurodegenerative disorder include the major causes of disability in elderly people. Age influences in the clinical progression of diseases such as Parkinson disease (PD). PD is a degenerative disorder that affects the central nervous system. Its earlier symptoms detected are movement-related, including shaking and

disturbance of gait. Gait studies have been used to estimate characteristics of Parkinson such as: harshness of tremor, dyskinesia and bradykinesia (TIEN; GLASER; AMINOFF, 2010).

Other disorders and accidents that lead to motor impairments are stroke and spinal cord injury. Stroke or cerebrovascular accident is a brain damage due to blood supply stops flowing to the brain. This condition causes neurons' death leading to permanent neurological damage and malfunction of the brain area affected. Usually, people suffering stroke have one or more limbs paralyzed in one side of the body. This condition affects profoundly velocity and symmetry of gait (HSU; TANG; JAN, 2003). Physiotherapists spend considerable time attempting to restore patients' movement, particularly walking ability. In these scenarios, researchers propose the use of robotic devices in order to avoid fatigue (BÔRTOLE, 2014). Thus, the application of these technologies requires a detailed analysis of biomechanical parameters which implies the use of GA tools (LAUDANSKI, BROUWER; LI, 2013).

Patients that suffered a spinal cord injury (SCI) require significant rehabilitation treatment to restore gait function and recover the capacity to performance its daily living activities. A recent study was focused on the biomechanics of gait in patients with central cord syndrome. Such a study helped to understand how this injury affects gait pattern and underscore the importance of GA as a tool to decide surgical or orthopedic intervention (GIL-AGUDO et al., 2011).

On the other hand, conditions during pregnancy, birth or after birth (up to about age three) could affect the good development of infant brain and provoke problem with GA. For example, cerebral palsy (CP) causes physical disability mainly in the areas motion-related. The most common symptoms of this disorder are involuntary movements, spasticity, balance problems and unsteady gait. Depending on the severity of the disorder, physical or occupational therapy could present improvement in the results. Recent researches reported the remarkable performance of GA in the treatment of cerebral palsy. Preoperatively this tool could help to make decision of surgical intervention and assess specific pathologies. Postoperatively GA is used to assess of outcome quantitatively (CIMOLIN et al., 2011).

Rheumatoid arthritis (RA) and osteoarthritis (OA) are other degenerative disorders that involve degradation and/or inflammation of joints. The underlying bone and cartilage also are affected causing pain and movement problems. The causes of these diseases are not completely understood. However they could be associated with genetics and environmental factors. Recently it was reported that unhealthy habits as smoking is a risk factor for RA

(SUGIYAMA et al., 2010). Generally, symptoms include joint pain, stiffness, tenderness and locking. Patients with RA manifest inflammation signs which are less prominent in OA (referred to as non-inflammatory problems of the joints). The treatment of these patients involves the use of analgesics and change habits and lifestyles. Also, includes combination of exercises and occasionally joint replacement surgery. Different researches used gait analysis in patients with RA to estimate both static and dynamic lower limb functional disability and improvement after treatment (BAAN et al., 2012; SINGH et al., 2012; PARVATHY; MASOCHA, 2013; METSIS et al., 2013).

Other condition associated with mobility issues is the loss of a body part by amputation. The causes include an injury, illness or surgery. The complete loss of a limb requires the use of prosthesis because a permanent disability occurs. Also, amputated patients should undergo to rehabilitation after surgery in order to regain highest possible level of motor function. The restoration of locomotion and improvement of gait pattern is closely related to the technology of prosthesis. Designers face challenges as amputees' balance, dynamic of activities such as staircase walking or gait on inclined plane, wear material, esthetics, comfort and costs. Recent researches applied gait analysis to predict, evaluate and analyze faults in orthopedic prostheses (OLIVARES et al., 2010; OLIVARES et al., 2011; HERNÁNDEZ-CASTILLO; ÁLVAREZ-CAMACHO; SÁNCHEZ-ARÉVALO, 2013; BOFFANO et al., 2014).

1.3. The Use of Gait Analysis

Aforementioned mobility diseases alter biomechanical features that define a healthy gait pattern, and these changes lead to dysfunctional or pathological gait. In this context, clinical professionals and researchers use gait analysis to identify abnormalities and potential problems caused by such diseases. Different studies recognized GA as a clinically helpful tool to assist diagnosis, help to find the best treatment and give feedback to clinicians (Figure 1.1).

A recently research by Benedetti et al. (2011) exposes that gait analysis could also make the clinical decision less arbitrary and more objective in the assessment and diagnosis of excessive ankle plantar flexion (equinus foot) in CP patients. Using both clinical evaluation and instrumented gait analysis, the aim of the study was to define the types of equinus foot. Experimental protocol involved twenty patients and researchers clarify that each patient could

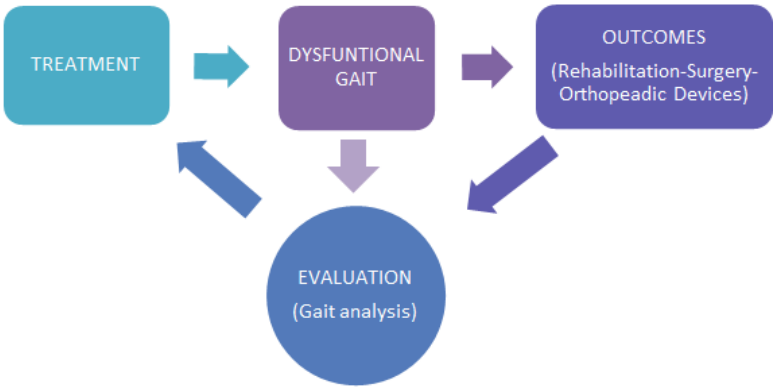

Figure 1.1 Performance of Gait analysis in a clinical scenario.

present more than one form of equinus. Considerable agreement was found between both assessment forms, matching 50 out of the 61 defined types. Authors conclude that gait analysis is useful to distinguish among different equinus types. This is important in clinical rehabilitation, because it allows a correct and objective diagnosis tool to choose the most suitable intervention or treatment.

Wren et al. (2009) expose the effects of clinical GA on the cost of care and the amount of surgeries practiced in ambulatory children with CP. The study presents the comparison between two groups of patients with CP that had been intervened with surgery. Group 1 (G1: $N = 313$) represents those that had undergone to GA before their index surgery and group 2 (G2: $N = 149$) those had not. The results evidence less subsequent surgery in G1-patients with 11% of patients who required additional surgeries compared to 32% presented in G2-patients. This situation also implies more additional surgeries per person-year (G2: 03/person-year, G1: 0.1/person-year) resulting in additional cost (G2: $3009/person-year, G1: $916/person-year). In conclusion, clinical GA is related with a lower rate of additional surgical intervention helping to reduce disruption to the patients' lives even though the cost of the first surgery were higher in G1-patients (G1: $43,006, G2: $35,215).

Fuller et al. (2002) conducted a research to determine the impact of practicing gait analysis on surgical planning in adult patients with spastic equinovarus deformity. These gait-dysfunctional patients are characterized by having one or both feet rotated internally at the ankle. The study involved thirty-six patients and two surgeons formulated independently surgical plans before applying GA. After this process, an experienced physiatrist collected kinetic, kinematic and EMG data. The results show that 64% of surgical plans changed after

gait study and the agreement between independent surgical plans increased from 0.34 to 0.76. This shows how GA may alter surgical decision- making.

Despite the studies demonstrate gait analysis effectiveness, there are some challenges to make GA widely accepted as a routine in clinical diagnoses. Among the most mentioned barriers and limitations are: the maturity of technology (including variability, accuracy and reproducibility related to technical factors), cost-effectiveness, flexible and friendly use and time-consumption to drive tests and interpret data (SIMON, 2004).

Optical camera systems are the current and standard technology used to estimate position and orientation of human limbs. Along with force platforms, they constitute specialized gait laboratories. Using these technologies both kinematic and kinetic parameters could be estimated with high accuracy. However, these technologies present some limitations: they are expensive, present reduced portability, restrict the study to a controlled laboratory environment and require dedicated and experienced personnel.

Alternatively, wearable sensor systems (WS), which are used in this dissertation, with evident cost, usability and flexibility advantages may offer real-time motion analysis. This technological advancement offers to clinical area a solution to those principal hampering factors avoiding complex set-ups and use without specific environment limitations. Muro-de-la-Herran et al. (2014) conducted a review of thirty two articles published from 2012 to 2013 about original research in gait analysis. 40% of articles were related to non-wearable systems (NWS), 37.5% related to inertial sensor-based systems and 22.5% regarding other WS. According to the authors, trends in the gait analysis area evidently suggest more development of WS including calibration, signal processing and data analysis algorithms in order to accomplish better accuracy and repeatability. Also, the authors insure that inertial sensors are the most promising and widely used WS in recent researches.

From now on in this dissertation, the terminology IMU (inertial measurement unit) will be referred as a device comprised of multi-axis accelerometers, gyroscopes and magnetometers, although some authors use other terms instead of IMU to refer to those sensors that include magnetometers, such as MIMU (Magnetic and Inertial Measurement Unit) (FAVRE et al., 2009; PICERNO; CEREATTI; CAPPOZZO, 2011; PALERMO et al., 2014) or MARG (Magnetic, Angular Rate and Gravity) (PICERNO; CEREATTI; CAPPOZZO, 2008; GALINSKI; DEHEZ, 2012; QIU et al. 2014).

Different accomplishments in gait analysis based on inertial sensors have been reported in the last years. A wearable sensor network based on accelerometers was used to monitor patients with Parkinson's disease. The researchers focused on the evaluation of motor status of patients. The study involved ninety-two Parkinson disease (PD) patients and twenty healthy subjects, which undergone to gait assessment in different versions improved of the system. The system, called PERFORM, provides a very moderate assessment of patients performing their daily activities (PASTORINO et al., 2013).

Van den Noort et al. (2013) reported a preliminary validation of Outwalk protocol (CUTTI et al., 2010) thought gait analysis of six children with cerebral palsy. Using inertial and magnetic sensors (Xsens Technology, NL), 3D joint kinematics were estimated. Results show significant differences in frontal and traversal plane due to offsets. Authors associate these offsets to problems related to protocols' anatomical calibration process. Finally, they suggest that posterior studies should be pointed to improve anatomical calibration of the sensors in application that involve children with cerebral palsy (CP).

Merchán-Baeza et al. (2014) used inertial sensors (InertialCube3TM, InterSense Inc, USA) to analyze the reliability in the Functional Reach Test (FRT) parameterization in five stroke patients. Clinicians use this test to estimate the semi-static balance of a person performing trunk displacement. This approach integrates biomechanics concepts including postural control to infer the chance of falling. Authors conclude that inertial sensors are a specific and reliable tool for this task.

In conclusion, gait analysis based on inertial sensor could benefit a variety of research and clinical practices including rehabilitation assessment, diagnose of motion disorders, continuous monitoring of patients and improving orthosis and prosthesis design. This leads to a wide field of research to develop better technologies, define more appropriated measurement protocol and provide different data processing and calibration techniques.

The sensor-to-body calibration procedure is a fundamental part of IMU-based gait analysis. IMU sensors are placed on the body segments in order to measure joint kinematics. To calculate the joint angles, the orientation of two adjacent segments is required. Each inertial sensor measures its orientation using a global coordinate system (G-CS) as reference, but they need to be aligned with the body segment frame in order to produce a correct measurement.

1.4. Objectives

Such as aforementioned, the core of currently gait analysis lies in the measurement of joint kinematics and kinetics. Perhaps, the kinematic parameter, which has a major interest in the gait study, is the joint angular displacement. On the other hand, IMU-based joint angle estimation requires alignment of the sensors to the body segments to produce correct measurements. Thus, the general objective of this research is to provide a sensor-to-body calibration procedure to align the sensor to the body segment coordinates system. This is an important task in order to detect and characterize 3D joint kinematics for gait analysis based on inertial sensors (IMUs). The aim of this dissertation is based on the following hypothesis: *Through the alignment of the sensors to body segment frames, is it possible to estimate the lower limb joint angles placing at least one inertial sensor in each body segment, namely foot, shank, thigh and pelvis*? More specifically the objectives of the dissertation are summarized as follows:

- To propose a suitable protocol to sensor placement.
- To study the background of different techniques to align the sensor placed on each body segment.
- To develop a sensor-to-body calibration algorithm and define technic-anatomical references in order to estimate joint angles of the ankle, knee and hip in healthy subjects.
- To develop an algorithm to calculate the joint angles.
- To validate the preliminary results according to the viewpoint of a specialist and by comparison with results of similar studies in the literature.
- To provide an easy and flexible tool for gait analysis to be used in external environments with clinical application in near future.

1.5. Organization of the Document

This M.Sc. dissertation is divided in six chapters: Chapter 1 exposes the motivation of this dissertation and a general introduction of clinical application, challenges, opportunities and trends of gait analysis (GA). The research objectives are also presented. Chapter 2 contains the overview of gait key parameters, methods and the state of the art in gait analysis including inertial sensors (IMUs) and background of sensor-to-body calibration techniques. Chapter 3 exposes methods and materials including the description of the used system, a short discussion of mathematical representation of rotations in 3D-space (Quaternions vs., Euler), the sensor-placement protocol and the explanation of the calibration procedure proposed to estimate lower-limb joint kinematics. Chapter 4 contains general simulations and the experimental validation divided in four subsections: the static assessment of simulated and real inertial sensors and the calibration procedure applied to two-semi sphere and goniometer simulated and real configuration. Chapter 5 provides the experimental protocol to estimate kinematic parameters in healthy volunteers the results and discussion. Finally, Chapter 6 presents the conclusions and future work.

Chapter 2. Gait Analysis and State of the Art

2.1. Description of Human Gait

From biomechanics, human gait is the forward displacement of the center of gravity, and in non-disability conditions, consists of keeping balance by moving harmonically the trunk and lower limbs. Its analysis involves the study of the body segments motion through time and space from one position to the other. A complete description of human gait includes kinematic and kinetic data. Gait could also be understood as a chain of successive events that means a cyclic pattern of movement repeated over time (VAUGHAN; DAVIS; O'CONNOR, 1999). A gait cycle is the basic unit to characterize the way of walking, assuming that successive cycles will be reasonably similar if not the same. This cycle is subdivided in two main phases (Figure 2.1):

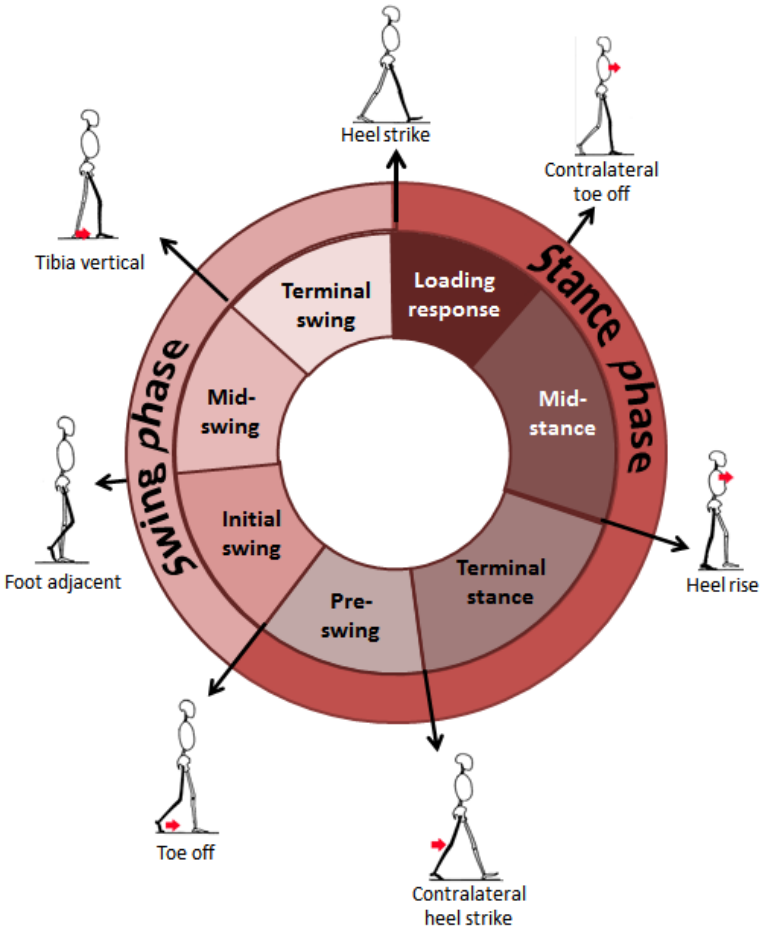

Figure 2.1 Gait phases and events. (Source: Adapted from WHITTLE, 2007).

1. Stance phase (approximately 60% of the gait cycle), when the foot is in contact to the ground and
2. Swing phase (approximately 40% of the gait cycle), when the same foot is not in contact with the ground and the leg is moving forward preparing the next contact.

Each phase is subdivided in periods (WHITTLE, 2007; TAO et al., 2012). Stance phase or "support phase" comprises the following periods.

1.1. Loading response: This is the initial double-limb support period. Beginning with initial contact (heel strike) until the other foot leaves the ground (contralateral toe off) prepared to swing. The hip is flexed, the knee is flexing until peak knee flexion for shock absorption and the ankle plantar flexion limits the heel rocker due to forefoot touches the floor. At the end of this stage, body weight is completely transferred onto the stance limb.

1.2. Mid-stance: This is the half of the single-limb support period. This period begins with the contralateral toe off and ends when body weight is aligned over the forefoot. While the hip and knee are extending, the goal is the advance of the body over the stationary foot by ankle dorsiflexion (second rocker).

1.3. Terminal stance: This period completes the single-limb support. The interval begins with heel rising (leaving the ground) until contralateral heel strike. The hip and the knee extend until the limit and start flexion. In this period the body advances through the forefoot rocker.

1.4. Pre-swing: This is the second double-limb support. Beginning with the contralateral heel strike until the foot leaves the ground (toe off). The hip and knee are flexing. The ankle keeps a movement of plantar-flexion. This interval is to prepare for swing.

The swing phase is subdivided into the following periods.

2.1 Initial swing: This is approximately one-third of swing phase. This interval begins with the toe off and ends when the swinging limb is opposite to stance limb; in this instant, the knee joint gets the maximum flexion. The hip is flexing and the limb advances.

2.2 Mid-swing: This is the second-third of the swing phase. This period begins following the maximum knee flexion and ends when the swinging limb is forward and the tibia is in a vertical position. The hip continues flexion and the knee extends in regards to gravity, the ankle continues dorsiflexion to ends neutral.

2.3 Terminal-swing: This last interval begins with a vertical tibia and ends with heel strike preparing for next step. The shank moves ahead of the thing through the knee fully extension. The hip is flexed and the ankle remains in dorsiflexion to neutral.

In the previous information, seven events were mentioned, which subdivide the gait cycle in periods (WHITTLE, 2007): 1) Initial contact or heel strike, when the heel contacts with the ground; 2) Contralateral toe off, this is toe of on the other foot; 3) Heel rise, also called “heel off”, when the heel begins to lift from the ground; 4) Contralateral heel strike, this is a heel strike on the other foot; 5) Toe off, when the foot leaves the floor; 6) Foot adjacent, this is the time at which the swinging limb passes the stance limb; and 7) Tibia vertical, when the tibia of swinging limb corresponds with the vertical.

From this general description, the gait study can be usually approached from two perspectives: the study of kinematics and/or kinetics. Kinematics is understood how the study of the motion of bodies without consideration of the causes that produce it. On the other hand, kinetics is the study of the relationship between the movement of bodies and its causes, namely forces and torques.

2.1.1. Kinematics

A variety of parameters could be expressed in terms of percentage of the gait cycle. According to the scope of this dissertation, these parameters only consist of those related to displacements, velocities and accelerations, specifically the lower limb joint angles. Key parameters such as gait speed, step length, stride length and cadence are explained in Table 2.1.

Table 2.1 Key parameters of human gait.

Parameter	Description
Gait average speed (m/s)	Distance traveled by the full body in a time period. According to Whittle (2007). $speed\ \left(\frac{m}{s}\right) = stride\ length\ (m) \cdot \frac{1}{120} cadence\ \left(\frac{steps}{mins}\right)$
Step length (m)	Linear distance between both feet when are in contact with the floor (Figure 2.2).

Stride length (m)	Linear distance between two successive placements of the same foot, that means two step lengths.
Cadence (steps/min)	Number of steps per time unit.

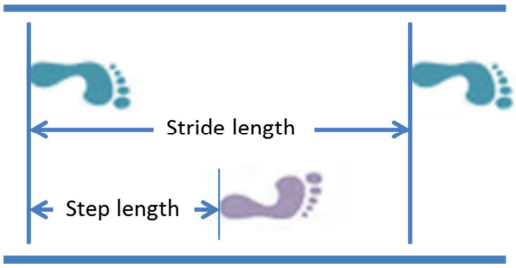

Figure 2.2 Step and stride. A stripe is equivalent to two steps.

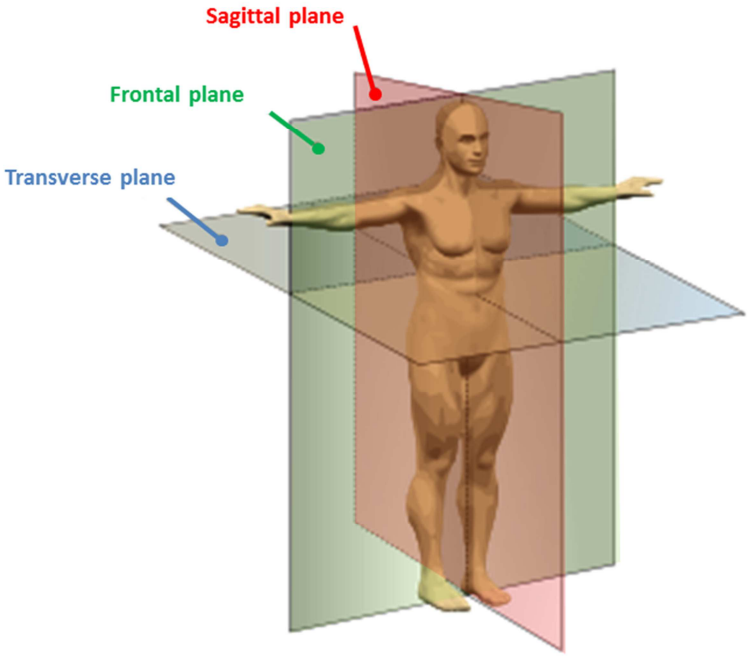

Figure 2.3 Sagittal, frontal and transverse plane (Source: WHITTLE, 2007).

Angular displacements: In a gait study, angular displacements of the body segment axes are ones of the kinematic parameters of most interest. These angular displacements are experimented on three reference planes (Figure 2.3). The sagittal plane divides symmetrically the body through the vertical, into right and left sides. The frontal plane (or coronal plane) divides the body into front (anterior) and back (posterior) portions. Finally, the transverse plane (or horizontal plane) divides the body into superior (cranial) and inferior (caudal) portions. The directions of the lower limb joint movements in there three planes are shown in Figure 2.4.

Once the joint angles are estimated during a gait cycle, key points from the curves could be selected to evaluate the way of walking, these point are called discrete angular kinematic parameters previously reported by Benedetti et al. (1998). These parameters allow a better comparison and detailed analysis of joints.

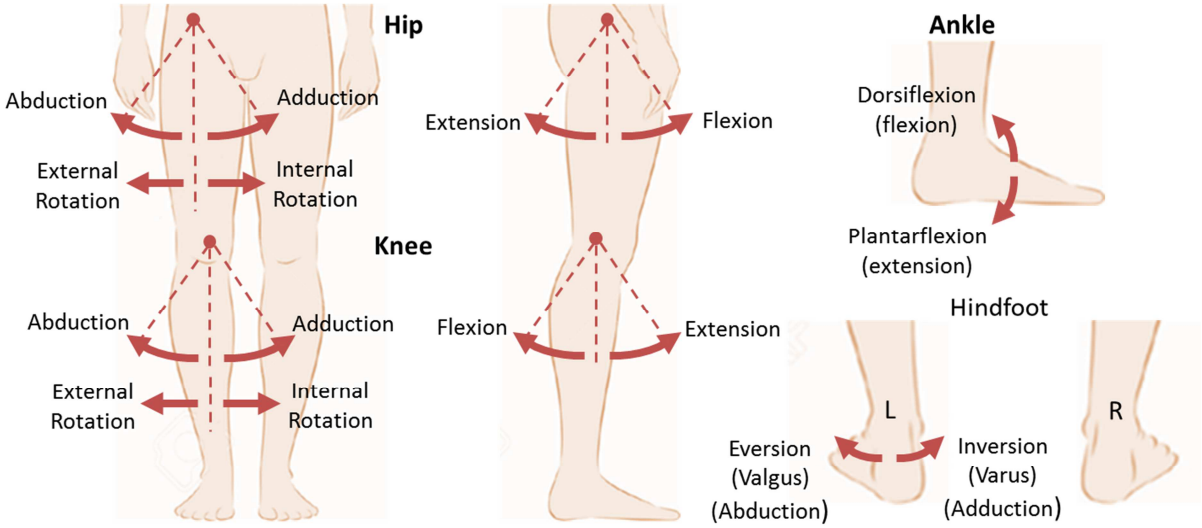

Figure 2.4 Hip, knee and ankle joint motion. (Source: Adapted from WHITTLE, 2007).

In this dissertation the joint angles of the ankle, knee and hip were estimated. For each joint discrete parameters that describe the angular displacement on a specific event (toe off or heel strike) or during a particular phase (maximum and/or minimum in stance or swing phase) are selected. These parameters are presented in Table 2.2. In Section 3.4.4 these parameters will be explained in detail.

Table 2.2 Joint angles parameter for gait analysis.

Hip angles parameters (Deg)		**Knee angles parameters (Deg)**		**Ankle angles parameters (Deg)**	
H1	Flexion at heel strike	**K1**	Flexion at heel strike	**A1**	Flexion at heel strike
H2	Max. flex. at loading response	**K2**	Max. flex. at loading response	**A2**	Max. plant. flex. at loading response
H3	Max. ext. in stance phase	**K3**	Max. ext. in stance phase	**A3**	Max. dorsiflexion in stance phase
H4	Flexion at toe off	**K4**	Flexion at toe off	**A4**	Flexion at toe off
H5	Max. flex. In swing phase	**K5**	Max. flex. In swing phase	**A5**	Max. dorsiflexion in swing phase
H6	Total sagittal plane excursion	**K6**	Total sagittal plane excursion	**A6**	Total sagittal plane excursion
H7	Total coronal plane excursion	**K7**	Total coronal plane excursion	**A7**	Total coronal plane excursion
H8	Max. add. in stance phase	**K8**	Max. add. in stance phase	**A8**	Max. eversion in stance phase
H9	Max. abd. in swing phase	**K9**	Max. add. in swing phase	**A9**	Max. inversion in swing phase
H10	Total transverse plane excursion	**K10**	Total transverse plane excursion		
H11	Max. int. rot. in stance phase	**K11**	Max. int. rot. in stance phase		
H12	Max ext. rot. in swing phase	**K12**	Max ext. rot. in swing phase		

2.1.2. Kinetics

In order to study the dynamics of human gait, it is imperative to know all internal and external forces and torques acting on the body. This approach is beyond the scope of this dissertation, however, the estimation of some dynamic joint parameters will be assessed in future works. This task has some high grade of complexity due to the measurement of kinetics of joints is not carried out directly with current technologies.

Therefore, these parameters could be estimated by using the kinematic data along with the position and orientation of the body segments and measuring the ground reaction force (GRF) and the point of application of this force (WINTER, 2009). Using anthropometry, the body segment lengths, centers of mass (COM) positions and its mass can be determined. Anthropometric measurements, kinematics and external forces could be inputs of the *link-segment model* (WINTER, 2009) and, using an *inverse solution*, the joint reaction forces and muscle moments could be calculated (Figure 2.5). Some assumptions are made about the model:

1. Each body segment has a constant mass located at its COM (as a point mass).
2. The location of each segment's COM doesn't change during motion.
3. The joints are assumed as hinge (or ball-and-socket) joints.
4. The moment of inertia of each segment about its mass center (or about either proximal or distal joints) is constant during motion.
5. The each segment length is constant during motion.

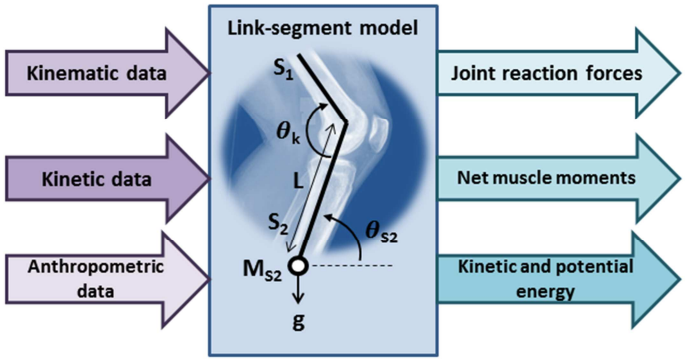

Figure 2.5 Schematic diagram using an inverse solution of a link-segment model to calculated moments and forces. (Source: Adapted from WINTER, 2009).

2.2. Gait Analysis: Non-wearable and Wearable Systems

Through this document, different approaches of gait analysis have been mentioned. From the perspective of methods, techniques and technologies applied, Muro-de-la-Herran et al. (2014) proposed the following system classification: Non-wearable (NWS) and wearable (WS) systems. NWS are those that work in controlled, specialized and delimited spaces. These present a higher cost, requiring fixed instrumentation and complex set-ups. On the other hand, WS can be used in external environments, presenting relatively lower costs. In addition, due to its condition of portability, these sensors may be placed on the body in a simpler way.

NWS are those based on optical processing and floor sensors. The optic sensors used include analog, digital and time-of-flight (ToF) cameras (MANCA et al., 2010; BOVI et al., 2011; DERAWI; ALI; CHEIKH, 2011; NGUYEN; MEUNIER, 2014), laser range scanners (CLARK et al., 2013; GIPSMAN et al., 2014) and infrared sensors (XUE et al., 2010). The type of technology and the methods applied define whether body markers are required (CESERACCIU; SAWACHA; COBELLI, 2014).

For the purpose of reconstruction and analysis of human body kinematics using multi-camera systems, stereophotogrammetry is perhaps the most sophisticated technique. Applying this technique, bone positions and orientations and relative movement between adjacent bones (joint kinematics) can be estimated. Basically, this technique consists of that infrared cameras detect a set of markers placed on the body according to gait analysis protocols. Within those protocols are some variations of the Conventional gait model (BAKER; RODDA 2003; BAKER, 2006), indicated as Newington-Gage-Davis model (DAVIS et al., 1991), the Helen Hayes model (KADABA; RAMAKRISHNAN; WOOTTEN, 1990) and the VCM (Vicon Clinical Manager) model. This latter is based on models proposed by Kadaba et al. (1989) and Davis et al. (1991). Other available protocols are LAMB (RABUFFETTI; CRENNA, 2004), CAST (CAPPOZZO et al., 1995) and the Foot model.

Most of models consider body segment as a rigid body, leaving aside the soft tissue problem. Thus, it can be assumed that all markers have a position and orientation fixed relative to associated bony segment. In such a way, technical and anatomical coordinate systems can be defined using mathematical models in order to estimate joint kinematics.

Within the floor sensors, there are the force platforms and pressure measurement systems, which are equipped with pressure and ground reaction force (GRF) sensors to measure the force applied by the subject while walking (HUNT et al., 2006; ROERDINK et al., 2008).

Moreover, WS include electro-goniometers (KUMAR et al., 2009)(SATO; HANSSON; COURY, 2010), extensometers and electromyography (EMG) (FREED et al., 2011). Also, these systems involve pressure and force sensors, such as instrumented shoes (BAE; TOMIZUKA, 2013) or insoles (DE ROSSI et al., 2011). Other systems consist of accelerometers (YANG AND HSU, 2010; YANG et al., 2011), gyroscopes and magnetometers or their combination creating inertial sensors (LUINGE; VELTINK, 2005; RODRÍGUEZ-MARTÍN et al., 2013; TADANO; TAKEDA; MIYAGAWA, 2013; ALONGE et al., 2014).

2.2.1. Commercial Gait Analysis Systems for Assessing Kinematics

Non-wearable systems: There are some examples of commercial gait laboratory and instrumentation. The most widely used are: BTS devices, integrated solutions using Vicon motion system and Qualisys along with external devices.

BTS GaitLab (Figure 2.6) is the most recently integrated laboratory from BTS Bioengineering company, Italy. It has been designed to carry out gait analysis in different environments including clinical scenarios. BTS GaitLab offers an integrated system to acquire kinematics, dynamics and EMG data. The standard equipment include, among others, a high precision optoelectronic system BTS Smart DX 6000 (8 infrared digital cameras and core), a modular sensory floor BTS P-6000 (equivalent to 4 traditional force plates) to measure ground reaction force, BTS FREEMG 1000 (8 EMG wireless probes), marker kit and a pre-installed software BTS SMART-Clinic. The walking analysis protocols available are: Davis, Helen Hayes, CAST, LAMB and foot model. The SMART-DX 6000 sensor resolution is 2.2 Megapixels, with 340 fps of acquisition frequency (at maximum resolution) and accuracy less than 0.1 mm in a 4x3x3 m^3 volume using from 3 to 20 mm markers (BTS BIOENGINEERING, 2014). Collazos and Argothy (2014) used BTS GaitLab system with six optoelectronic cameras in a research to model normal and pathological gait using kinematic parameters.

Vicon (Oxford metrics, UK) has been present in the motion capture industry for 30 years. The latest generation of Vicon optical cameras is called Bonita. Bonita B10 infrared camera (Figure 2.7) has a resolution of 1 Megapixel, a maximum frame rate of 250 fps and a precision down to 0.5 mm of translation and 0.5 degrees of rotation in a 4x4x4 m^3 volume using 9 mm markers (VICON, 2015). Its recent clinical software solutions are: Vicon Nexus, Polygon and Bodybuilder fully integrated, where each one present special features. The latest release in clinically accepted model is Plug-in Gait that preserves the VCM (Vicon Clinical Manager) features. Plug-in Gait is the Vicon implementation of the Conventional Gait Model (CGM) basing on the Newington-Helen Hayes gait model. Other partner enterprises, such as Comtemplas and Biomechanical solution (COMTEMPLAS GMBH, 2015; BIOMECHANICAL SOLUTIONS, 2015), resell integrated solution including from 4 to 16 Vicon infrared cameras, depending on the application (GRAGG; CLOUTIER; YANG 2013; CARSE et al., 2013; DI MARCO et al., 2015). Vicon systems can be integrated with force plates manufactured by AMTI, Bertec and Kistler. A configuration using 7 infrared cameras Bonita B10 was used in a research to characterize the gait of children with cerebral palsy (CELESTINO; GAMA; BARELA, 2014).

Qualisys (Qualisys AB, Sweden) offers solutions to integrate motion, force and muscle activity. Its latest release in the Oqus camera series is Oqus 7+. This camera (Figure 2.8) offers, in normal mode, a resolution of 12 Megapixels and a maximum frame rate at full resolution and full field of view (FOV) equal to 300 fps. The capture distance is up to 25 m using 19 mm markers or up to 9 m with 4 mm markers. A typical gait laboratory consists of 8 to 12 cameras covering a volume of at least 4x1.5x2 m (QUALISYS, 2015). Qualisys Track Manager (QTM) is the main software as an integral part of Qualisys' motion capture system that runs standard protocols (such a Helen Hayes) or methods and routines own user. Also, they have Visual3D (developed by one of Qualisys' partner, C-Motion, Inc), which is an analysis package to report optical 3D data. Alike Vicon solutions, QTM supports calculation of force data using force platforms from AMTI, Bertec and Kistler. Previous versions of Oqus have been used in different researches related-gait assessment, with a configuration from 6 to 12 cameras (OLSEN; ANDERSEN; PFAU, 2012: NISHIDA et al., 2015: GEERTSEN et al. 2015).

A summary of above-mentioned solutions, focusing on the sensor features to estimate joint kinematics is presented in Table 2.3.

Figure 2.6 BTS GaitLab. (Source: BTS BIOENGINEERING, 2015).

Figure 2.7 Infrared camera - Bonita B10 by Vicon. (Source: VICON, 2015).

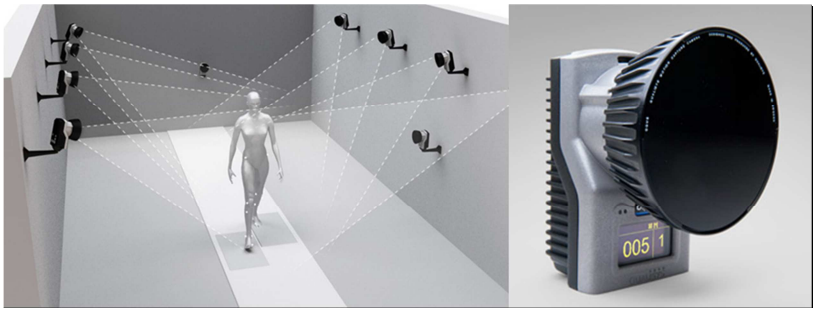

Figure 2.8 Typical Qualisys gait laboratory using Oqus 7+. (Source: Adapted from QUALISYS, 2015).

Table 2.3 Summary of the sensor features manufactured by BTS, Vicon and Qualysis.

Infrared camera features	**BTS SMART DX-6000**	**Vicon Bonita B10**	**Qualisys Oqus 7+**
Sensor resolution (MP)	2.2	1	12
Acquisition frequency (fps)	340	250	300
Accuracy (mm)	< 0.1	0.5	0.5*
Accuracy in volume (m^3)	4x3x3	4x4x4	-
Marker set - ∅ (mm)	3 to 20	9	4 to 19

* Unreported. Accuracy for previous version: Oqus 3 (DE MITS et al., 2012).

In addition, force platform and/or pressure measurement system are integrated to theses above-mentioned multi-camera system to estimate dynamic parameters. Some examples are: AMTI, Bertec and Kristle, enterprises that manufacture force plates, and Tekscan offers pressure measurement solutions. The main different between these type of force sensors is that force plates, in addition to quantify the vertical component, measure the horizontal components of the applied force. While that pressure measurement systems only quantify the pressure patterns exerted (vertical direction) by the foot on the floor over time.

Wearable systems: Different types of wearable sensors used to estimate various parameters of human body kinematics are available at global market. Some of these devices are manufactured to allow the monitoring of patients or to develop researches. The following examples include electromagnetic tracking systems (ETS), flexible goniometers and inertial sensors.

Polhemus G4 system (POLHEMUS, 2013) is the newest motion capture system commercialized by Polhemus Inc. USA (Figure 2.9). This electromagnetic tracking system (ETS) sends the position and orientation data (6DoF) to the PC via simple Radio Frequency (RF) link. Each G4 hub supports up to three sensors operating at 120 Hz. Position data are sent using Cartesian coordinates and orientation data through Euler angles or quaternions. This kind of technology requires a continuous source of magnetic field (as a magnetic transmitter) in order to track the sensors placed on the user through of G4 hub (receptor).

Perhaps the most common instrument to measure joint angles is a goniometer. Technological advances have allowed developing flexible goniometer using electric devices. Examples of these sensors are the “SG” series twin axis goniometers by Biometrics Ltd., UK (BIOMETRICS LTD, 2015). These flexible goniometers can measure angles in up to two planes of movements. The transducer type used is a strain gauge with accuracy of ± 2° over a range of ±90°. These sensors could be connected to DataLOG (data acquisition system) in order to transfer the data to the PC via Bluetooth (Figure 2.10). Mohamed et al. (2012) conducted a research using these sensors to measure knee kinematics during activities such as chair rise, gait and deep knee bends.

Figure 2.9 Polhemus G4 based on electromagnetic tracking system. (Source: Adapted from POLHEMUS, 2013).

Figure 2.10 Flexible goniometer called SG150 for knee joint. (Source: BIOMETRICS, 2015).

BTS G-WALK (BTS Bioengineering, Italy) uses an inertial sensor and it is placed on the waist to determine spatio-temporal parameters such as cadence, gait speed, stride and step length; pelvic angles are still estimated (BTS BIOENGINEERING, 2012a). This devices is projected as a clinical tool with four protocols to indicate walk and balance related problems, ability to sit and rise, monitor progression of patients and determine risk of fall. The system is an integrated platform using a 3D accelerometer (with different sensitivity from ±2 to ±16 g), a 3D gyroscope (different sensitivity from ±250 to ±2000 °/s), a 3D magnetometer (±1200 uT) and a GPS receiver with position accuracy from 2.5 to 3 m. The sensor fusion's frequency is 200 Hz and this is connected to a PC via Bluetooth. This device was compared to gold standard BTS GaitLab analyzing some parameters. Results showed a deviation of 2.28% (BTS BIOENGINEERING, 2012b).

Shadow (Figure 2.11) is a complete wireless sensor network for motion capture commercialized by Motion Workshop, USA. This wearable system is offered in three different configurations, one of those is lower body configuration that includes seven inertial sensors and pressure insoles (MOTION WORKSHOP, 2015) in order to estimate the lower limb kinematics. Also this includes software which provides a simple interface to configure the system, acquire orientation and sensor data. The system requires a wireless network controller unit that collects data from all connected sensors and sends to the PC via Wi-Fi.

Each sensor node is a combination of an accelerometer, a gyroscope and a magnetometer for each one of the three axes of measurement. Some features of interest of this system are shown in Table 2.4.

Figure 2.11 Wearable sensor network: Shadow system. (Source: Adapted from MOTION WORKSHOP, 2015).

STT-IBS (STT Systems, Spain) includes an accelerometer, a gyroscope and a magnetometer, each one of three dimensions (Figure 2.12) (STT SYSTEMS, 2013). Using Wi-Fi or Bluetooth, the system can communicate with the PC or a smart phone. The company provides a SDK in order to users can acquire the data sent by the sensor network and create own applications. Important characteristics to be compared are shown in Table 2.4.

Figure 2.12 STT IBS inertial sensor. (Source: Adapted from STT SYSTEMS, 2013).

Xsens Technologies (Netherlands) is probably the leading company of 3D motion tracking technology based on inertial sensor. Its different versions of inertial sensors are the most commonly used and commercially available. In gait analysis, the state of the art for Xsens inertial sensor is MTw (Figure 2.13). This sensor is included in the MVN Biomech system, a solution to measure 3D kinematics based on a biomechanical model. MTw is a completely wireless sensor and it is connected to Awinda Station (or Awinda Dongle) using IEEE 802.15.4. This last device receives and synchronizes data from up to 32 MTw sensors. Also,

this device charges up to 6 MTw sensors. The interface communication between Awinda and the PC is a USB port. In open space, the transmission range is up to 50 m and up to 20 m in an office space. Other sensor characteristics are shown in Table 2.4.

Figure 2.13 MTw wireless inertial sensors by Xsens. (Source: Adapted from XSENS TECHNOLOGIES, 2014).

Table 2.4 Comparing three different inertial sensors.

Sensor feature	MTw (Xsens, NL)	STT-IBS (STT System, Spain)	MotionNode – Shadow (Motion Workshop, USA)
Number of sensor (up to)	32	28	20
Dimensions W x L x H (mm)	34.5 x 57.8 x 14.5	36 x 46.5 x 15	35 x 35 x 15
Weight (g)	27	30	10
Communication Sensor-Controller unit (CU)	IEEE 802.15.4 (PHY)	IEEE 802.11 Bluetooth 2.0 (directly to the PC)	USB, Standard-A connector
Communication CU-PC	USB	-	IEEE 802.11G
Battery life (~ hours)	4 (typical)	Unreported	4.75 (15 sensors)
Transmission range indoor/outdoor (m)	20 - 50	20 - 50	32 – 95
Acceleration (g)	± 16 (full scale)	± 2 or ± 8	± 2 or ± 6
Angular velocity (°/s)	± 1200	± 2000	± 2000
Magnetic field (µT)	± 150	± 1200	± 100
Frequency rate (Hz)	50 (12 sensors)	125 – 250	100
Angular resolution (°)	0.05	< 0.1	Unreported
Static precision (°)	< 0.5 (roll/pitch) 1 (yaw)	< 0.5	0.5 to 2 (RMS)
Dynamic precision (°)	2 (RMS)	< 2	

In this dissertation, Tech IMU CAN sensors (Techanid, Spain) were used to estimate joint kinematics. A detailed description of the system will be presented in Section 3.1.

2.3. Principles of Inertial Sensors

Through the document it has been mentioned that an inertial sensor (IMU) is a combination of multi-axis sensors such as accelerometers, gyroscopes and magnetometers. With the recent progress in microelectromechanical system (MEMs), the development of these sensors smaller and lighter has been accomplished.

MEMS (Microelectromechanical Systems) accelerometers are generally piezoresistive sensors. These sensors (piezo) are composed of a mass suspended by a spring (1D). Its working principle consists of detecting an inertial force generated by the acceleration or deceleration of the proof mass. This motion causes a mechanical displacement of the elastic spring which finally restores that mass to its neutral position (ALBARBAR et al., 2008). These sensors measures two components of acceleration, one due to the effect of gravity and the other corresponds to the motion of sensor. Currently, MEMS gyroscopes are based on vibrating mass and these are used to measure angular velocities. A general configuration is composed of two masses oscillating and moving in opposite directions. If an angular velocity occurs, the Coriolis force acts on each mass also in opposite directions causing capacitance change. This capacitance change is proportional with the angular velocity (HARISH et al., 2008). MEMS magnetometers measure the magnetic field strength. Many of them operate by detecting the effect of the Lorentz force (LANGFELDER et al., 2013). Thus, these sensors rely on the mechanical motion of the MEMS structure caused by Lorentz force being exerted on the current conductor in the magnetic field. Multi-axis accelerometers, gyroscopes and magnetometers are built mounting perpendicularly the one-dimension sensors. Furthermore, gyroscopes and magnetometers present high temperature sensibility. Therefore, as an additional component of the IMU sensors, a temperature sensor should be used along with compensation algorithms to reduce this effect.

Different approaches to estimate body segment orientation and therefore estimating joint angles are presented in the literature. By using only gyroscopes, an accumulative error may be generated due to the integration of the angular velocity (TONG; GRANAT, 1999; LUINGE; VELTINK, 2005). To increase accuracy, it is suggested to add accelerometers to determine the direction of the local vertical and use fusion algorithms such a Kalman filter. Meanwhile, magnetometers may contribute with stability in the horizontal plane avoiding heading drifts, but magnetic disturbances affect highly their performance (ROETENBERG; BATEN;

VELTINK, 2007). Therefore, the effort to improve data fusion algorithms and, consequently, reduce these errors remains an important research line of many groups (CIFUENTES et al., 2012; ALFONSO, 2014). Nevertheless, the data fusion algorithms are out of scope of this work and will not be further discuss in this dissertation.

2.3.1. Sensor-to-Body Calibration Techniques

To estimate kinematic parameters, IMU sensors are placed on the body segments in order to determine their orientations respect to a global frame. Each segment of lower limb (feet, shank and thigh) and the pelvis are considered as a separate entity. These are the links of the human body model that is composed of a series of interconnected rigid links and joints in a biomechanical approach. For example, (knee) joint angles are estimated using orientation data of distal (shank) and proximal (thigh) segments. To accomplish this task, there is a need to define coordinates systems (CSs) for each segment. It is desirable that these CSs are bone-embedded frame (anatomical frame), but due to different factors, these CSs are always product of an estimate (technical frame). Within those factors are sensor errors, soft tissue artifact, geometric approximations and assumption of segment orientations during known postures.

As previously defined for optical systems, each segment is considered to present uniform geometry (Figure 2.14): the thigh and shank are assumed as cylindrical shapes and the foot as a right pyramid (VAUGHAN et al. 1999). In the study of segment's 3D motions, six coordinates are required to express its position and orientation uniquely. Three of those coordinates could be Cartesian coordinates that indicate the body segment position in the space. Other coordinates are the three angles of rotations to describe its orientation respect to a reference frame. Inertial sensors can measure kinematic parameters relating to angles, velocities and accelerations but not relative positions. Nevertheless, studies presented in (ROETENBERG; BATEN; VELTINK, 2007; VELTINK; DE ROSSI, 2010) propose automatic identification of inertial sensor placement on human body segments and estimation of sensor position using human kinematic model and anthropometry. For the purpose of this dissertation, positions of specific points, such as center of gravity of each segment, are not required**.**

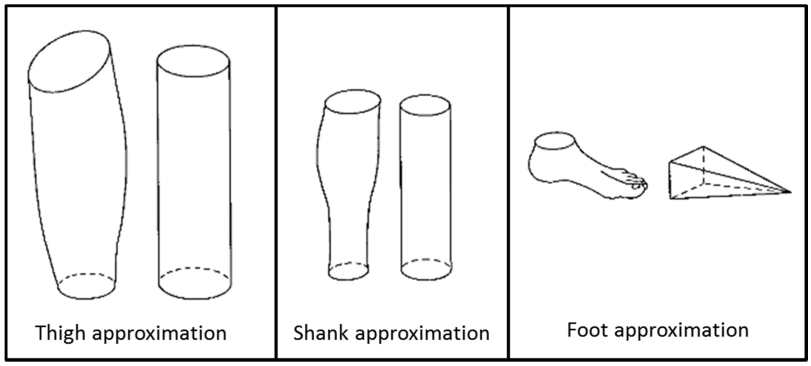

Figure 2.14 Geometric approximations of lower limb body segments.
The thigh and shank are assumed as cylinders and the foot as a right pyramid.
(Source: Adapted from VAUGHAN et al., 1999).

On the other hand, the lack of standards regarding how and where sensors should be placed on the body segments and the definition of its technical coordinate systems (CS) still limit the clinical application of this technology and further complicate the calculation of joint kinematics. Different approaches to accomplish this task can be found in the literature.

Kavanagh et al. (2006) proposes a wireless system based on accelerometers to estimate the segmental accelerations applied to gait analysis. Each accelerometer node consists of two biaxial accelerometers mounted perpendicular to each other, but only three of four axes are used. Authors mention the difficulties to obtain correct measurements due to, among other issues, the relation between the acceleration data to a global reference frame, since the reference frame of the acquired data is constantly moving. To counteract this effect, authors propose to apply a tilt correction to all acceleration data after their collection. During a static calibration trial and the subject standing in anatomical position, the degree of axes misalignment is determined (KAVANAGH; BARRETT; MORRISON, 2004). While the person is on quiet stance, the degree of tilt of the device in the sagittal (gravity vector) and frontal planes could be estimated using the accelerometer outputs. Subsequently, this tilt can be corrected using a correction factor determined from basic trigonometry.

Luinge, Veltink, and Baten (2007) propose the definition of coordinate systems for upper arm and forearm according to predefined movements. This procedure can also be applied to lower limbs. During a pronation-supination movement, the orientation of IMU frame (S) respect to the forearm frame (F) is determined (^{SF}R). The direction of the angular velocity, during pronation ($\boldsymbol{\omega}_{Pron}$), determines the forearm y-axis of the coordinate system as shown in Equation (2.1).

$$^{S}\boldsymbol{y}^{F} = \boldsymbol{\omega}_{Pron}/|\boldsymbol{\omega}_{Pron}|. \quad (2.1)$$

While the palm of the hand faced downwards (at the beginning and end of the trial) the direction of the forearm z-axis is assumed pointing in a vertical direction (opposite to the gravity vector $\boldsymbol{g}$). So, using the accelerometer, this axis can be calculated using the Equation (2.2).

$$^{S}\boldsymbol{z}^{F-} = -\boldsymbol{g}_{start}/|\boldsymbol{g}_{start}|. \quad (2.2)$$

Authors used the minus sing to indicate that this axis is later recomputed. The x-axis is determined making an orthogonal coordinate system. Since the y-axis and z-axis could not be exactly orthogonal using experimental data, the z-axis, as previously mentioned, is recomputed to determine a rotation matrix as shown in the Equation (2.3).

$$^{SF}R = [^{S}\boldsymbol{y}^{F} \times {}^{S}\boldsymbol{z}^{F-} \quad {}^{S}\boldsymbol{y}^{F} \quad (^{S}\boldsymbol{y}^{F} \times {}^{S}\boldsymbol{z}^{F-}) \times {}^{S}\boldsymbol{y}^{F}]. \quad (2.3)$$

The rotation matrix used for upper arm is determined in the same fashion through other predetermined movements. In this research two IMUs (Xsens, Enschede, 3° RMS orientation error) were used.

Following the same line of calibration procedure based on performing predefined movements, O'Donovan et al. (2007) proposes a 3D joint angle measurement technique based on IMU sensors. Authors verified that the technique reliably estimates the ankle joint angles and the results showed accurate measurements. Also, this technique could be expanded to other joints. The cited method proposes angle measurements independently of a fixed coordinate system, but the interest of this dissertation focuses on how the orientation of the segment respect to the sensor placed on is determined. The $^{SENi}R_{SEGi}$(i-segment CS orientation respect to i-sensor CS) matrix is calculated for each i-sensor using a two stage technique (Figure 2.15). The first stage consists of determining the axis of rotation while a subject in standing upright posture performs a rotation about the longitudinal axis of the full-body. Thus, $^{SENi}\hat{\boldsymbol{y}}_{SEGi}$ (the segment y-axis respect to the sensor CS) is defined. On the second stage, $^{SENi}\hat{\boldsymbol{z}}_{SEGi}$ (the segment z-axis respect to the sensor CS) is defined performing a knee extension (avoiding ankle joint motion). In this stage, the subject is seated and the medio-lateral axes of the foot and shank should be aligned in parallel.

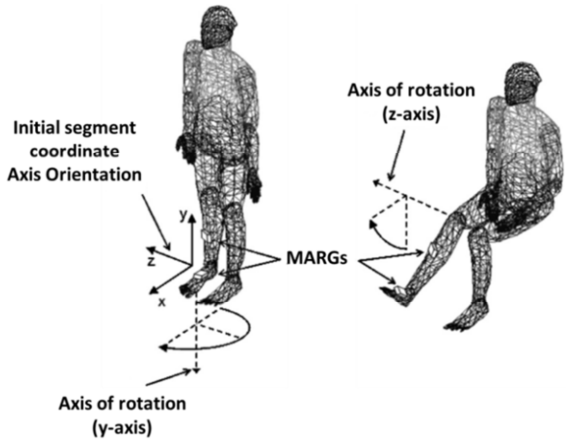

Figure 2.15 Two stage technique to define ${}^{SENi}\boldsymbol{R}_{\boldsymbol{SEGi}}$. First a whole body rotation around y-axis is performed. Secondly, a knee extension in sitting posture is realized around z-axis. (Source: Adapted from O'DONOVAN et al., 2007).

Finally, the x-axis is calculated as the cross product of the y-axis and z-axis. Therefore, the 3×3 orientation matrix ${}^{SENi}R_{SEGi}$ is given by Equation (2.4). Custom designed IMU sensors (which the authors called AARM) were used in this research.

$$ {}^{SENi}R_{SEGi} = [{}^{SENi}\hat{\boldsymbol{x}}_{SEGi}: \quad {}^{SENi}\hat{\boldsymbol{y}}_{SEGi}: \quad {}^{SENi}\hat{\boldsymbol{z}}_{SEGi}]. \tag{2.4} $$

An "anatomical" calibration technique using an external device was proposed by Picerno et al (2008). The procedure consists of identifying superficial anatomical landmarks (ALs) through an *ad hoc* experiment and determines their location relative to TF (technical frame). TF is associated with the sensor local frame and defined during the calibration procedure by the orientation matrix ${}^{g}R_{t}(0)$ relative to global frame. This task is accomplished using a calibration device which has two mobile pointers and one sensor aligned with the segment connecting them (Figure 2.16).

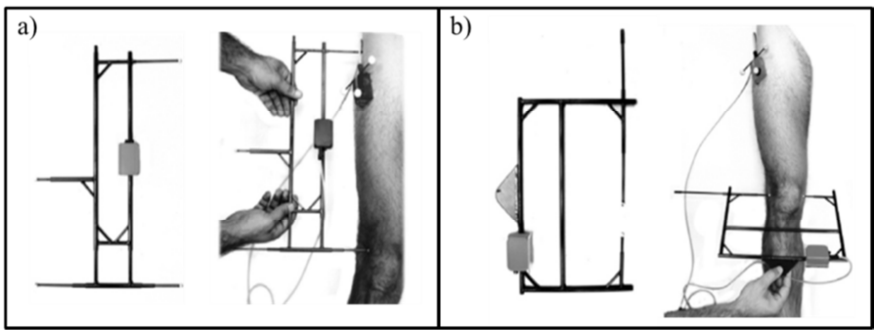

Figure 2.16 Calibration device used to measure the orientation of the line joining two ALs, a) Defining GT (greater trochanter) to LE (lateral femoral epicondyle) line and b) ME (Medial epicondyle) to LE line. (Source: Adapted from PICERNO et al., 2008).

Using this device, the orientation of a line joining two ALs (represented by unit vector ${}^{g}\boldsymbol{u}_k$) is measured relative to a global frame in order to define anatomical frames (AFs) as shown in Figure 2.17. For each segment, at least two non-parallel lines ($k = 1, 2$) have to be determined to define the anatomical orthogonal frame by using a geometric rule. Then, these unit vectors are represented in the sensor technical frame according to Equation (2.5).

$$ {}^{t}\boldsymbol{u}_k = {}^{g}R_t^T(0) \cdot {}^{g}\boldsymbol{u}_k. \tag{2.5} $$

and hence AFs respect to TFs (${}^{t}R_a(0)$) are calculated. In each i-th sampled instant of time, the AFs are calculated as shown in the Equation (2.6).

$$ {}^{g}R_a(i) = {}^{g}R_t(i)\,{}^{t}R_a(0); i = 1, \dots, N. \tag{2.6} $$

Finally, using the Cardan angular convention the joint angular kinematics of ankle, knee and hip can be determined. Four MTx (Xsens Technologies, NL) IMU sensors were used in this research.

Favre et al. (2009) propose a calibration procedure based on functional movements to estimate the 3D knee joint angles using two IMU sensors. Firstly, the constant quaternions ($\vec{\vec{R}}_A$ and $\vec{\vec{R}}_B$) that relate the coordinate systems of the segments and the sensors are calculated. The mentioned quaternions represent the bone-embedded anatomical frame (BAF) orientation of the thigh (A) and shank (B) segment, respectively, respect to the sensor local frames. IMU sensor orientations are expressed by two quaternions $\vec{\vec{Q}'}_A$ and $\vec{\vec{Q}'}_B$ respect to a common static reference frame XYZ (Figure 2.18).

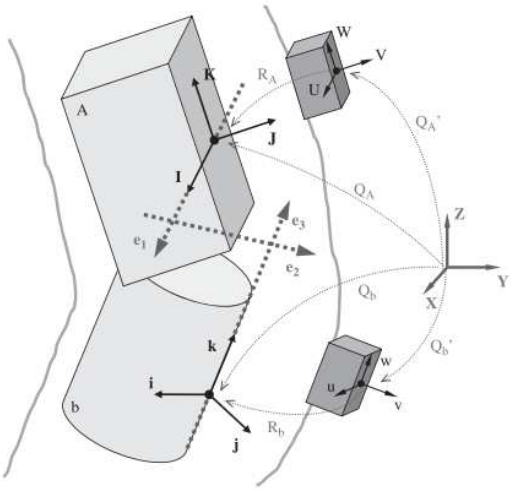

Figure 2.17 Relation of quaternions between BAFs (IJK and ijk), IMU frames (UVW and uvw) and fixed reference frame (XYZ). (Source: FAVRE et al., 2009).

Hence, the BAFs orientations are calculated respect to fixed reference frame in each instant of time according to Equation (2.7).

$$\begin{aligned} \vec{\vec{Q}}_A(t) &= \vec{\vec{Q}}'_A \otimes \vec{\vec{R}}_A \\ \vec{\vec{Q}}_B(t) &= \vec{\vec{Q}}'_B \otimes \vec{\vec{R}}_B \end{aligned}, \tag{2.7}$$

where $\otimes$ corresponds to the quaternion multiplication operation. The alignment of $\vec{\vec{Q}}'_A$ and $\vec{\vec{Q}}'_B$ to a common frame (XYZ) was determined using the functional procedure presented by Favre et al. (2008). The functional procedure consists of estimating the angle θ. This angle represents the offset in the horizontal plane between the T and S frames. These fixed reference frames are associated with the thigh (T) and shank (S) respectively. In the first study, θ was determined during a hip abduction/adduction movement (Figure 2.19b). During this "firm" hip movement (without any knee joint motion), it is assumed that the two segments (thigh and shank) angular velocities measured in a common reference frame must be equal.

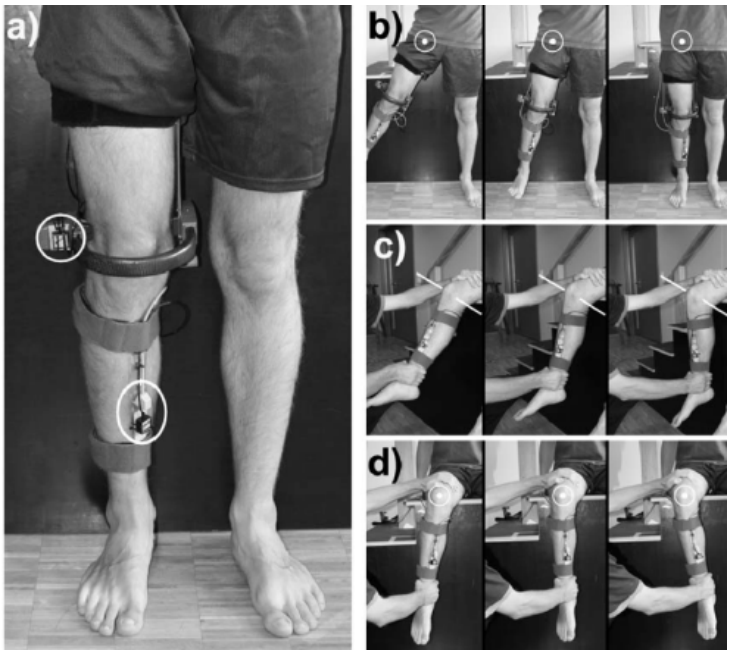

Figure 2.18 (a) Measurement system. (b-d) Predefined movements to determine body anatomical frames. (Source: FAVRE et al., 2009).

In consecutive research, authors expanded this technique adding other movement phases. Two passive movements are performed by an examiner while the subject is on sitting posture: a knee flexion-extension (performed between 45° and 80° of flexion, Figure 2.19c) and a

rotation of the shank in its frontal plane (Figure 2.18d). Thus, two axes of the quaternion $\vec{\vec{R}}_B$ are defined based on the angular velocity vectors that were measured during these movements. Lastly, the quaternion $\vec{\vec{R}}_A$ is estimated in order to align the thigh IMU frame to the shank-anatomical frame during a neutral standing posture ($\vec{\vec{Q}}_B(0)$), assuming the three knee joint angles equal to zero. Knee joint angles were estimated according to the International Society of Biomechanics (ISB) recommendations. The system used was made with up of two IMU (3D accelerometer and 3D gyroscope) connected to portable data-logger (Physilog®, BioAGM, CH). Also the IMUs were placed on the thigh and shank using an exoskeleton harness (Figure 2.19a).

Cutti et al. (2010) developed a protocol named “Outwalk” by defining many anatomical coordinate systems (according to the authors the most critical part of the process) as the number of joints adjacent to the segment following the standard Denavit-Hartenberg convention. The correct placement of the sensors units (SUs) (by identifying palpable landmarks or anatomical area defined) was required in this procedure, especially the sensors placed on the pelvis and shank due to their coordinate system (CS) are assumed to be coincident with the anatomical frames. The protocol also defines the manner to position the SUs according to their local frame (Figure 2.20). To define the orientation of anatomical/functional CS in the SU-CS associated, first the orientation of the mean flexion-extension (FE) axis of the knee has to be computed. This latter step is accomplished during a pure knee FE task. Here an examiner helps the subject to flex-extend the knee five times up to 70° keeping an upright posture. Therefore, V_{FLEX} (the FE axis) is calculated using the instantaneous helical axis (IHA) theory (CUTTI et al., 2008; STOKDIJK et al., 2000; WOLTRING, 1990). This vector is used to define the distal thigh CS. A complete table is provided showing the definition of all anatomical CS. Some of those aforementioned are aligned with the gravity vector. The joint angles calculation is performed using the relation between distal and proximal CS with the Euler sequence ZX’Y’’. In this research ten IMU sensors MTx (Xsens Technologies, NL) were used and the orientation data is provided by the proprietary software.

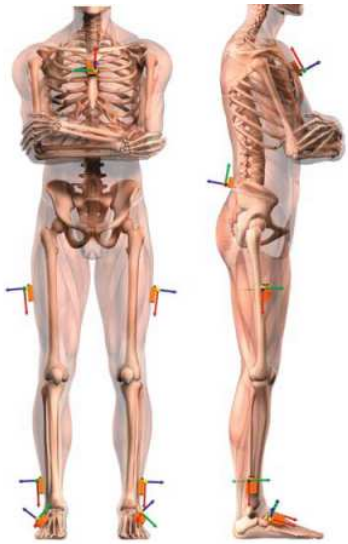

Figure 2.19 Positioning the sensors according their local frame. Red, green and blue arrows correspond to the X, Y and Z axes. (Source: CUTTI et al., 2010).

A two-phase functional calibration procedure was presented by Palermo et al. (2014). This procedure was used to obtain the body to sensor alignment independently to each sensor. The ${}^{s_i}R_{b_i}$ matrix represents the body-to-sensor rotation matrix. This matrix depends on how the body coordinate system (CS) is defined. Authors propose a functional procedure using two phases to determine this matrix. During phase A (Figure 2.21) the subject is in a standing upright posture and the z-axis (${}^{s_i}\boldsymbol{z}_{b_i}$) of the i-th body CS is defined parallel to the gravity vector measured by the i-th sensor ($\boldsymbol{z}_{g_i}$) as shown in Equation (2.8)

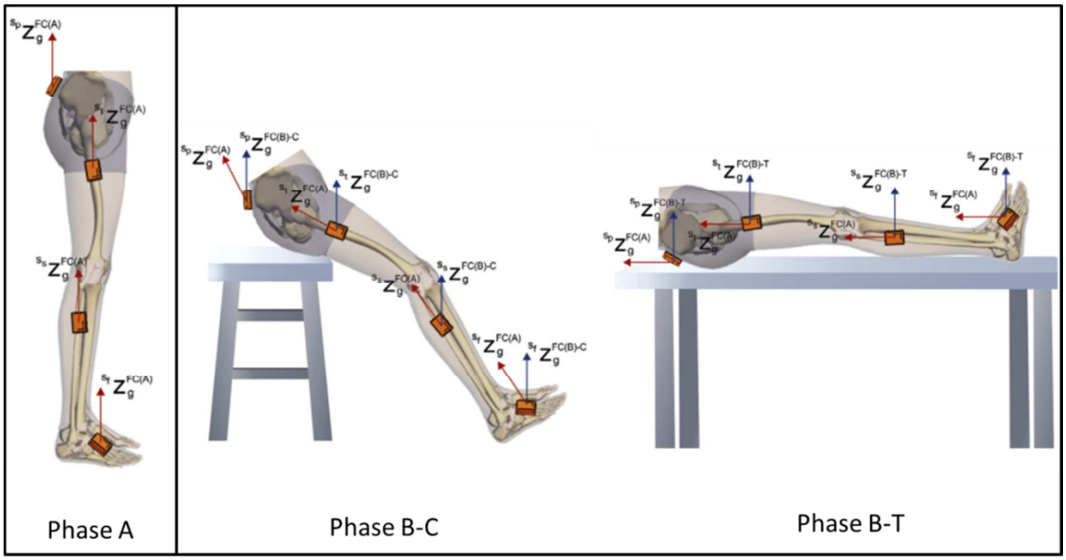

Figure 2.20 Two phases-calibration procedure. (Phase A) Standing upright posture, (B-C) sitting position with the trunk inclined and the legs stretched, (B-T) lying on a table. (Source: Adapted from PALERMO et al., 2014).

$$^{s_i}\boldsymbol{z}_{b_i} = {}^{s_i}\boldsymbol{z}_{g_i}^{\boldsymbol{A}}\,. \tag{2.8}$$

The phase B presents two variations. During (B-C) the subject is seated with the trunk inclined and the legs stretched or (B-T) the subject is lying on a table. In any of two variations, the sagittal plane (yz-plane) is defined parallel to $^{s_i}\boldsymbol{z}_{b_i}$ and $\boldsymbol{z}_{g_i}$ (the gravity vector measured by the sensor during the new posture B-C or B-T) with $\boldsymbol{y}_{b_i}$ pointing forward, thus, the x-axis $^{s_i}\boldsymbol{x}_{b_i}$ and the y-axis $^{s_i}\boldsymbol{y}_{b_i}$ are calculated using Equations (2.9) and (2.10), respectively. Hence the rotation matrix $^{s_i}R_{b_i}$ is calculated as shown in Equation (2.11). Note that the matrix $^{s_i}R_{b_i}$ is computed using only accelerometer data, but it is required that the subject maintain the sagittal plane of whole body parallel between phase A and phase B, preventing rotation in transverse and frontal plane.

$$^{s_i}\boldsymbol{x}_{b_i} = \frac{^{s_i}\boldsymbol{z}_{b_i} \times {}^{s_i}\boldsymbol{z}_{g_i}^{\boldsymbol{B}}}{\left|{}^{s_i}\boldsymbol{z}_{b_i} \times {}^{s_i}\boldsymbol{z}_{g_i}^{\boldsymbol{B}}\right|} \tag{2.9}$$

$$^{s_i}\boldsymbol{y}_{b_i} = {}^{s_i}\boldsymbol{z}_{b_i} \times {}^{s_i}\boldsymbol{x}_{b_i} \tag{2.10}$$

$$^{s_i}R_{b_i} = [{}^{s_i}\boldsymbol{x}_{b_i} \quad {}^{s_i}\boldsymbol{y}_{b_i} \quad {}^{s_i}\boldsymbol{z}_{b_i}]. \tag{2.11}$$

Tadano et al. (2013) used seven acceleration and gyro sensors placed on pelvis, both thighs, both shanks and both feet of five volunteers to estimate joint angles in the transverse and sagittal plane using quaternion calculations. Each volunteer was asked to do one gait trial walking 5 m. Authors compared measurements of motion obtained by the proposed method and a commercially camera-based motion analysis system. The calibration method developed converts the sensor to body segment CSs using a rotation matrix obtained by estimating the coordinates of sensors using camera images and markers during two static postures: standing upright and sitting with outstretched legs (where gravitational acceleration vector $\boldsymbol{g}_{stand}$ and $\boldsymbol{g}_{sit}$ are measured). Global frame axes are defined as: Z-axis in the opposite direction of $\boldsymbol{g}_{stand}$, Y –axis the cross product of $\boldsymbol{g}_{stand}$ and $\boldsymbol{g}_{sit}$, X-axis orthogonal to the other two vectors following right hand rule. Thus, a rotation matrix R_{SG} that converts the sensor frame orientation to global frame is obtained. Anthropometric measures also are required to calculate the body segment frames. Using camera images, another rotation matrix R_{GB} used to convert the global to the body segment frame is defined. Finally, the rotation matrix R_{SB} (sensor-to-body segment frame) is calculated as shown in Equation (2.12). The WAA-006 sensor units (Wireless Technologies, Inc., Japan) were used in this research.

$$R_{SB} = R_{SG}R_{GB}. \quad (2.12)$$

2.3.2. Conclusion

In conclusion, this section has presented some anatomical calibration procedures to determine the offset or the degree of misalignment between the sensor local frame and the underlying segment frame. The main problem with algorithms based on accelerometers and gyroscopes data (KAVANAGH et al., 2006; LUINGE et al., 2007; PICERNO et al. 2008; FAVRE et al., 2009; TADANO et al., 2013) is the difficulty in defining a common reference frame and, consequently, measuring 3D angles. To accurately measure 3D angles, a second reference axis is necessary, which is not present on systems based on accelerometers and gyroscopes. They have only the gravity vector as a common reference axis. The second reference axis is commonly the magnetic field vector, measured by the systems that include magnetometers.

Since heading drift remains a problem within systems that involve only accelerometers and gyroscopes, the anatomical calibration techniques presented that use such systems rely on predefined user´s movements to define the axis of joint motion, or use multiple devices such as cameras (TADANO et al., 2013) and anatomical landmark pointers (PICERNO et al., 2008). Moreover, these methods have to employ devices to fix the sensor in controlled positions such as exoskeleton harness (FAVRE et al., 2009). The need of these additional tools also increases the experiment duration and requires experienced personnel.

On the other hand, performing some movements keeping firm upright postures (CUTTI et al., 2010), minimal motion of other joints (O'DONOVAN et al., 2007; FAVRE et al., 2009) or maintaining the same orientation or joint angle between two postures (TADANO et al., 2013; PALERMO et al., 2014) may not be simple tasks to be performed by subjects with motor disabilities. Even for subjects without disability, performing these tasks require assistance of examiners. Hence, these mentioned methods may be more prone to calibration errors.

In this context, the objective of this M.Sc. dissertation is to provide a calibration procedure based on fast and easy sensor placement, with no need of movements performed by the user. Complementary, the procedure does not require any additional tools, which makes the technique practical for clinical use.

In the following chapter, the Tech IMU system will be present. Using this system the orientation of body segment, where sensors have been placed, can be collected. A check-procedure to assessment the static orientation consistency of the sensors will be also described. Finally, it will be proposed a protocol for sensor placement and a calibration procedure to define the technic-anatomical coordinate system. An initial test of the procedure will be presented in details using a two-spheres and goniometer configuration.

Chapter 3. Materials and Methods

This chapter presents the main features of the used materials, including the data acquisition system, IMU sensors and the software used for processing and analyzing orientation data. A brief discussion about the representation of rigid body's orientation in 3D space is also presented, which allows exposing the reasons why quaternion was the orientation format used in this dissertation. Also, a method to assess the static orientation consistency of IMUs is presented, which allows selecting the more reliable IMUs for further experiments. Finally, the sensor-to-body calibration procedure applied to gait analysis proposed in this dissertation is presented.

3.1. Motion Acquisition System

To fulfill the objective of providing an easy and flexible tool for gait analysis to be used in external environments, the Tech MCS (Technaid, Spain) motion acquisition system based on IMUs was used. This system is composed, mainly, of a HUB and 4 Tech IMU-CAN sensors.

The Tech-HUB V.3 (Figure 3.1) uses Bluetooth or USB communications to send the orientation data from sensors to the computer. IMU sensors are connected to the HUB through a CAN (Controller Area Network) bus. The HUB can drive up to 16 IMUs simultaneously and it is powered by four AA batteries or using a power adapter. Some technical features of the HUB are shown in Table 3.1 (TECHNAID, 2014).

Each Tech IMU-CAN (Figure 3.2) sensor is comprised of a tri-axial accelerometer, tri-axial gyroscope and a tri-axial magnetometer sensor. Also, IMUs include a temperature sensor to compensate errors due to temperature sensibility from gyroscopes and magnetometers. Technical features of inertial sensors are shown in Table 3.2.

Figure 3.1 Tech IMU-CAN connected to the Tech-HUB and a red adapter Bluetooth. (Source: Adapted from TECHNAID, 2014).

Table 3.1 Technical features Tech-HUB.

Features	Value
Nominal Voltage (V)	5.0
Maximum current (A)	3.0
Dimension W x L x H (cm)	10 x 15 x 6
Frequency rate (Hz)	10 – 200
Power supply	4 AA Adapter 110/220 VAC
Communication	USB 2.0 Bluetooth PC Offline mode Micro SD

Figure 3.2 Tech IMU-CAN sensors, illustrating local coordinate systems. To describe the convention of the output of Technaid's sensors. (Source: MELIM, 2013).

Table 3.2 Technical features of Tech IMU.

Features		Magnitude / Range	Units
Supply Voltage		3.7 – 4.5	VDC
Current		100 – 110	mA
Dimension W x L x H		26 x 36 x 11	mm
Peso		9	g
Gyroscopes	**Range**	± 500 / ± 2000 ± 8.727 / ± 34.9	°/s rad/s
	Sensibility	2,0 / 0,5	mV/°/S
Accelerometer	**Range**	± 3.6 ± 35,32	G m/s^2
	Sensibility	300	mV/g
Magnetometer	**Range**	± 2 ± 200	gauss µT
	Sensibility	0.5	V/gauss
Accuracy inertial sensor		< 1	degree
Wireless range with Line-Of-Sight		150	m
Wireless range with obstacles		50	m
Frequency rate		10 - 200	Hz
Physical measurement: • 3D Angular velocity (rad/s) • 3D Acceleration (m/s^2) • 3D Magnetic field (µT) • Temperature (°C)		**Output format:** • **Digital**: Digitalized signal values at 12 bits. • **Physical**: Physical signal values on the corresponding unit of measurement. • **Orientation**: Direction cosine matrix (DCM) or Quaternions	

Data processing by the manufacturer: Data from 3D accelerometers, gyroscopes and magnetometers are processed by a fusion data algorithm to obtain the orientation data. This algorithm consists of two stages (TECHNAID, 2014). First stage is calibration which provides the initial orientation using only the 3D accelerometer and 3D magnetometer data. This process is made only one time, at the beginning of each capture, before the user starts to move. Second stage consists of estimating the IMU orientation when movement occurs, where data from 3D gyroscopes are also used. Two mentioned stages are used in a sensorial fusion procedure that involves an Extended Kalman Filter (EKF), which is executed into the IMU.

In this dissertation the 3D orientation measurements of each sensor are provided by Technaid's sensor fusion algorithm. The manufacturer indicates that errors in angle estimation for static measurements are smaller than 1° (TECHNAID, 2014). This was validated using a

spot check for assessing static orientation proposed by Picerno et al. (2011) and presented in this dissertation in Section 3.3

To estimate lower limb joint angles, the orientation of the two adjacent segments is required. Thus, the joint's relative angle is defined as the orientation of a distal segment respect to a proximal segment (VAUGHAN et al., 1999). To measure the orientation of body segments, at least one inertial sensor is placed on each segment. In this dissertation, the interest is to analyze the angular displacement of three joints: hip, knee and ankle, making a complete description of lower-limb kinematics during gait.

For this task, four IMU sensors were used, which were placed on the pelvis, thigh, shank and foot. Bluetooth communication to the computer was chosen for practical reasons and the orientation data were acquired using the quaternion format at 50 Hz. It is important to state that in the case of human gait analysis, frequency components up to 5 Hz are found (YANG; KONG, 2009). A total of four quaternions were collected at each sample time, one for each IMU. These quaternions represent the sensor current orientation respect to the global reference system. The global frame is defined by the fusion algorithm using accelerometer and magnetometer data. Thus, data samples express the absolute orientation of each sensor.

Next section addresses the discussion about three ways to represent the orientation of a rigid body and it is explained why quaternion representation was selected.

3.2. Quaternions vs. DCM and Euler Angles

3.2.1. Quaternions

Rotations and orientations in a three dimensional space can be represented using quaternions. Quaternions are four-element vectors $q = (q_0, q_1, q_2, q_3) = (q_0, \mathbf{q})$, to which is assigned the non-commutative multiplication rule. They were first devised by William Rowam Hamilton (1805-1865), an Irish mathematician who described quaternions as four-element vectors with the first element as the scalar part and the remaining three as the vector part (HANSON, 2006) (see Equation (3.1)).

The algebra of quaternions is often denoted by H or $\mathbb{H}$. Unlike multiplication of real or complex numbers, multiplication of quaternions is not commutative. Quaternion

multiplication (also called Hamilton product) is defined as shown in Equation (3.2) (HANSON 2006):

$$q = q_0 + q_1\mathbf{i} + q_2\mathbf{j} + q_3\mathbf{k}. \tag{3.1}$$

$$\begin{aligned} p \otimes q &= (p_0, p_1, p_2, p_3) \otimes (q_0, q_1, q_2, q_3) \\ p \otimes q &= \begin{bmatrix} p_0q_0 - p_1q_1 - p_2q_2 - p_3q_3 \\ p_1q_0 + p_0q_1 + p_2q_3 - p_3q_2 \\ p_2q_0 + p_0q_2 + p_3q_1 - p_1q_3 \\ p_3q_0 + p_0q_3 + p_1q_2 - p_2q_1 \end{bmatrix} . \\ p \otimes q &= (p_0q_0 - \mathbf{p}\cdot\mathbf{q}, p_0\mathbf{q} + q_0\mathbf{p} + \mathbf{p}\times\mathbf{q}) \end{aligned} \tag{3.2}$$

For representing orientations and rotations, only quaternions of unit length are used. These obey the unit length restriction, as expressed in Equation (3.3).

$$q \cdot q = (q_0)^2 + (q_1)^2 + (q_2)^2 + (q_3)^2 = (q_0)^2 + \mathbf{q}\cdot\mathbf{q} = 1. \tag{3.3}$$

The inverse of a quaternion is defined as shown in Equation (3.4). Where, q^* is the conjugate of q and $\|q\|$ its norm. Note that given the condition of unit quaternion $q^{-1} = q^*$.

$$q^{-1} = \frac{q^*}{\|q\|^2}. \tag{3.4}$$

According to the Euler's rotation theorem (HANSON, 2006), any rotation can be described using a unit-vector $\hat{\mathbf{n}}$ (called also Euler axis) and an angle θ, which describes a rotation around the mentioned vector (Figure 3.3). Its corresponding quaternion is shown in Equation (3.5).

$$q(\theta, \hat{\mathbf{n}}) = \left(\cos\left(\frac{\theta}{2}\right), \hat{\mathbf{n}}\, sin\left(\frac{\theta}{2}\right)\right). \tag{3.5}$$

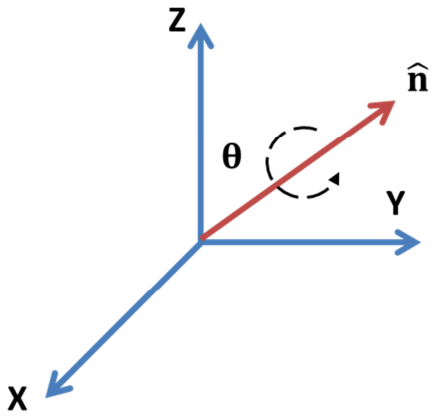

Figure 3.3 Euler's rotation theorem, a rotation represented by an Euler axis $\hat{\mathbf{n}}$ and angle $\boldsymbol{\theta}$.

3.2.2. Direction Cosine Matrix (DCM)

A rotation matrix is a matrix that when multiplied by a vector, rotates the vector but not change its length. The special orthogonal group of all 3×3 rotation matrices is denoted by $SO(3)$ (DIEBEL, 2006). Thus, for M as a proper matrix, if $M \in SO(3)$, then M has the properties as shown in Equation (3.6).

$$\det(M) = 1 \text{ and } M^{-1} = M^T. \tag{3.6}$$

The orientation of a rigid body can be described by using these rotation matrices. Consider $O - xyz$ as an orthogonal reference frame (or global frame), where x, y and z are the unit vectors of the frame axes. Also, consider an orthogonal frame, called local, attached to the body $O - x'y'z'$, where x', y' and z' are the unit vectors of the frame axes. In this case, both frames have the same origin (e.g. see Figure 3.4). The vectors of local frame are expressed respect to the global frame using Equation (3.7) and its rotation matrix associated is shown in Equation (3.8) (SCIAVICCO; SICILIANO 2000).

$$\begin{aligned} x' &= x'_x x + x'_y y + x'_z z \\ y' &= y'_x x + y'_y y + y'_z z. \\ z' &= z'_x x + z'_y y + z'_z z \end{aligned} \tag{3.7}$$

$$M = \begin{bmatrix} x'_x & y'_x & z'_x \\ x'_y & y'_y & z'_y \\ x'_z & y'_z & z'_z \end{bmatrix}. \tag{3.8}$$

Rotations around one axis are expressed using elementary rotation matrices. Suppose that the global frame $O - xyz$ is rotated by an angle α about axis x (see Figure 3.4), an angle β about axis y and an angle γ about axis z, separately. Let $O - x'y'z'$ be the rotated frame. The elementary rotation matrices associated to these rotations are shown in Equations (3.9) to (3.11).

$$M_x(\alpha) = \begin{bmatrix} 1 & 0 & 0 \\ 0 & \cos(\alpha) & -\sin(\alpha) \\ 0 & \sin(\alpha) & \cos(\alpha) \end{bmatrix}. \tag{3.9}$$

$$M_y(\beta) = \begin{bmatrix} \cos(\beta) & 0 & \sin(\beta) \\ 0 & 1 & 0 \\ -\sin(\beta) & 0 & \cos(\beta) \end{bmatrix}. \tag{3.10}$$

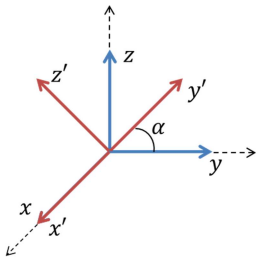

Figure 3.4 Rotation of $\boldsymbol{O-xyz}$ by an angle $\boldsymbol{\alpha}$ around axis x.

$$M_z(\gamma) = \begin{bmatrix} \cos(\gamma) & -\sin(\gamma) & 0 \\ \sin(\gamma) & \cos(\gamma) & 0 \\ 0 & 0 & 1 \end{bmatrix}. \tag{3.11}$$

Any rotation can be expressed using a sequence of elementary rotation matrices according to Euler sequences, for example ZXY sequence (see Equation (3.12), where c is the cosine and s is the sine). Rotation matrices also are referred as direction cosine matrix, because the matrix elements are the cosines of the unsigned angles between the local frame and the global frame as shown in Equation (3.13) (DIEBEL, 2006).

$$M_{ZXY}(\gamma,\alpha,\beta) = \begin{bmatrix} c(\beta)c(\gamma) - s(\alpha)s(\beta)s(\gamma) & -c(\alpha)s(\gamma) & s(\beta)c(\gamma) + s(\alpha)c(\beta)s(\gamma) \\ c(\beta)s(\gamma) + s(\alpha)s(\beta)c(\gamma) & c(\alpha)c(\gamma) & s(\beta)s(\gamma) - s(\alpha)c(\beta)c(\gamma) \\ -c(\alpha)s(\beta) & s(\alpha) & c(\alpha)c(\beta) \end{bmatrix}. \tag{3.12}$$

$$M = \begin{bmatrix} \cos(\theta_{x',x}) & \cos(\theta_{y',x}) & \cos(\theta_{z',x}) \\ \cos(\theta_{x',y}) & \cos(\theta_{y',x}) & \cos(\theta_{z',x}) \\ \cos(\theta_{x',z}) & \cos(\theta_{y',x}) & \cos(\theta_{z',x}) \end{bmatrix}. \tag{3.13}$$

There are two definition of rotation related to physical motions: intrinsic and extrinsic rotations. Intrinsic rotations are rotations around the local frame axes, that means that each subsequence rotation is around the actual frame axes (see Figure 3.5a). Extrinsic rotations are rotations around the fixed (global) frame axes (see Figure 3.5b).

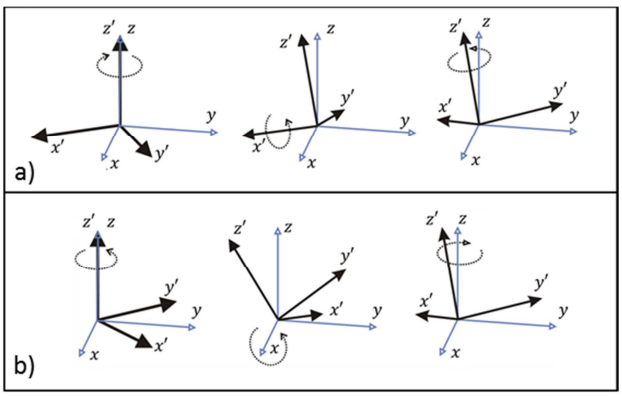

Figure 3.5 Sequence of rotations a) Intrinsic (z-x'-z'') and b) Extrinsic (z-x-z).

A matrix rotation $M = X(\alpha)Y(\beta)Z(\gamma)$ represents a composition of intrinsic rotations about axes x-y'-z″, if used to pre-multiply column vectors. This notation, x-y'-z″ indicates that first rotation is around x, second rotation is around actual y and the last rotation around actual z. A matrix rotation $M = Z(\gamma)Y(\beta)X(\alpha)$ represents a composition of extrinsic rotations about axes x-y-z. In this case, the rotations are around x-axis, y-axis and z-axis of global (fixed) frame.

3.2.3. Euler Angles

Maybe the most common way to represent rotations and orientations in three-dimensional space are Euler angles. As aforementioned, three coordinate rotations in sequence can describe any rotation. For notation, angles α, β and γ can be arranged in a three dimensional vector called the Euler angle vector u, defined as shown in Equation (3.14)

$$u := [\alpha, \beta, \gamma]^T. \tag{3.14}$$

There are twelve possible sequences that satisfy the constraint that no two consecutive numbers in a valid sequence may be equal (DIEBEL, 2006). For notational brevity, rotations around x-axis, y-axis and z-axis are numbered 1, 2 and 3, respectively. Thus, the set of possible sequences is shown in Equation (3.15).

$$(i,j,k) \in \begin{Bmatrix} (1,2,1), & (1,2,3), & (1,3,1), & (1,3,2), \\ (2,1,2), & (2,1,3), & (2,3,1), & (2,3,2), \\ (3,1,2), & (3,1,3), & (3,2,1), & (3,2,3), \end{Bmatrix}. \tag{3.15}$$

For the ZXY sequence (or 3, 1, 2 sequence), whose rotation matrix is expressed in Equation (3.12), the Euler angles are determined using the equations shown in Equation (3.16). Where asin function denotes the inverse of the sine and atan2 is the arctangent function with two arguments.

$$\begin{aligned} \alpha &= \operatorname{asin}\big(M_{ZXY}(3,2)\big) \\ \beta &= \operatorname{atan2}\big(-M_{ZXY}(3,1), M_{ZXY}(3,3)\big). \\ \gamma &= \operatorname{atan2}\big(-M_{ZXY}(1,2), M_{ZXY}(2,2)\big) \end{aligned} \tag{3.16}$$

Singularities- Different singularities are found in the various Euler angle representations (dependent of rotation sequence). These singularities are said to arise from the Gimbal lock (DIEBEL, 2006). This physical phenomenon of gimbal lock is referred as the loss of one degree of freedom in a three-dimensional mechanism, which results from having coplanar axes of rotation (HANSON, 2006). This “locks" the system into rotation in a degenerate two-dimensional space.

3.2.4. Rotation Conversions

Convert from Euler angles to rotation matrix and vice versa: As it was mentioned, using Euler angles and rotation matrix, there are twelve possible sequences to reach a desired orientation. To convert from DCM to Euler angles and vice versa a convention (which define the sequence) is required (DIEBEL, 2006). One example was shown previously, that is, using Equation (3.12) it is possible to convert from Euler angles (α, β and γ) to rotation matrix M_{ZXY} and using Equation (3.16), it is possible to convert from rotation matrix to Euler angles.

Convert from unit quaternions to Euler angles and vice versa: Converting to Euler angles require a convention that dependent of a rotation sequence. For example, the equations to convert from quaternions to Euler angles, using the ZXY sequence, are shown in Equation (3.17).

$$\begin{aligned} \alpha &= \operatorname{asin}\big(2(q_2 q_3 + q_0 q_1)\big) \\ \beta &= \operatorname{atan2}(2(q_0 q_2 - q_1 q_3), q_0^2 - q_1^2 - q_2^2 + q_3^2) \\ \gamma &= \operatorname{atan2}(2(q_0 q_3 - q_1 q_2), q_0^2 - q_1^2 + q_2^2 - q_3^2). \end{aligned} \tag{3.17}$$

The conversion from a particular Euler angle sequence to a quaternion can be written as the product of the three axis-angle unit quaternions defined using pure rotations. That is, for the sequence ZXY, with rotation angles $[\gamma, \alpha, \beta]$, the corresponding quaternion is shown in Equation (3.18) (DIEBEL, 2006):

$$q_{zxy}(\gamma, \alpha, \beta) = q(\gamma, k) \otimes q(\alpha, i) \otimes q(\beta, j).$$

$$q_{zxy}(\gamma,\alpha,\beta)=\begin{bmatrix} cos\left(\frac{\gamma}{2}\right)cos\left(\frac{\alpha}{2}\right)cos\left(\frac{\beta}{2}\right)-sin\left(\frac{\gamma}{2}\right)sin\left(\frac{\alpha}{2}\right)sin\left(\frac{\beta}{2}\right) \\ cos\left(\frac{\gamma}{2}\right)sin\left(\frac{\alpha}{2}\right)cos\left(\frac{\beta}{2}\right)-sin\left(\frac{\gamma}{2}\right)cos\left(\frac{\alpha}{2}\right)sin\left(\frac{\beta}{2}\right) \\ sin\left(\frac{\gamma}{2}\right)sin\left(\frac{\alpha}{2}\right)cos\left(\frac{\beta}{2}\right)+cos\left(\frac{\gamma}{2}\right)cos\left(\frac{\alpha}{2}\right)sin\left(\frac{\beta}{2}\right) \\ sin\left(\frac{\gamma}{2}\right)cos\left(\frac{\alpha}{2}\right)cos\left(\frac{\beta}{2}\right)+cos\left(\frac{\gamma}{2}\right)sin\left(\frac{\alpha}{2}\right)sin\left(\frac{\beta}{2}\right) \end{bmatrix}. \quad (3.18)$$

Convert from unit quaternions to DCM. To convert from unit quaternions to direction cosine matrix, as that shown in Equation (3.13), the relation shown in Equation (3.19) is applied.

$$M(q)=\begin{bmatrix} q_0^2+q_1^2-q_2^2-q_3^2 & 2(q_1q_2-q_0q_3) & 2(q_1q_3+q_0q_2) \\ 2(q_1q_2+q_0q_3) & q_0^2-q_1^2+q_2^2-q_3^2 & 2(q_2q_3-q_0q_1) \\ 2(q_1q_3-q_0q_2) & 2(q_2q_3+q_0q_1) & q_0^2-q_1^2-q_2^2+q_3^2 \end{bmatrix}. \quad (3.19)$$

To convert from rotation matrix to unit quaternion is slightly more complex and, according to Diebel (2006), there are four different inverse mappings, but they will not be mentioned in this dissertation.

3.2.5. Comparison of Unit Quaternions, DCM and Euler Angles

Perhaps the first and main disadvantage of Euler angles, as it was mentioned, is that the important functions have singularities (DIEBEL, 2006). Euler angles and rotation matrixes both are sequence dependent. A desired orientation can be reached in many different ways that depend on a convention, which makes these two representations subject to ambiguities.

Alternatively, the singularities associated with Gimbal lock do not appear in the quaternion representation (HANSON, 2006). In this dissertation quaternions were selected to represent orientation avoiding these singularities. Some advantages and disadvantages of the three different representations are shown in Table 3.3

From the point of view of computational cost, quaternions are represented by four numbers, unlike the DCMs that need nine numbers. That means, quaternions are more space efficient to store than DCMs. Another of the reasons of why quaternion representation was selected in this dissertation is because using DCM, the Technaid system can only drive up to four sensors. Using quaternions, the system can drive up to ten sensors, which allows the method presented in this dissertation to be expanded to other articulations, using more sensors.

Table 3.3 Advantages and disadvantages of quaternion, DCM and Euler angles.

Representation	Advantages	Disadvantages
Unit quaternions	-Avoid Gimbal lock -Space efficient to store -Coordinate system independency	-Do not have intuitive physical meanings
Euler angles	-Specify an orientation in an intuitive way	-Subject to singularities -Sequence dependent
DCM	-Intuitive physical meanings	-Possible ambiguities in the definition -Order of rotation dependent -Rotation represented by many different rotation matrices -Redundant information

3.3. Static Assessment of IMU Sensors

IMUs have a local frame (LF) defined respect to global fixed frame (GF). When LF and GF are aligned, the direction of IMU x-axis points to Earth's magnetic north and z-axis direction is opposite to gravity vector.

For the assessment evaluation of IMU performance, a spot check for assessing static orientation measurements of seven available Tech-IMUs was applied. The test was introduced by Picerno et al (2011). This consists of determining the orientation consistency in two scenarios: 1) Static orientation consistency of all IMUs with respect to a common global frame (Inter-IMU consistency, IC); and 2) consistency of each IMU static orientation with respect to an invariant global frame (Self-IMU consistency, SC). The first case exposes the reliability of the seven IMU in measuring the same global frame, and the second case, the reliability of that one IMU measures the same global frame regardless of its orientation in space.

This test was performed, essentially, to know the initial state of the system, so it is possible identify the four more reliable IMUs to exclude the other sensors and suggest to recalibrate them. Also, the gait analysis based on IMU is subject to errors affecting its accuracy. Usually, these errors are associated to ferromagnetic disturbances (ROETENBERG et al., 2005; SABATINI, 2006). In addition, it is said that the IMU performance decreases over a period of use due to the fact that calibration parameters become no longer effective (JURMAN et al.,

2007; BRODIE; WALMSLEY; PAGE, 2008). Thus, it is of the interest of this dissertation to identify issues related to the system accuracy.

The software Tech MCS was used to acquire orientation data in quaternion format. Seven IMUs were tested and these are identified (ID IMU) using the following serial numbers: 88, 89, 90, 91, 92, 101 and 104. All experiments were conducted in a space as far from metal objects as possible (approximately a 2×2×1 m^3 volume). Additionally, the devices were kept far from computers, cell phones and other devices that may cause ferro-magnetic disturbances. Experiments were performed on a wooden table 1 m off the ground, and a 20 minutes warm-up of sensors was completed before the experiments, in such a way that the orientation measurement was stabilized. The acquisition frequency was set to 50 Hz.

3.3.1. Test Description

Inter-IMU consistency (IC) test – IMUs were fixed into a wooden rigid box with flat bottom and sides (see Figure 3.6a). IMUs were fixed using double-side tape spaced, approximately, 3 cm and carefully aligned to each other. So, it is expected that all LF IMU orientations were the same. The box was positioned on the table and oriented in twelve different poses. Four poses for each one of the three axes of rotation: z-axis, y-axis and x-axis. From an initial position (z-axis up) the box was rotated anticlockwise with steps of approximately 90° from the initial pose to 270° for each axis of rotation. After an initial period of 60 s, the box was rotated and left stationary for 20 s. Only the last 10 s of acquired data for each pose were used. A total of twenty-four orientations were collected.

Self-IMU consistency (SC) test – This test was executed for each IMU separately. A cross of intersection of two perpendicular lines was drawn in the bottom of the box. This marker allowed fixing and aligning each sensor to the box (see Figure 3.6b). Twelve different poses were collected for each IMU ($\theta = 0°, 90°, 180°, 270°$ for each axis). The axes of rotations were: z-axis up, y-axis and x-axis. The procedure of data acquisition and stationary times were equal to the IC test.

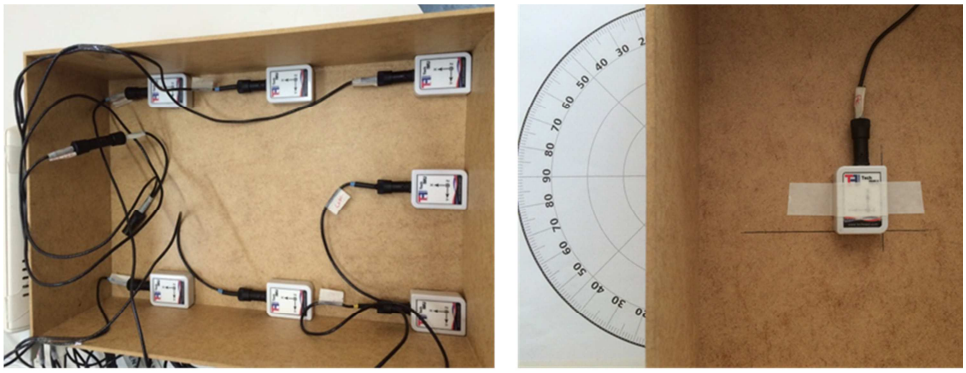

a) b)

Figure 3.6 IMUs fixed and aligned to the box.

Three angular components – The orientation quaternion q was expressed as shown in Equation (3.5). That orientation quaternion, with respect to the GF, was decomposed into three angular components: α, β and γ, using Equation (3.20) (PICERNO et al., 2011):

$$\alpha = \theta \frac{q_1}{sin\left(\frac{\theta}{2}\right)}$$

$$\beta = \theta \frac{q_2}{sin\left(\frac{\theta}{2}\right)} \quad . \tag{3.20}$$

$$\gamma = \theta \frac{q_3}{sin\left(\frac{\theta}{2}\right)}$$

Notation and data processing IC test– The quaternion ${}^{G_i}q_{L_j}$ represents the orientation of the LF of the i-th IMU in the j-th box pose with respect to its GF_i, where $i = 88, 89, 90, 91, 92, 101, 104$ and $j = 1, \ldots, 12$.The orientation quaternion ${}^{G_i}q_{L_j}$ is the average of quaternion data over a 10 s interval. The quaternion ${}^{G}\bar{q}_{L_j}$ represents the average quaternion calculated using the orientation data of all seven IMU for each j-th box pose. The difference between ${}^{G_i}q_{L_j}$ and ${}^{G}\bar{q}_{L_j}$ was determined as shown in Equation (3.21).

$$d_{i,j} = {}^{G}\bar{q}_{L_j} \otimes \left({}^{G_i}q_{L_j}\right)^{-1} \tag{3.21}$$

The angular components $\alpha(d_{i,j}), \beta(d_{i,j})$ and $\gamma(d_{i,j})$ were calculated according to the Equation (3.20) and expressed in absolute value for further error analysis. The objective of this step was to determine the deviation of each IMU from the average orientation for each

box pose. The orientation difference between two IMUs (all possible pairs) was computed as shown in Equation (3.22).

$$p_{i,k,j} = {}^{G_i}q_{L_j} \otimes \left({}^{G_k}q_{L_j}\right)^{-1}, \tag{3.22}$$

where $k = 88, 89, 90, 91, 92, 101, 104$. The angular components $\alpha(p_{i,k,j}), \beta(p_{i,k,j})$ and $\gamma(p_{i,k,j})$ were calculated according to Equation (3.20). The purpose of this step was to identify the largest angular difference along with the corresponding pair of IMUs.

Notation and data processing SC test - The quaternion ${}^{G_O}q_{L_O}$ represents the initial orientation measured by each IMU (L_O) with respect to the GF (G_O). The quaternion ${}^{G}q_{L}(\theta, \hat{e})$ represents the orientation quaternion measured by each IMU after a rotation θ ($\theta = 0°, 90°, 180°, 270°$) around one of its axes $\hat{e}$ ($\hat{e} = \hat{x}, \hat{y}, \hat{z}$). Both ${}^{G_O}q_{L_O}$ and ${}^{G}q_{L}(\theta, \hat{e})$ were calculated from averaging data over 10 s interval of time.

The quaternion ${}^{L_O}q_{L}(\theta, \hat{e})$ represents the rotation θ that describes each IMU around one of its axes $\hat{e}$ from the initial orientation L_O to the final L. This quaternion is mathematically defined using Equation (3.5) for the defined rotations ($\theta = 0°, 90°, 180°, 270°;\ \hat{e} = \hat{x}, \hat{y}, \hat{z}$).

The orientation difference between the measured GFs from the initial orientation (G_O) to the final orientation (G) can be expressed as shown in Equation (3.23).

$${}^{G_O}q_{G}(\theta, \hat{e}) = {}^{G_O}q_{L_O} \otimes {}^{L_O}q_{L}(\theta, \hat{e}) \otimes \left({}^{G}q_{L}(\theta, \hat{e})\right)^{-1}. \tag{3.23}$$

The corresponding angular errors, as shown in Equation (3.24), were determined according to Equation (3.20) and then expressed in absolute value for further error analysis. As it was mentioned, the objective of this step is to determine the degree of deviation of each IMU in measuring the same global frame regardless of its orientation in space. The results of this static assessment of IMU sensors are presented in Sections 4.1 and 5.1.

$$\begin{aligned} e_{G\alpha} &= \alpha\left({}^{G_O}q_{G}(\theta, \hat{e})\right) \\ e_{G\beta} &= \beta\left({}^{G_O}q_{G}(\theta, \hat{e})\right) \\ e_{G\gamma} &= \gamma\left({}^{G_O}q_{G}(\theta, \hat{e})\right). \end{aligned} \tag{3.24}$$

3.4. Sensor-to-Body Calibration Procedure

For estimating the lower limb joint angles, it is necessary to measure the orientation of the two adjacent body segments, which means, for example, to estimate the hip angles, the pelvis and thigh absolute orientations are required. In this dissertation, hip, knee and ankle joint angles of the right lower limb were estimated. That is, the pelvis (body segment named PV), the right thigh (TH), the right shank (SH) and the right foot (FT) orientations are required.

One IMU sensor was placed on each aforementioned body segment. Each body segment also has associated one coordinate system (BF), which is called in this dissertation "technic-anatomical frame". This is not an anatomical bone-embedded frame as the one defined by International Society of Biomechanics (ISB) recommendations (WU et al. 2002; GROOD; SUNTAY, 1983). The reason is that the axes of body segments' Cartesian coordinate systems, within ISB recommendations, are defined based on bony landmarks that are palpable or identifiable from X-rays.

Definition of technic-anatomical frame – During a standing upright posture, the technic-anatomical frames (BFs) are aligned with the gravity vector and the walking direction. The walking direction is defined using the opposite of z-axis of the pelvis frame (BF-PV). This z-axis is determined after a correction process that aligns the IMU placed on the pelvis with the gravity. This process is explained in details in Section 3.4.1. The technic-anatomical frames are presented in Figure 3.7 for each body segment. During the initial posture the joint angles are assumed to be zero, since the corresponding body segments are aligned.

Placing the IMUs in arbitrary position on the body segments, without identifying palpable landmarks, requires a sensor-to-body calibration procedure, which allows that the sensor coordinate system (or IMU frame, IMU-F) is aligned with the underlying body segment. The procedure consists of determining how the IMU sensor is oriented with respect to the body segment. In Section 3.4.2, the proposed sensor-to-body calibration algorithm is explained in details.

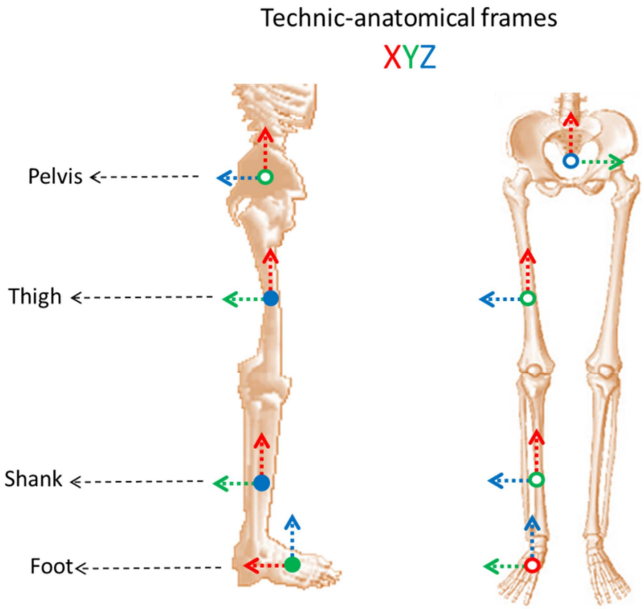

Figure 3.7 Technic-anatomical frame (BF) of the pelvis, thigh, shank and foot. Representation of the axes X, Y and Z in color red, green and blue, respectively.

3.4.1. Protocol of Sensor Placement

Four sensors were positioned from the pelvis through right lower limb (thigh, shank and foot segments) (see Figure 3.8). The pelvis sensor was placed on the sacrum at the S2 spinous process in the middle point between two posterior superior iliac spines. The IMU describes a coordinate system (IMU-F) defined as x-axis pointing cranially and z-axis pointing posteriorly. The thigh sensor was placed over the iliotibial tract approximately 5 cm above the patella. The shank sensor was positioned on the lower one-third of lateral shank 5 cm above of the lateral malleolus of the fibula.

The sensors on thigh and shank were positioned with z-axis pointing cranially and z-axis pointing laterally. The foot sensor was fixed with double sided tape on the dorsal region of the foot over the 3rd and 4th metatarsal bones, 3 cm above to the corresponding metatarsophalangeal joints, with z-axis pointing cranially and z-axis pointing posteriorly.

These sensors were attached with double-sided tape on an acrylic plate, which was glued to elastic band with Velcro. Such positions have been suggested by different authors (CUTTI et al., 2010; FERRARI et al., 2010; TAO et al., 2012).

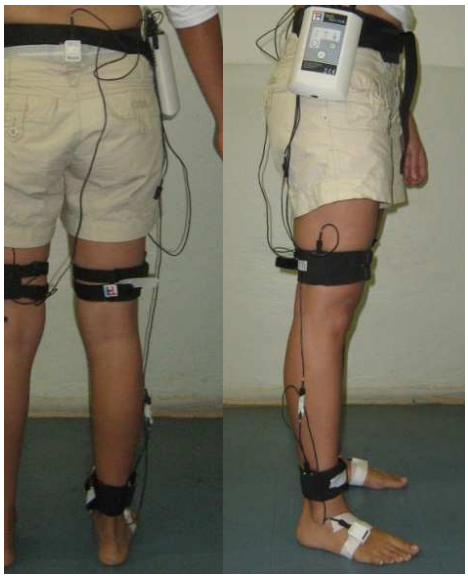

Figure 3.8 Sensor placement.

3.4.2. Calibration Algorithm and Definition of Technic-Anatomical Frames

During 5 s of static acquisition (initial upright posture), the orientation data were used to define sensor-to-body alignment. The first stage consists of correcting the sensor frame placed on the pelvis (IMU-F-PV). This correction procedure aims to align the IMU-F-PV with the gravity.

Let ${}^{GF}q_{IMU-F-PV_O}$ be the quaternion of IMU placed on the pelvis, in the initial posture computed for averaging the orientation data acquired over the 5 s interval. Since the orientation data were obtained in quaternion format, the operations to correct or align the sensor ${}^{GF}q_{IMU-F-PV_O}$ with the gravity were performed as follows:

1) Obtain x-axis ($X_{IMU\text{-}F\text{-}PV}$) of coordinate system referred to the IMU orientation measured by the quaternion associated ${}^{GF}q_{IMU-F-PV_O}$ in the initial posture. Using the Equation (3.19), $X_{IMU\text{-}F\text{-}PV}$ is defined as shown in Equation (3.24)

$$X_{IMU-F-PV} = [q_0^2 + q_1^2 - q_2^2 - q_3^2 \quad 2\cdot(q_1q_2 + q_0q_3) \quad 2\cdot(q_1q_3 + q_0q_2)]^T, \quad (3.24)$$

where q_0, q_1, q_2 and q_3 are the components of the quaternion ${}^{GF}q_{IMU-F-PV_O}$.

2) Define the angle θ between $X_{IMU-F-PV}$ and the gravity Z_G. The angle θ is calculated using Equation (3.25).

$$\theta = acos\big(2 \cdot (q_1 q_3 + q_0 q_2)\big). \tag{3.25}$$

3) Define the vector $\boldsymbol{n_1}$ orthonormal to the mentioned vectors ($X_{IMU-F-PV}$ and Z_G). Around this vector a rotation θ is made according to Euler's rotation theorem.

The orthonormal and unit vector $\mathbf{n_1}$ was defined as shown in Equation (3.26). The correction quaternion $q_C(\theta, \boldsymbol{n_1})$ was calculated using Equation (3.5)

$$\begin{gathered} \boldsymbol{n_1} = [2 \cdot (q_1 q_2 + q_0 q_3) \quad q_0^2 + q_1^2 - q_2^2 - q_3^2 \quad 0]^T \\ \boldsymbol{n_1} = \frac{n_1}{\|n_1\|} \end{gathered}, \tag{3.26}$$

where q_0, q_1, q_2 and q_3 are the components of the quaternion ${}^{GF}q_{IMU-F-PV_O}$. The technic-anatomical frame of the pelvis (BF-PV) calculated with respect to the global frame (GF), during the initial posture, was defined as shown in Equation (3.27)

$${}^{GF}q_{BF-PV_O} = q_C \otimes {}^{GF}q_{IMU-F-PV_O}. \tag{3.27}$$

Other initial technic-anatomical frame (BF) using quaternions were defined during the calibration procedure as shown in Table 3.4.

Table 3.4 Definition of technic-anatomical quaternions obtained during calibration posture (straight upright posture)

Segment	Initial quaternion definition
Pelvis (PV)	${}^{GF}q_{BF-PV_O}$
Thigh (TH)	${}^{GF}q_{BF-TH_O} = {}^{GF}q_{BF-PV_O} \otimes q_{ROT}(90°, \boldsymbol{x})$
Shank (SH)	${}^{GF}Q_{BF-SH_O} = {}^{GF}q_{BF-TH_O}$
Foot (FT)	${}^{GF}q_{BF-FT_O} = {}^{GF}Q_{BF-SH_O} \otimes q_{ROT}(180°, \boldsymbol{n_2})$

where $\boldsymbol{x} = [1\ 0\ 0]^{\boldsymbol{T}}$ and $\boldsymbol{n_2} = [1\ 0\ 1]^{\boldsymbol{T}}$

Let $q_{ROT}(\theta, \boldsymbol{n})$ be the quaternion calculated using Equation (3.5) for $\theta = 90°$ or $180°$ and $\boldsymbol{n} = \boldsymbol{x}$ or $\boldsymbol{n_2}$.

Once the initial technic-anatomical quaternions were defined, the sensor-to-body orientation ${}^{BF}q_{IMU-F-B}$ was determined for each sensor using Equation (3.28).

$$^{BF-B}q_{IMU-F-B} = {}^{GF}q^{*}_{BF-B_O} \otimes {}^{GF}q_{IMU-F-B}, \quad (3.28)$$

where B denotes the body segment, namely PV, TH, SH and FT. And $*$ the complex conjugate of the quaternion. Having the relative orientation of the sensor to body segment, the orientation of each segment at any instant in time can be determined as $^{GF}q_{BF-PV}$, $^{GF}q_{BF-TH}$, $^{GF}q_{BF-SH}$ and $^{GF}q_{BF-FT}$, for the pelvis, thigh, shank and foot, respectively. Then, the hip, knee and ankle joint rotations are defined by the orientation of the distal body segment with respect to the proximal body segment. The angles extraction is presented in detail in the next section.

3.4.3. Joint Angles Calculation

For calculating the joint angles using the quaternions presented for each body segment, the mathematical formalism presented by Grood and Suntay (1983) was used. The last general reporting standard for joint kinematics based on Joint Coordinate System (JCS) was proposed by the International Society of Biomechanics (ISB) (WU et al., 2002). The concept of JCS was first presented by Grood and Suntay (1983) only for the knee joint, but this has been adopted to define the kinematics of other human joints. The presented mathematical formalism uses the Cartesian coordinate systems and vector algebra. In this dissertation, the equivalent algebra using quaternions is presented.

According to Grood and Suntay (1983), in constructing the coordinate system for the joint (JCS), it is necessary to specify: 1) the Cartesian coordinate system fixed in each bone and 2) the body fixed axes of the joint coordinate system and the reference axes of the JCS used to describe the relative motion between two bones.

Let e_1 and e_3 be the unit vectors, which are the fixed axes to the proximal body segment (PB) and the distal body segment (DB), respectively. The third axis, e_2, is the common perpendicular to the body fixed axes. Therefore, it is defined as shown in the Equation (3.29).

$$e_2 = \frac{e_3 \times e_1}{|e_3 \times e_1|} \quad . \quad (3.29)$$

This common perpendicular axis is referred as floating axis, because it is not fixed in any body segment and moves in relation to both. In Table 3.5 the body fixed axes and the reference axes of the JCS are presented according to the frames shown in the Figure 3.7.

The Table 3.6 summarizes the sign convention used in defining the clinical rotations. In this dissertation, the sign of external rotation is negative, unlike presented by Grood and Suntay (1983), which is positive. That is used considering that recent scientific contributions by other authors studied in this dissertation (BENEDETTI et al. 1998; PICERNO et al., 2008; CUTTI et al., 2010; PALERMO et al., 2014) presented the external rotation as a negative angle.

Now, let ${}^{GF}q_{BF-PV}$, ${}^{GF}q_{BF-TH}$, ${}^{GF}q_{BF-SH}$ and ${}^{GF}q_{BF-FT}$ be the orientation quaternions that represent the frames fixed in each bone. Each body fixed, floating and reference axes, in Table 3.5, are computed as function of quaternions. For example, let e_{2-H}, e_{2-K} and e_{2-A} be the floating axis of the hip, knee and ankle joint, respectively.

Table 3.5 Body fixed, floating and references axes of each joint.

Joint	Joint Coordinate System	Body fixed and floating axes	References axes
HIP*	Pelvis axis (flexion-extension)	$e_1 = -Y_{PV}$	$e_1^r = -Z_{PV}$
	Femoral axis (internal-external rotation)	$e_3 = X_{TH}$	$e_3^r = -Y_{TH}$
	Floating axis (abduction-adduction)	$e_2 = \frac{X_{TH} \times (-Y_{PV})}{\lvert X_{TH} \times (-Y_{PV}) \rvert}$	
KNEE**	Femoral axis (flexion-extension)	$e_1 = Z_{TH}$	$e_1^r = -Y_{TH}$
	Tibial axis (internal-external rotation)	$e_3 = X_{SH}$	$e_3^r = -Y_{SH}$
	Floating axis (abduction-adduction)	$e_2 = \frac{X_{SH} \times Z_{TH}}{\lvert X_{SH} \times Z_{TH} \rvert}$	
ANKLE*	Tibial axis (dorsiflexion-plantar-flexion)	$e_1 = Z_{SH}$	$e_1^r = -Y_{SH}$
	Calcaneal (internal-external rotation)	$e_3 = Z_{FT}$	$e_3^r = -X_{FT}$
	Floating axis (inversion-eversion)	$e_2 = \frac{Z_{FT} \times Z_{SH}}{\lvert Z_{FT} \times Z_{SH} \rvert}$	

*JCS proposed by Wu et al., (2002) and **JCS proposed by Grood and Suntay (1983).

Table 3.6 Rotations of the hip, knee and ankle joint of right limb.

Joint	Flexion-extension	Abduction-adduction	Internal-external rot.
HIP	$\alpha = asin(e_2 \cdot X_{PV})$	$\beta = \text{acos}(-Y_{PV} \cdot X_{TH}) - \frac{\pi}{2}$	$\gamma = asin(e_2 \cdot Z_{TH})$
KNEE	$\alpha = -asin(e_2 \cdot X_{TH})$	$\beta = \text{acos}(Z_{TH} \cdot X_{SH}) - \frac{\pi}{2}$	$\gamma = asin(e_2 \cdot Z_{SH})$
ANKLE*	$\alpha = asin(e_2 \cdot X_{SH})$	$\beta = \text{acos}(Z_{SH} \cdot Z_{FT}) - \frac{\pi}{2}$	

*Ankle rotations are dorsiflexion-plantar flexion and inversion-eversion

The corresponding equations are shown in Equation (3.30). Where $M_i\left({}^{GF}q_{BF-j}\right)$ is the i-th column of M calculated using Equation (3.19) ($i = 1,2$ and 3), for j-th quaternion ($j = PV, TH, SH$ and FT). $|\cdot|$ denote that the vector must be normalized. Then, the equivalent equations in quaternions for calculating the joint rotations are presented in the Table 3.7.

$$e_{2-H} = \frac{M_1({}^{GF}q_{BF-TH}) \times \left(-M_2({}^{GF}q_{BF-PV})\right)}{|\cdot|}$$

$$e_{2-K} = \frac{M_1({}^{GF}q_{BF-SH}) \times M_3({}^{GF}q_{BF-TH})}{|\cdot|} \quad . \tag{3.30}$$

$$e_{2-A} = \frac{M_3({}^{GF}q_{BF-FT}) \times M_2({}^{GF}q_{BF-SH})}{|\cdot|}$$

Table 3.7 Joint rotations as functions of quaternions

Joint	Angles
HIP	$\alpha(e_{2-H}, X_{PV}), X_{PV} = M_1\left({}^{GF}q_{BF-PV}\right)$
	$\beta(Y_{PV}, X_{TH}), Y_{PV} = M_2\left({}^{GF}q_{BF-PV}\right), X_{TH} = M_1\left({}^{GF}q_{BF-TH}\right)$
	$\gamma(e_{2-H}, Y_{TH}), Y_{TH} = M_2\left({}^{GF}q_{BF-TH}\right)$
KNEE	$\alpha(e_{2-K}, X_{TH}), X_{TH} = M_1\left({}^{GF}q_{BF-TH}\right)$
	$\beta(Z_{TH}, X_{SH}), Z_{TH} = M_3\left({}^{GF}q_{BF-TH}\right), X_{SH} = M_1\left({}^{GF}q_{BF-SH}\right)$
	$\gamma(e_{2-K}, Z_{SH}), Z_{SH} = M_3\left({}^{GF}q_{BF-SH}\right)$
ANKLE	$\alpha(e_2, Z_{SH}), Z_{SH} = M_3\left({}^{GF}q_{BF-SH}\right)$
	$\beta(Y_{SH}, Z_{FT}), Y_{SH} = M_2\left({}^{GF}q_{BF-SH}\right), Z_{FT} = M_3\left({}^{GF}q_{BF-FT}\right)$

The results of this sensor-to-body calibration procedure applied to gait analysis of five volunteers without gait disabilities are presented in Section 5.2. In Section 4.1.2 and 4.2.2 the calibration procedure is applied to two semi-spheres and goniometer configuration, which allowed explore the calibration procedure using a rigid body with uniform geometry and controlled orientations.

3.4.4. Kinematics Parameters

The variables evaluated in this dissertation were the discrete angular kinematic parameters previously reported in a reference work by Benedetti et al. (1998) for the three planes of motion (see Table 2.2). Discrete parameters allow making a parametric analysis, which is demonstrated to be reliable and a practical method analyzing gait data. Also, it is a useful tool of the assessment of data reliability (BENEDETTI et al., 1998).

In the sagittal plane, H1, K1 and A1 refer to flexion at heel strike for hip, knee and ankle, respectively. H2, K2 and A2: peak flexion (plantar flexion for ankle) at loading response. H3, K3 and A3: peak extension (dorsiflexion for ankle) in stance phase. H4, K4, and A4: flexion H5, K5 and A5: peak flexion (dorsiflexion for ankle) in swing phase.

Frontal plane variables were H8, K8 and A8, which denote peak adduction (eversion for ankle) in stance phase. H9, K9 and A9 refer to the peak abduction (ankle inversion) in swing. Transverse plane was assessed by the pairs H11, K11 (peak internal rotation in stance) and H12, K12 (peak external rotation in swing phase).

These kinematic parameters are computed for each gait cycle. To determine them, there is a need to identify the two main phases of gait, stance and swing. This procedure of segmentation consists of determining the two events that indicate the start of each phase, which are heel strike (HS) and toe off (TO). Sabatini et al. (2005) proposes to determine HS and TO using the angular velocity sensed by a gyroscope on the foot. In Figure 3.9 the wave form processed signal is shown, where the estimation of HS is indicated as a circle and TO as a square.

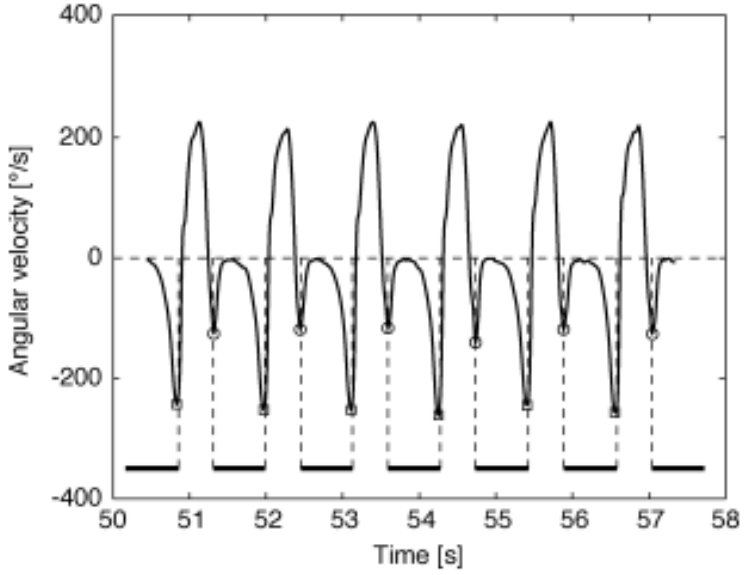

Figure 3.9 Detection of heel strike and toe off using angular velocity measured by a gyroscope placed on the foot. (Source: SABATINI et al., 2005).

In this dissertation, the orientation data of the foot are collected using quaternions. Each trial was divided in gait cycles to extract the kinematics parameters posteriorly. To determine the HS and TO, the angular velocity as a function on quaternion is computed as shown in Equation (3.31)

$$\Omega_t = 2\,{}^{GS}q^{*}_{BF-FT}\;\;{}^{GS}\dot{q}_{BF-FT}\;, \tag{3.31}$$

where ${}^{GS}\dot{q}_{BF-FT}$ is the vector of quaternion rates (or the time derivate of the unit quaternion) of the foot and $\Omega_t = \left(0, \omega_x, \omega_y, \omega_z\right)^T$ is the quaternion representation of the angular velocity ω_t. Using the component of the angular velocity on the sagittal plane (ω_y, for IMU placed on the foot), the HS and TO events are determined using a minimum detection algorithm.

Having HS and TO, it is possible to estimate the kinematics parameters at heel strike and toe off. In addition, with these two events of interest, the gait cycle is divided in the two main phases. Thus, it is possible to estimate the other kinematic parameters using maximum and minimum detection algorithm. The results of this estimation of kinematics parameters applied to gait analysis of five volunteers without gait disabilities are presented in Section 5.2.

Chapter 4. Simulations and Experimental Validation

In this chapter, general simulations are presented in Section 4.1.1. The aim is to study the behavior of IMU sensors during the static assessment and to validate the sensor-to-body calibration methods. For the static evaluation, the orientations of seven IMU were simulated. In Case Study 1, misalignments between sensors (less than 1°) were introduced in the simulation, which allows analyzing how this condition affects the measurements.

According to the manufacturer, the errors in estimating angles for static measurements should be smaller than 1°. So, corresponding errors were introduced randomly for the simulated angles (Case Study 2).

In Section 4.1.2, a two semi-spheres and goniometer set-up was built to explore the sensor-to-body calibration algorithm. Each semi-sphere is used to represent body segments with a known geometry, and the goniometer is used to represent an articulation with one degree of freedom. Using the goniometer, angular movements can be performed in a controlled way. Both scenarios allow validating the methods presented in Sections 3.3 and 3.4.

Finally, the experimental results that allow assessing the performance of the IMUs are presented. In Section 4.2.1, seven IMUs were assessed in a static setup. The aim is to know the initial state of the capture system, and identify the IMUs that present better performance to be used in further experiments. In Section 4.2.2, an experiment to explore the sensor-to-body segment calibration method was performed.

4.1. Simulations

4.1.1. Static Assessment of Simulated IMU Sensors

The evaluation method of static orientation consistency of IMUs, presented in Section 3.3, was simulated using possible orientations of seven IMU sensors.

Case Study 1: Errors due to misalignment between sensors.

Considering the experiment proposed in Section 3.3, the IMU sensors are fixed to a wooden box aligned to each other. Nevertheless, an observational error cannot be discarded, which is understood as an observational error as the parallax error. Thus, errors by misplacing the IMUs may affect the accuracy of the measurements. In this simulation, errors due to this condition are introduced to analyze its influence in the final results.

Assume a misalignment around the z-axis of 0.8°, -0.9°, 1°, -1°, 0.6°, -0.9° and 0.4° for the IMUs 1, 2, 3, 4, 5, 6 and 7, respectively. These misalignments are seven numbers generated using the function rand from MATLAB. Note that the worst cases (-1° and 1° of deviations) are included. Consider, additionally, that all devices are initially placed with z-axis up. Rotations of 0°, 90°, 180° and 270° around x-axis, y-axis and z-axis were performed (see Figure 4.1 Each posture of the wooden box was numbered as shown in Table 4.1.

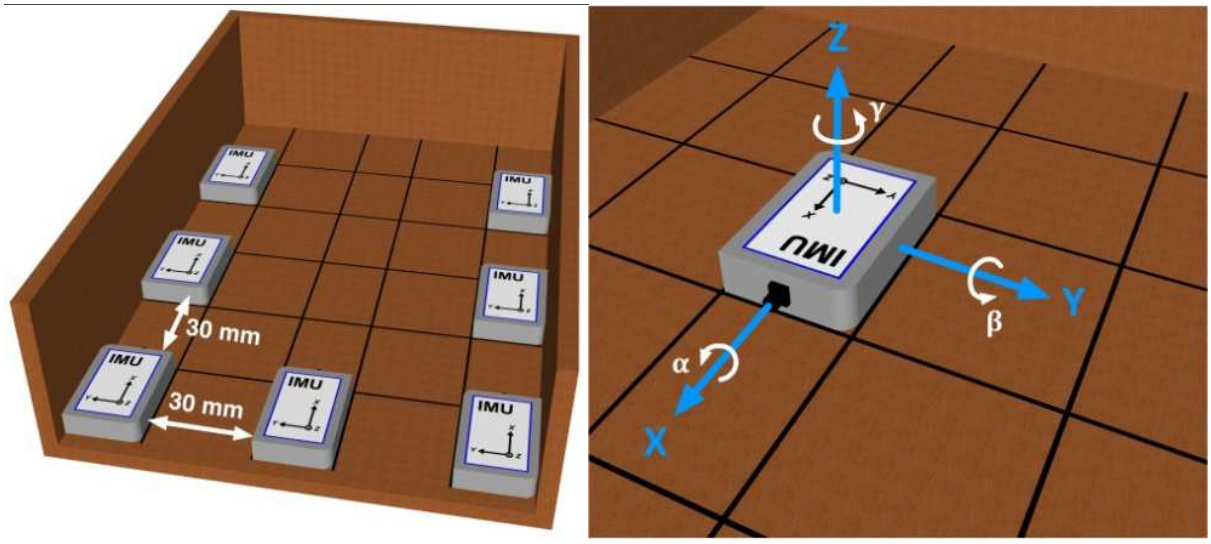

Figure 4.1 IMU sensors fixed to wooden box.

Table 4.1 Description of twelve postures of the wooden box.

Number posture	Description	Number posture	Description	Number posture	Description
1	0° around x-axis	**5**	0° around y-axis	**9**	0° around z-axis
2	90° around x-axis	**6**	90° around y-axis	**10**	90° around z-axis
3	180° around x-axis	**7**	180° around y-axis	**11**	180° around z-axis
4	270° around x-axis	**8**	270° around y-axis	**12**	270° around z-axis

Observe that the postures 1, 5 and 9 are the same because the initial position is always z-axis up. For this reason, they will not be shown in the simulation results. The angular components α, β and γ are computed using the Equation 3.20 for each IMU and each posture. These angular components are presented in the Table 4.2, Table 4.3 and Table 4.4, respectively. As previously mentioned in Section 3.3, the quaternion ${}^{G_i}q_{L_j}$ represents the orientation of the local frame (LF) of the i-th IMU in the j-th box pose with respect to its global frame (GF_i). Values of α, β and γ equal to zero for all IMUs during some posture are not presented. Also, the expected (EXP) angles are shown.

Table 4.2 Angle $\boldsymbol{\alpha}$ calculated from ${}^{G_i}\boldsymbol{q}_{\boldsymbol{L_j}}$.

Posture	IMU 1 (°)	IMU 2 (°)	IMU 3 (°)	IMU 4 (°)	IMU 5 (°)	IMU 6 (°)	IMU 7 (°)	EXP (°)
2	89,998	89,998	89,998	89,998	89,999	89,998	90,000	90
3	179,996	179,994	179,993	179,993	179,998	179,994	179,999	180
4	269,984	269,980	269,975	269,975	269,991	269,980	269,996	270
6	-0,628	0,707	-0,785	0,785	-0,471	0,707	-0,314	0
7	-1,257	1,414	-1,571	1,571	-0,942	1,414	-0,628	0
8	-1,885	2,120	-2,356	2,356	-1,414	2,120	-0,942	0

Table 4.4.3 Angle $\boldsymbol{\beta}$ calculated from ${}^{G_i}\boldsymbol{q}_{\boldsymbol{L_j}}$.

Posture	IMU 1 (°)	IMU 2 (°)	IMU 3 (°)	IMU 4 (°)	IMU 5 (°)	IMU 6 (°)	IMU 7 (°)	EXP (°)
2	0,628	-0,707	0,785	-0,785	0,471	-0,707	0,314	0
3	1,257	-1,414	1,571	-1,571	0,942	-1,414	0,628	0
4	1,885	-2,120	2,356	-2,356	1,414	-2,120	0,942	0
6	89,998	89,998	89,998	89,998	89,999	89,998	90,000	90
7	179,996	179,994	179,993	179,993	179,998	179,994	179,999	180
8	269,984	269,980	269,975	269,975	269,991	269,980	269,996	270

Table 4.4.4 Angle $\boldsymbol{\gamma}$ calculated from ${}^{G_i}\boldsymbol{q}_{L_j}$.

Posture	IMU 1 (°)	IMU 2 (°)	IMU 3 (°)	IMU 4 (°)	IMU 5 (°)	IMU 6 (°)	IMU 7 (°)	EXP (°)
1	0,800	-0,900	1,000	-1,000	0,600	-0,900	0,400	0
2	0,628	-0,707	0,785	-0,785	0,471	-0,707	0,314	0
4	-1,885	2,120	-2,356	2,356	-1,414	2,120	-0,942	0
5	0,800	-0,900	1,000	-1,000	0,600	-0,900	0,400	0
6	0,628	-0,707	0,785	-0,785	0,471	-0,707	0,314	0
8	-1,885	2,120	-2,356	2,356	-1,414	2,120	-0,942	0
9	0,800	-0,900	1,000	-1,000	0,600	-0,900	0,400	0
10	90,800	89,100	91,000	89,000	90,600	89,100	90,400	90
11	180,800	179,100	181,000	179,000	180,600	179,100	180,400	180
12	270,800	269,100	271,000	269,000	270,600	269,100	270,400	270

In Section 3.3, the assessment method of static orientation was divided into two stages. The first stage, called Inter-consistency test, corresponds to the evaluation of the difference quaternion ($d_{i,j}$) of all IMU with respect to the average quaternion (${}^{G}\bar{q}_{L_j}$) using the Equation 3.21. Computing the angular components $\alpha(d_{i,j}), \beta(d_{i,j})$ and $\gamma(d_{i,j})$, the errors between the average quaternion (${}^{G}\bar{q}_{L_j}$) and the quaternions calculated for each IMU in each posture (${}^{G_i}q_{L_j}$) were estimated. In Table 4.5 the errors are presented. Note that the initial misalignment of the sensors is exhibited on the angular components depending on the posture. The errors equal to zero are not presented.

Expressing the errors in absolute value, the largest deviation from the average quaternion is presented for the IMUs 3 and 4, as it was expected. Also, the error is equal to the initial misalignment and it is exhibited only in one angular component for each posture.

Table 4.5 Deviations from the average quaternion for each posture.

Posture	Ang. Comp.	IMU 1 (°)	IMU 2 (°)	IMU 3 (°)	IMU 4 (°)	IMU 5 (°)	IMU 6 (°)	IMU 7 (°)
1, 5, 9-12	γ	-0,800	0,900	-1,000	1,000	-0,600	0,900	-0,400
3 and 7	γ	0,800	-0,900	1,000	-1,000	0,600	-0,900	0,400
2	β	0,800	-0,900	1,000	-1,000	0,600	-0,900	0,400
4	β	-0,800	0,900	-1,000	1,000	-0,600	0,900	-0,400
6	α	-0,800	0,900	-1,000	1,000	-0,600	0,900	-0,400
8	α	0,800	-0,900	1,000	-1,000	0,600	-0,900	0,400

To determine the errors between two IMUs, the angular components $\alpha(p_{i,k,j}), \beta(p_{i,k,j})$ and $\gamma(p_{i,k,j})$ were computed. For $\alpha(p_{i,k,j})$, the errors were exhibited only for postures 6 and 8, for $\beta(p_{i,k,j})$, only for the postures 2 and 4 and for $\gamma(p_{i,k,j})$, the errors were exhibited for the other postures. These errors are consistent with the initial misalignments. As a representative

case, the errors presented for the IMU 3 are shown in Table 4.6. As it was expected, the largest deviation was presented from the IMU 3 to the IMU 4, and the error was of 2°.

In conclusion, initial misalignments lead to errors (of the same magnitude) that are exhibited in the angular components, but these errors are presented only in one angular component depending on the box posture.

Table 4.6 Deviations between IMU 3 and other IMUs.

$\alpha(p_{i,k,j})$ for posture 6 and 8							
	IMU 1 (°)	**IMU 2 (°)**	**IMU 3 (°)**	**IMU 4 (°)**	**IMU 5 (°)**	**IMU 6 (°)**	**IMU 7 (°)**
IMU 3 (°)	0,2	1,9	0,0	2,0	0,4	1,9	0,6
$\beta(p_{i,k,j})$ for posture 2 and 4							
	IMU 1 (°)	**IMU 2 (°)**	**IMU 3 (°)**	**IMU 4 (°)**	**IMU 5 (°)**	**IMU 6 (°)**	**IMU 7 (°)**
IMU 3 (°)	0,2	1,9	0,0	2,0	0,4	1,9	0,6
$\gamma(p_{i,k,j})$ for posture 1, 3, 5, 7, 9-12							
	IMU 1 (°)	**IMU 2 (°)**	**IMU 3 (°)**	**IMU 4 (°)**	**IMU 5 (°)**	**IMU 6 (°)**	**IMU 7 (°)**
IMU 3 (°)	0,2	1,9	0,0	2,0	0,4	1,9	0,6

In the second stage of the test, called Self-consistency test, the angular components $\alpha\left({}^{Go}q_G(\theta,\hat{e})\right)$, $\beta\left({}^{Go}q_G(\theta,\hat{e})\right)$ and $\gamma\left({}^{Go}q_G(\theta,\hat{e})\right)$ were calculated using the Equations 3.20 3.23 and 3.24. Remember that this test allows determining the degree of deviation of each IMU in measuring the same global frame regardless of its orientation in space. The misalignments introduced in the previous stage were also applied for this test.

In Table 4.7, the errors in measuring the global frame of each IMU for all posture are shown. The deviations approximately equal to zero are not presented. Observe that in this test, the initial misalignment is exhibited twice for the angular component γ in the postures 2 and 6. And in the other postures, the deviation is exhibited for two angular components. That means for example, that in the posture 1 the initial misalignment of 1° of IMU 3 is exhibited in the angular components β and γ.

Table 4.7 Deviations in measuring the same global frame for each IMU.

$\alpha\left({}^{Go}q_G(\theta,\hat{e})\right)$							
Posture	**IMU 1 (°)**	**IMU 2 (°)**	**IMU 3 (°)**	**IMU 4 (°)**	**IMU 5 (°)**	**IMU 6 (°)**	**IMU 7 (°)**
5	-0,800	0,900	-1,000	1,000	-0,600	0,900	-0,400
7	0,800	-0,900	1,000	-1,000	0,600	-0,900	0,400
$\beta\left({}^{Go}q_G(\theta,\hat{e})\right)$							
Posture	**IMU 1 (°)**	**IMU 2 (°)**	**IMU 3 (°)**	**IMU 4 (°)**	**IMU 5 (°)**	**IMU 6 (°)**	**IMU 7 (°)**
1	0,800	-0,900	1,000	-1,000	0,600	-0,900	0,400
3	-0,800	0,900	-1,000	1,000	-0,600	0,900	-0,400

$\gamma\left({}^{Go}\boldsymbol{q}_{G}(\boldsymbol{\theta},\hat{\boldsymbol{e}})\right)$							
Posture	**IMU 1 (°)**	**IMU 2 (°)**	**IMU 3 (°)**	**IMU 4 (°)**	**IMU 5 (°)**	**IMU 6 (°)**	**IMU 7 (°)**
1	0,800	-0,900	1,000	-1,000	0,600	-0,900	0,400
2	1,600	-1,800	2,000	-2,000	1,200	-1,800	0,800
3	0,800	-0,900	1,000	-1,000	0,600	-0,900	0,400
5	0,800	-0,900	1,000	-1,000	0,600	-0,900	0,400
6	1,600	-1,800	2,000	-2,000	1,200	-1,800	0,800
7	0,800	-0,900	1,000	-1,000	0,600	-0,900	0,400

In conclusion, the errors due to misalignment between sensors (up to 1° of deviation) in the IC and SC tests have a maximum value of 2° when analyzing the angular components of $p_{i,k,j}$ and ${}^{Go}q_{G}(\theta,\hat{e})$.

In this dissertation, the proposal of avoiding the errors due to misalignment between sensors (see Equation 4.1), consists on pre-multiplying the orientation quaternion ${}^{Gi}q_{L_j}$ by the inverse of the initial quaternion for each sensor ${}^{Go}q_{L_O}$. Thus, any misalignment around any axis (x, y or z) is avoided and the errors due to this condition are eliminated. Then the method of assessment of static orientation (in Section 3.3) can be applied.

$$ {}^{Gi}q_{L_j{}_{AL}} = {}^{Gi_O}q^{*}{}_{L_{i_O}} \otimes {}^{Gi}q_{L_j}. \tag{4.1} $$

Case Study 2: Errors smaller than one degree (technical features by manufacturer)

Considering that the manufacturer mentions that the maximum deviation for each sensor unit in static conditions is smaller than 1°, errors of compatible magnitude were introduced. Note that such errors are inherent of the measurement system and this Case Study aims to observe their effects on the calculations of angular displacements.

If errors smaller than 1° are randomly introduced into the measurement of angles, it is observed a similar behavior as shown in the Case Study 1. The largest deviation evaluating $p_{i,k,j}$ and ${}^{Go}q_{G}(\theta,\hat{e})$ is of 2°. To avoid repetitions, a representative case is presented in Table 4.8 and Table 4.9. Experimental results of the static assessment of seven IMUs are presented in Section 4.2.1.

Table 4.8 Deviations between IMU 1 and other IMUs.

Worst case of $\boldsymbol{\alpha}(\boldsymbol{p}_{i,k,j})$							
	IMU 1 (°)	**IMU 2 (°)**	**IMU 3 (°)**	**IMU 4 (°)**	**IMU 5 (°)**	**IMU 6 (°)**	**IMU 7 (°)**
IMU 1 (°)	0°	0,9573°	0,6493°	0,8438°	0,7048°	0,8775°	0,5621°
Worst case of $\boldsymbol{\beta}(\boldsymbol{p}_{i,k,j})$							
	IMU 1 (°)	**IMU 2 (°)**	**IMU 3 (°)**	**IMU 4 (°)**	**IMU 5 (°)**	**IMU 6 (°)**	**IMU 7 (°)**
IMU 1 (°)	0°	0,5033°	0,7155°	0,4390°	0,8433	0.7313°	0,6378°
Worst case of $\boldsymbol{\gamma}(\boldsymbol{p}_{i,k,j})$							
	IMU 1 (°)	**IMU 2 (°)**	**IMU 3 (°)**	**IMU 4 (°)**	**IMU 5 (°)**	**IMU 6 (°)**	**IMU 7 (°)**
IMU 1 (°)	0°	0,7418°	0,6921°	0,7865°	1,9191°	0,8732°	0,9362°

Table 4.9 The worst cases of angles for IMU 1 in measuring the same global frame.

Angle	**Maximum value (°)**
$\boldsymbol{\alpha}\left({}^{G_0}\boldsymbol{q}_{\boldsymbol{G}}(\boldsymbol{\theta},\hat{\boldsymbol{e}})\right)$	0,952°
$\boldsymbol{\beta}\left({}^{G_0}\boldsymbol{q}_{\boldsymbol{G}}(\boldsymbol{\theta},\hat{\boldsymbol{e}})\right)$	0,899°
$\boldsymbol{\gamma}\left({}^{G_0}\boldsymbol{q}_{\boldsymbol{G}}(\boldsymbol{\theta},\hat{\boldsymbol{e}})\right)$	1,903°

4.1.2. Calibration Procedure: Simulation of Two Semi-spheres and Goniometer Set-up

A two semi-sphere and goniometer set-up (see Figure 4.2) was used to explore the sensor-to-body calibration algorithm. Each semi-sphere represents a segment and they are named as S1 and S2. The goniometer that represents the joint is denoted as J1. Using the goniometer, controlled rotations, around z-axis of the IMU 1, are performed. Angles of $0°, \pm 20°, \pm 40°, \pm 60°, \pm 80°$ and $\pm 90°$ are shown in the simulation. These angles correspond to rotations of the S2 with respect to S1. A method to define the orientation of the semi-spheres with respect to the global frame, analogous to that presented in Section 3.4.2, is applied.

Protocol of sensor placement: Three sensors (IMUs 2, 3 and 4) were placed on two semi-spheres and one sensor (IMU 1) was placed on the goniometer as they are shown in Figure 4.2. The IMU 1 is used as the reference, in the same way as the sensor placed on the pelvis for the experiments with human subjects.

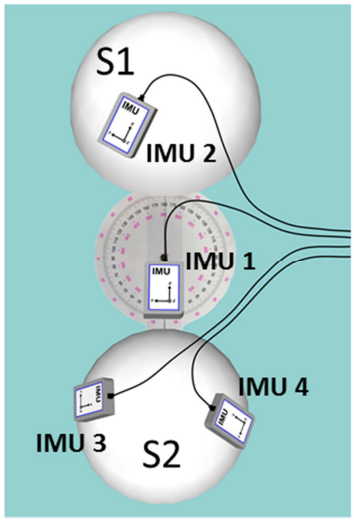

Figure 4.2 Two semi-sphere and goniometer set-up.

In Figure 4.3a, the initial position of IMUs is shown using the software Tech MCS. In Figure 4.3b, the corresponding coordinate systems are shown, where the misalignment between sensors can be observed.

Calibration algorithm and definition of technical frames: For each semi-sphere, a technical frame was defined ($^{G}\boldsymbol{q_{S1}}$ and $^{G}\boldsymbol{q_{S2}}$). In the initial position, these frames are aligned with the reference frame, which is defined by the initial orientation of IMU 1 local frame ($^{G}\boldsymbol{q_{IMU1_0}}$). The equations presented in Section 3.4.2 are applied. Thus, for each semi-sphere, the definitions of initial technical frames are shown in Equation (4.2).

$$^{G}q_{S1_0} = {}^{G}q_{S2_0} = {}^{G}q_{IMU1_0}. \tag{4.2}$$

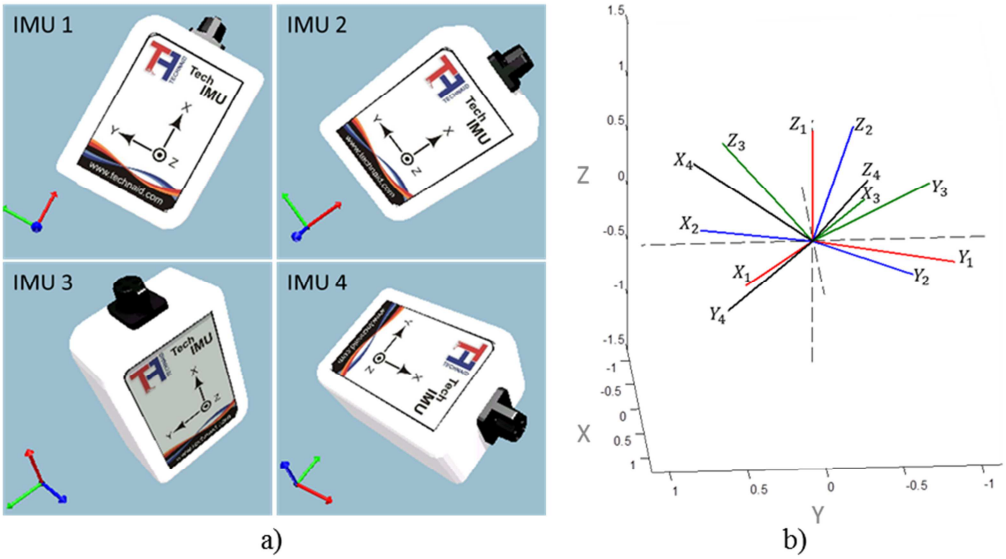

Figure 4.3 a) Orientation of IMUs using Tech MCS and b) Cartesian coordinate system equivalents for each IMU.

Now, the orientation of each sensor with respect to the initial technical frame is computed using Equation (3.28), as shown in Equation (4.3):

$$\begin{aligned} {}^{S1}q_{IMU2} &= {}^{G}q^{*}_{\mathbf{S1_0}} \otimes {}^{G}q_{IMU2} \\ {}^{S2}q_{IMU3} &= {}^{G}q^{*}_{\mathbf{S2_0}} \otimes {}^{G}q_{IMU3}. \\ {}^{S2}q_{IMU4} &= {}^{G}q^{*}_{\mathbf{S2_0}} \otimes {}^{G}q_{IMU4} \end{aligned} \tag{4.3}$$

Having the relative orientation of the sensor to semi-sphere frame in the initial position, the orientation of each semi-sphere frame at any instant of time can be determined as ${}^{G}q_{S1}$, ${}^{G}q_{S2_{IMU3}}$ and ${}^{G}q_{S2_{IMU4}}$. In this case, the frame of S1 is determined using the IMU 2 and the frame of S2 may be determined using the IMU 3 or IMU 4.

The objective of this simulation is to demonstrate that regardless of the initial sensor position, using the method presented in Section 3.4.2, it is possible to estimate the joint angles. Consequently, after applying the method, the angles obtained using the orientation of IMU 3 with respect to IMU 2 are the same if using the orientation of IMU4 with respect to IMU 2. The joints are called J1 (rotation of IMU 3 with respect to IMU 2) and J2 (rotation of IMU 4 with respect to IMU 2).

Joint angles calculation: As the rotations were performed only on one plane, the calculation of the joint angles was simplified using Equation (4.4). Then, the angular component γ is computed using the Equation (3.20).

$$\begin{aligned} J1 &= J2 \\ J1 &= {}^{G}q^{*}_{S1} \otimes {}^{G}q_{S2_{IMU3}} \\ J2 &= {}^{G}q^{*}_{S1} \otimes {}^{G}q_{S2_{IMU4}} \end{aligned} \tag{4.4}$$

S2 was rotated with respect to S1 ($\gamma = 0°, \pm 20°, \pm 40°, \pm 60°, \pm 80°, \pm 90°$). In the Figure 4.4 observe the angular components of IMU 3 and IMU 4 with respect to IMU 2 without applying the sensor-to-segment calibration method. Also, observe that because the IMUs are not aligned, the relative rotations present the three angular components (α, β and γ).

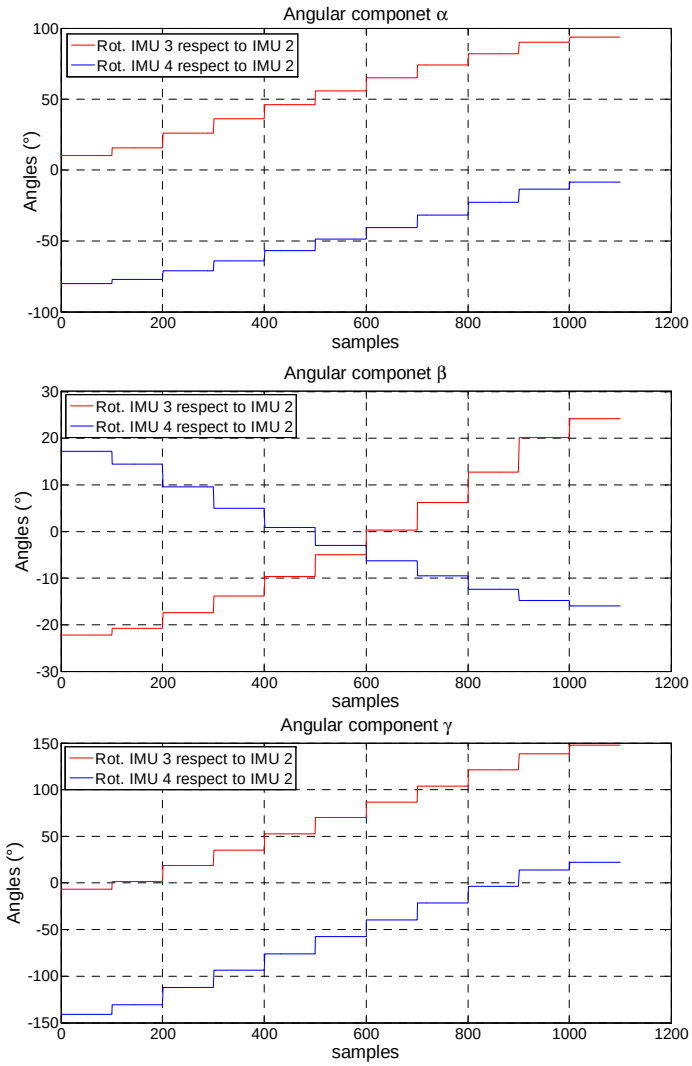

Figure 4.4 Angular components $\boldsymbol{\alpha}$, $\boldsymbol{\beta}$ and $\boldsymbol{\gamma}$, rotations of IMU 3 and 4 with respect to IMU 2 without applying the sensor-to-segment calibration method.

When the calibration method is applied, the angular components α and β are equal to zero, because the rotations of S2 with respect to S1 are performed on one plane around z-axis. That means that only the angular component γ is significant. In the Figure 4.5, the angles γ obtained applying the calibration method are shown.

Note that as α and β angles are equal to zero, they are not graphically presented. Additionally, as γ angles of J1 and J2 are the same, they are presented in different plots in Figure 4.5 to avoid the superposition of curves.

Observe that the values of γ for J1 and J2 are equal to the rotations imposed by simulation. This angular estimation demonstrates the correct performance of the calibration method. Experimental results of the sensor-to-segment calibration method are presented in Section 4.2.2.

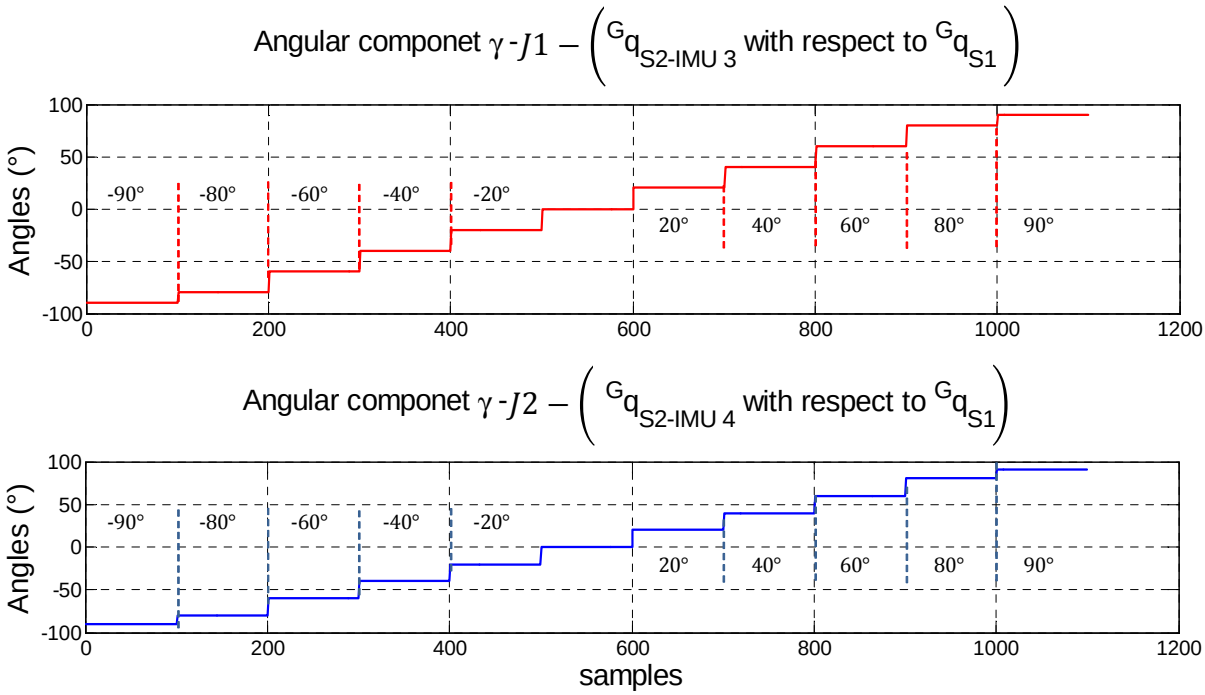

Figure 4.5 Angular component γ calculated from the joints $J1$ and $J2$ applying the sensor-to-segment calibration procedure.

4.2. Experimental Validation

4.2.1. Static Assessment of IMU Sensors

The test to estimate the static accuracy of the IMU was performed on seven Tech IMUs (ID: 88, 89, 90, 91, 92, 101 and 104). This experiment was completed following the considerations shown in Sections 3.3 and 4.1.1. Remember that rotations of $\theta = 0°, 90°, 180°, 270°$ were executed around the x-axis, y-axis and z-axis during the IC test and SC test. Initially, the IMUs were aligned, which allows avoiding any initial misalignment.

At the beginning of the experiment, all sensors measure the same global frame, but posterior measurements will show the performance of the system. Also, remember the numbered postures previously presented in Table 4.1.

According to the Inter-consistency test, in Table 4.10, the worst case of the angular components $\alpha(d_{i,j}), \beta(d_{i,j})$ and $\gamma(d_{i,j})$, expressed in absolute value, is shown. As the IMUs

are enforced to be aligned, the angular components for the postures 1, 5 and 9 are approximately equal to zero.

Table 4.10 IC test – the worst case of the angular components $\boldsymbol{\alpha}, \boldsymbol{\beta}$ and $\boldsymbol{\gamma}$ for each posture
Largest deviation and corresponding ID IMU from the average quaternion.

Posture	$\boldsymbol{\alpha(d_{i,j})}$	$\boldsymbol{\beta(d_{i,j})}$	$\boldsymbol{\gamma(d_{i,j})}$
2	0,490° ID 088	1,908° ID 101	4,786° ID 090
3	0,349° ID 088	0,919° ID 101	3,283° ID 089
4	1,056° ID 101	1,285° ID 104	2,893° ID 089
6	0,989° ID 104	1,070° ID 101	5,561° ID 101
7	0,315° ID 089	0,532° ID 090	1,941° ID 089
8	0,621° ID 104	0,501° ID 101	3,200° ID 088
10	0,272° ID 104	0,448° ID 088	3,709° ID 101
11	0,458° ID 088	0,254° ID 104	3,441° ID 101
12	0,267° ID 104	0,448° ID 088	5,633° ID 101

The largest deviation of the measurements ($\alpha_{max} = 1{,}056°, \beta_{max} = 1{,}908°, \gamma_{max} = 5{,}633°$), on average, were exhibited by the IMU 101. The errors for the angular components α and β are according to manufacturer specifications, but the angular component γ is approximately 6°, which may be critical value to observe the some joint angles on transversal and frontal planes. It is important to mention that movements associated with the angle γ are perpendicular to the direction of the gravity vector. That means that errors in correspondence with the angle γ may be associated to the performance of the gyroscopes and magnetometers.

The maximum angular differences $\alpha(p_{i,k,j}), \beta(p_{i,k,j})$ and $\gamma(p_{i,k,j})$, expressed in absolute value, are shown in Table 4.11, with its corresponding pair of IMUs and posture. The largest difference between two IMUs ($\alpha_{max} = 1{,}816°, \beta_{max} = 2{,}619°, \gamma_{max} = 10{,}200°$) were exhibited for the pairs ID 089-104, ID 089-101 and ID 090-101, respectively. It is possible to observe that the largest differences presented mostly involve the IMUs ID 90 and 101.

Table 4.11 Maximum angular differences between two IMUs and corresponding posture.

Rot	2	3	4	6	7	8	10	11	12
α	(88-90) 0,862°	(88-101) 0,662°	(90-101) 1,554°	(89-104) 1,816°	(89-104) 0,470°	(89-104) 1,802°	(91-104) 0,528°	(88-91) 0,800°	(91-104) 0,516°
β	(89-101) 2,619°	(90-101) 1,836°	(101-104) 2,127°	(90-101) 1,997°	(90-104) 0,895°	(90-104) 0,730°	(88-91) 0,756°	(91-104) 0,490°	(88-91) 0,825°
γ	(90-101) 9,129°	(89-104) 6,491°	(89-90) 4,929°	(90-101) 10,200°	(89-90) 3,625°	(88-92) 5,968°	(92-101) 5,073°	(90-101) 6,642°	(89-101) 8,046°

According to the Self-consistency test, in Table 4.12, the worst and the best case of the angular components $\alpha\left({}^{Go}q_G(\theta,\hat{e})\right)$, $\beta\left({}^{Go}q_G(\theta,\hat{e})\right)$ and $\gamma\left({}^{Go}q_G(\theta,\hat{e})\right)$ are shown. As the angular component γ presents the largest deviations, the errors for all IMU and corresponding posture are shown in Table 4.13.

Table 4.12 SC Test -the worst and best case of $\boldsymbol{\alpha}$, $\boldsymbol{\beta}$ and $\boldsymbol{\gamma}$. Deviations in measuring the same global frame regardless of posture.

Best scenario to estimate the same global regardless of posture IMU 091									
Rot	2	3	4	6	7	8	10	11	12
α	1,977°	0,721°	2,137°	0,165°	0,093°	0,224°	0,741°	0,349°	1,243°
β	1,131°	1,536°	0,802°	1,649°	0,072°	1,417°	1,074°	1,837°	0,686°
γ	0,313°	3,705°	0,375°	2,253°	5,969°	5,896°	2,484°	0,872°	6,567°
Worst scenario to estimate the same global regardless of posture IMU 101									
Rot	2	3	4	6	7	8	10	11	12
α	0,217°	0,488°	1,902°	1,205°	0,212°	0,960°	0,801°	0,070°	0,981°
β	2,172°	2,327°	0,056°	2,210°	0,248°	0,989°	0,825°	1,868°	0,995°
γ	2,704°	0,358°	4,670°	1,422°	14,023°	12,202°	6,407°	12,902°	10,009°

Table 4.13 Deviations of each IMU in correspondence of $\boldsymbol{\gamma}$.

Posture	ID 88	ID 89	ID 90	ID 91	ID 92	ID 101	ID 104
2	1,923	4,210	3,381	0,313	4,759	2,704	2,671
3	4,249	5,393	8,460	3,705	5,595	0,358	3,019
4	4,004	3,551	3,972	0,375	0,214	4,670	0,972
6	4,418	1,305	2,005	2,253	1,585	1,422	4,107
7	8,448	2,237	10,600	5,969	5,809	14,023	6,187
8	1,412	7,324	0,694	5,896	6,709	12,202	4,497
10	8,524	3,007	8,343	2,484	1,905	6,407	4,482
11	8,563	4,885	3,571	0,872	0,263	12,902	5,709
12	10,532	7,231	12,779	6,567	6,374	10,009	6,685

The largest deviation ($\gamma_{max} = 14{,}023°$) was exhibited by the IMU 101 in the posture 7. According to the Table 4.12 and 4.13, the IMUs 89, 91, 92 and 104 present the lower errors. Despite the initial alignment of sensors, it is evident that all IMU do not sense the same global

frame. This condition is exhibited in Table 4.13, where even the best case (IMU 91) presents deviations up to approximately 7°. According to the literature, the deviations in correspondence of the angular component γ may be associated to the performance of magnetometer (PICERNO et al., 2011; BRODIE et al., 2008). Also, Picerno et al., 2011 reported that the angular deviations are smaller when the Kalman filter is not used, as they are directly related to the gyroscope offsets. The angular deviations more than 6° may be critical factor to estimate the angles of joints whose rotation ranges are smaller than 20°, for example, the hip abduction/adduction angles (BENEDETTI et al., 1998; HARTMANN et al., 2010).

4.2.2. Calibration Procedure: Two Semi-spheres and Goniometer Set-up

An experiment to validate the method simulated in Section 4.1.2 was performed. A two semi-spheres and goniometer set-up was implemented (see Figure 4.6). The four IMUs (89, 91, 92 and 104) were used, which were identified as the sensors that presented lower errors in the previous section. The IMU 89 was used as reference, which was placed on the goniometer. The IMU 91 was placed on the semi-sphere S1 and the IMUs 92 and 104 were placed on the semi-sphere S2. Rotations of $\mathbf{0}°, \pm\mathbf{20}°, \pm\mathbf{40}°, \pm\mathbf{60}°, \pm\mathbf{80}°$ and $\pm\mathbf{90}°$ were performed and the experiment was conducted on a wooden table.

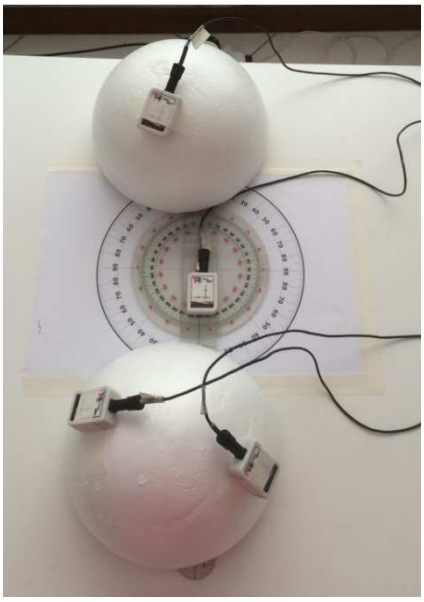

Figure 4.6 The two semi-sphere and goniometer set-up to explore the sensor-to-body segment calibration procedure.

In Figure 4.7, it is possible to observe the angular components of IMU 92 and IMU 104 (placed on S2) with respect to IMU 91 (placed onS1) without applying the sensor-to-segment calibration method. Note that because the IMUs are not aligned, the relative rotations present the three angular components (α, β and γ).

In Figure 4.8, the angles obtained applying the method of calibration are shown. Remember that only the angular component γ is significant. In Figure 4.9, the error between the two joints (J1 and J2) is shown. Maximum values of α and β are also shown in Table 4.14.

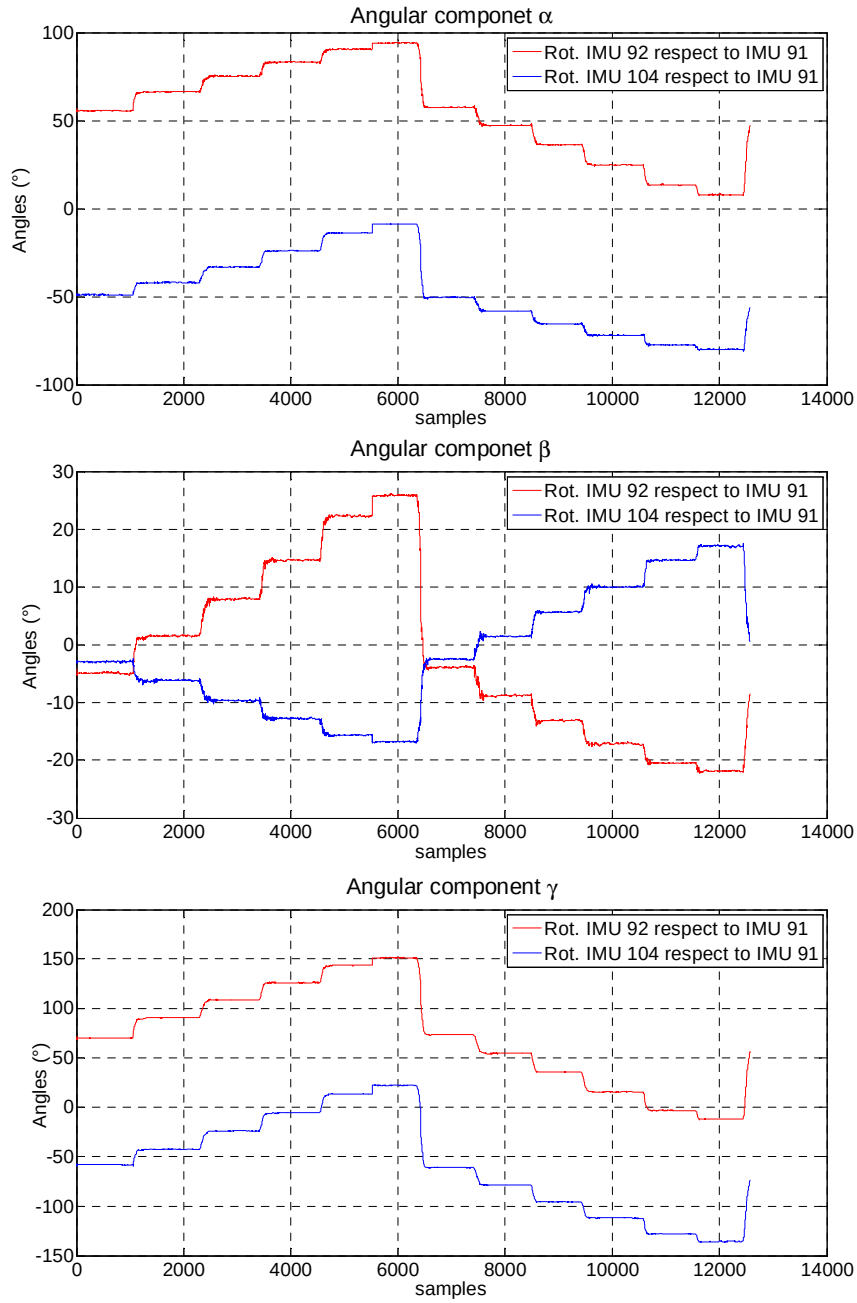

Figure 4.7 Angular components $\boldsymbol{\alpha}, \boldsymbol{\beta}$ and $\boldsymbol{\gamma}$, rotations of IMU 92 and 104 with respect to IMU 91 without applying the sensor-to-segment calibration method.

Table 4.14 Maximum values of the angular component $\boldsymbol{\alpha}$ and $\boldsymbol{\beta}$ for the corresponding joint.

Joint	Angle	Maximum Value (°)
J1	α	0,866
	β	0,822
J2	α	0,694
	β	0,743

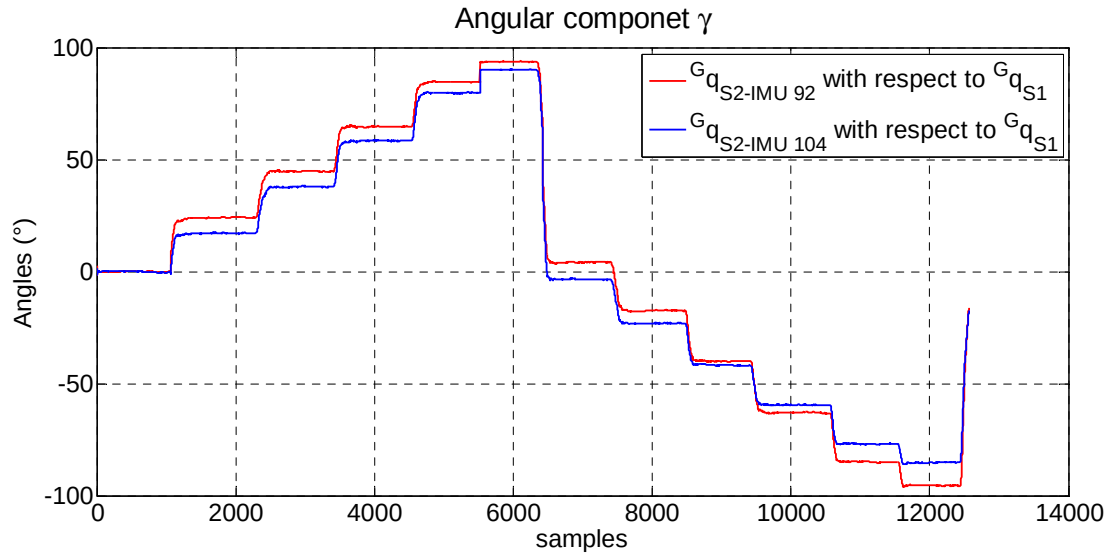

Figure 4.8 Angular component γ of rotations of $(J1)\ {}^{G}q_{S2-IMU92}$ and $(J2)\ {}^{G}q_{S2-IMU104}$ with respect to ${}^{G}q_{S1}$ applying the sensor-to-segment calibration method.

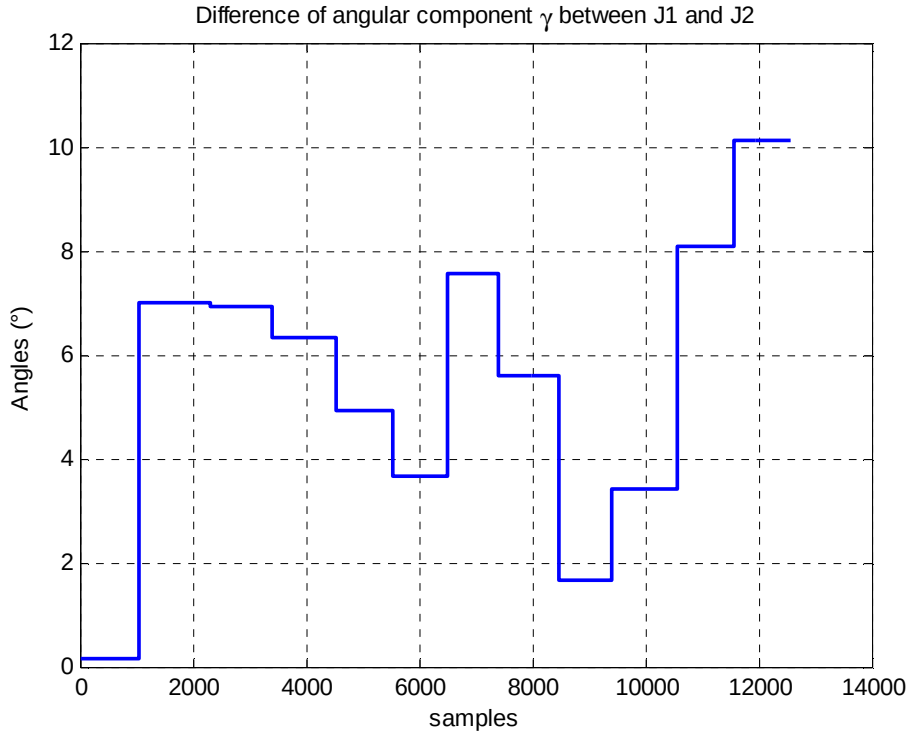

Figure 4.9 Error between $J1$ and $J2$ in correspondence with the angular component γ

Observe that due to the inherent errors of the measurement system, the angular component γ is not the same for the joints J1 and J2. The estimated and expected angles are shown in Table 4.15. The largest difference between the estimated joints was approximately 9.8° (deviation presented for the angle -90°).

The largest error for the expected angle was approximately 5.2° for the angle -90°. This error was exhibited by the joint J1 calculated using the IMUs 91 and 92. Also, observe that the difference between the two estimated joints is not the same through the time and executed rotations.

Table 4.15 Angles $\boldsymbol{\gamma}$ of the J1 and J2 joints

Joint	**0°**	**20°**	**40°**	**60°**	**80°**	**90°**
J1	0°	23,825°	44,738°	64,732°	84,678°	93,748°
J2	0°	17,08°	37,633°	58,574°	79,492°	90,192°
Joint	**0°**	**-20°**	**-40°**	**-60°**	**-80°**	**-90°**
J1	4,045°	-17,367°	-40,056°	-62,653°	-84,791°	-95,182°
J2	-3,491°	-23,130°	-41,624°	-59,502°	-76,743°	-85,345°

4.3. Final considerations

Significant errors were found in the experimental validation of the method for static assessment of the IMU orientation and for the sensor-to-segment calibration procedure. Unlike the results presented in simulations, errors in correspondence to the angular component γ may be a critical factor to accurately estimate the 3D human joint angles. In Table 4.16, the worst cases of errors obtained in this dissertation are compared to those presented by Picerno et al., 2011. Observe that the errors associated with the angle γ are significantly higher than errors associated with the angles α and β.

Table 4.16 Worst cases of errors obtained in this dissertation and presented by Picerno et al., (2011)

	In this dissertation	**By Picerno et al., (2011)**
The worst cases associated to the Inter-consistency test		
$\boldsymbol{\alpha}(\boldsymbol{p}_{i,k,j})$	1,8°	8,0°
$\boldsymbol{\beta}(\boldsymbol{p}_{i,k,j})$	2,6°	4,8°
$\boldsymbol{\gamma}(\boldsymbol{p}_{i,k,j})$	10,2°	11,4°
The worst cases associated to the Self-consistency test		
$\boldsymbol{\alpha}\left({}^{G_0}\boldsymbol{q}_{\boldsymbol{G}}(\boldsymbol{\theta},\hat{\boldsymbol{e}})\right)$	1,9°	4,8°
$\boldsymbol{\beta}\left({}^{G_0}\boldsymbol{q}_{\boldsymbol{G}}(\boldsymbol{\theta},\hat{\boldsymbol{e}})\right)$	2,3°	3,3°
$\boldsymbol{\gamma}\left({}^{G_0}\boldsymbol{q}_{\boldsymbol{G}}(\boldsymbol{\theta},\hat{\boldsymbol{e}})\right)$	14,0°	8,4°

As aforementioned, movements associated with the angle γ are perpendicular to the direction of the gravity vector. This indicates that these errors may be associated to the performance of the magnetometers and gyroscopes. Perhaps the more critical effect of this condition is that IMUs do not sense the same global frame regardless of it orientations, as if the reference frame is moving. Also, it was reported (PICERNO et al., 2011) that the deviations are smaller when the Kalman filter is not used. Thus, these errors may be associated specifically with the fusion algorithms. Therefore, the effort to improve data fusion algorithms and, consequently, reduce these errors is an important and attractive scientific research challenge.

In addition, during the executing of the tests, it was evident that the performance of sensors decreases when ferromagnetic objects are near to them. Nevertheless, it is known that some manufacturers provide software tools to recalibrate the magnetometer in the location of the experiments. Consequently, this may improve the performance of the system.

Chapter 5. Gait Analysis

In this chapter, the results from assessing the sensor-to-body calibration procedure are presented. Five volunteers were tested using the procedure presented in Section 3.4. Once the joint angles are computed, an algorithm to separate each gait cycle was applied based on determining the heel strike as initial event of the gait cycle. In addition, the detection of discrete angular kinematic parameters is performed. Finally, the results are compared with similar studies in the literature.

5.1. Experimental Protocol for Gait Analysis

Figure 5.1 presents a block diagram that summarizes the stages of data processing. Observe that each block represents the explained functions in Section 3.4. The proposal of this dissertation is to define the technic-anatomical frames using the gravity vector and walking direction.

Five volunteers without gait disabilities (3 men and 2 women, 26 ± 4 years old) were enrolled in the validation procedure of this study. Sensors were placed on pelvis and on right lower limb (thigh, shank and foot segments) by a trained physiotherapist as previously mentioned in Section 3.4.1. The sensor placed to the pelvis was aligned with the walking direction. The subjects were asked to keep a straight, upright posture, during 5 seconds before start walking in a 10 meters walkway. This calibration posture allowed the definition of the sensor-to-body alignment according to the algorithm presented in Section 3.4.2. Each subject performed three trials and the three middle gait cycles were extracted for analysis. This methodology was applied to ensure that complete gait cycles were selected excluding motion at the beginning and at the end of the walkway. Nine gait cycles were acquired for each subject.

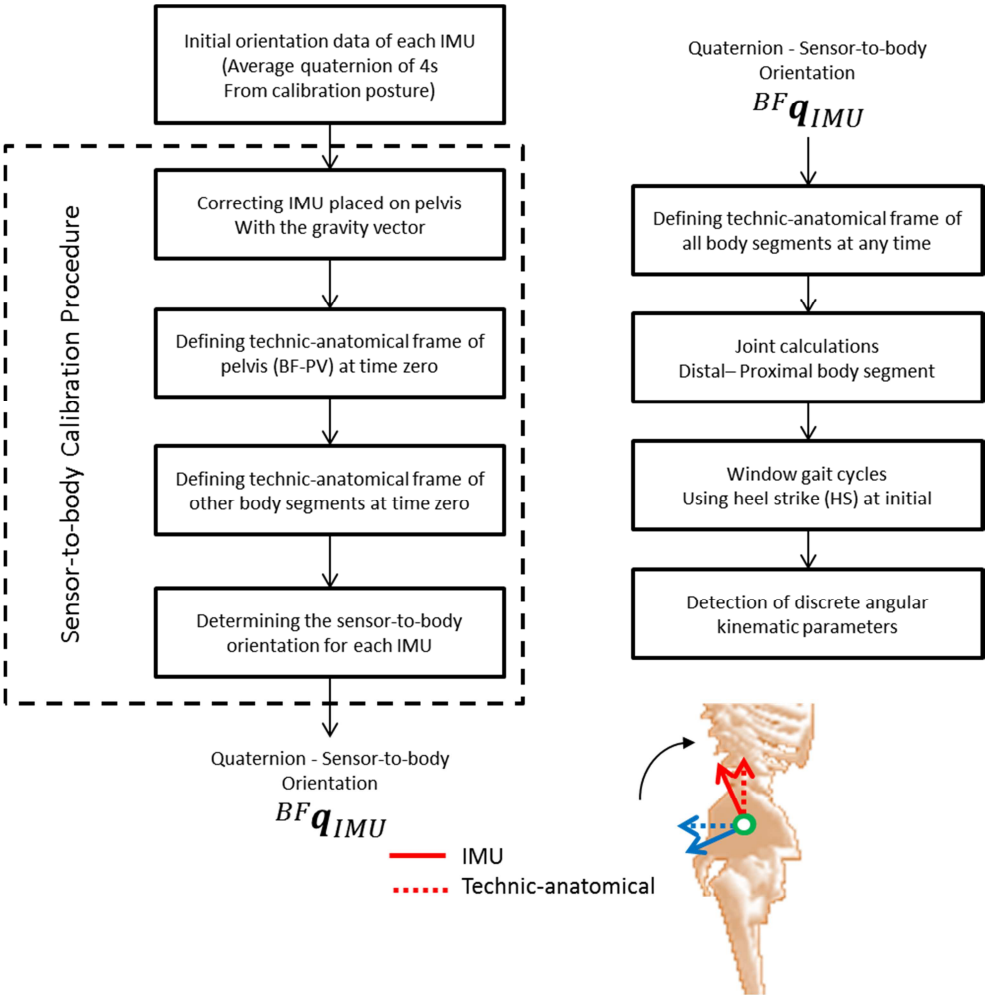

Figure 5.1 Block diagram of the stages of data processing. Including sensor-to-body calibration procedure, joint angle calculations and detection of angular kinematic parameters.

5.2. Results

As a representative case, the results of data processing in different stages are shown for the Subject #1. For the other subjects, only the final results are shown. In Figure 5.2, the joint angles of one trial are shown (Subject #1). The angles are flexion-extension, internal-external rotation and abduction-adduction for the hip and knee joints, and dorsiflexion-plantar flexion and eversion-inversion for the ankle joint. These angles were calculated using the corresponding equations presented in Section 3.4.3. The shaded areas correspond to the three middle gait cycles which are extracted using the heel strike (HS) detection algorithm also described in chapter 3.

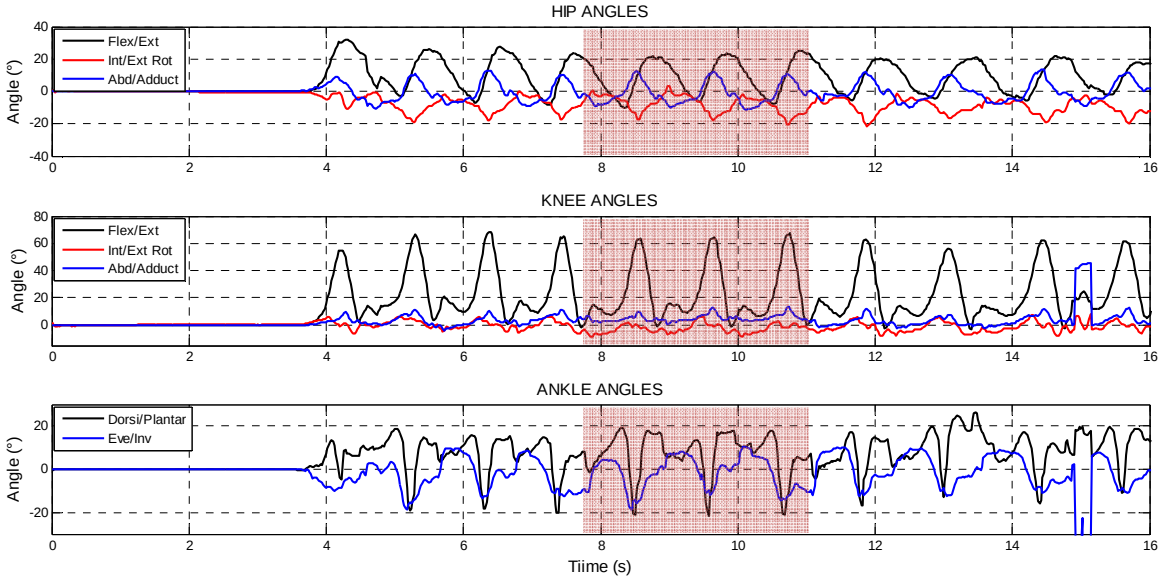

Figure 5.2 Hip, knee and ankle joint angles of one trial of Subject # 1.

In Figure 5.3, the angular velocity computed from the IMU placed on the foot is shown. Observe that HS and toe-off (TO) events are marked using circles and squares, respectively. Note that HS is used as the initial event of a gait cycle. Thus, the HS of the middle of the trial is identified and the three middle gait cycles can be extracted and expressed in percentage of gait cycle. In Figure 5.4, the three middle gait cycles for three trials are shown. Observe lines that separate the cycles corresponding to the HS events. Finally, for each joint angle a total of nine gait cycles is computed.

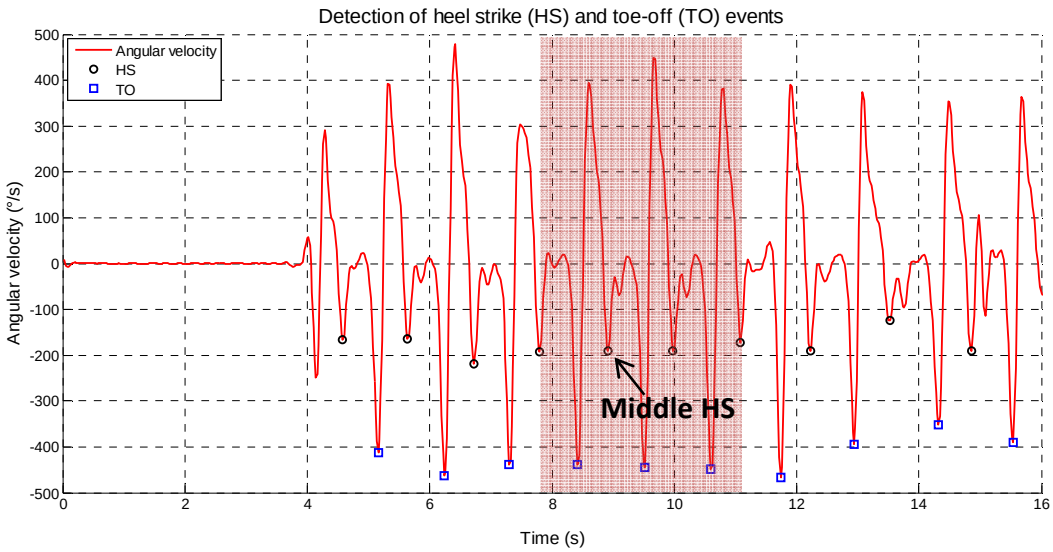

Figure 5.3 Angular velocity computed from IMU placed on foot to determine HS (circles) and TO (squares) events for Subject # 1 during first trial.

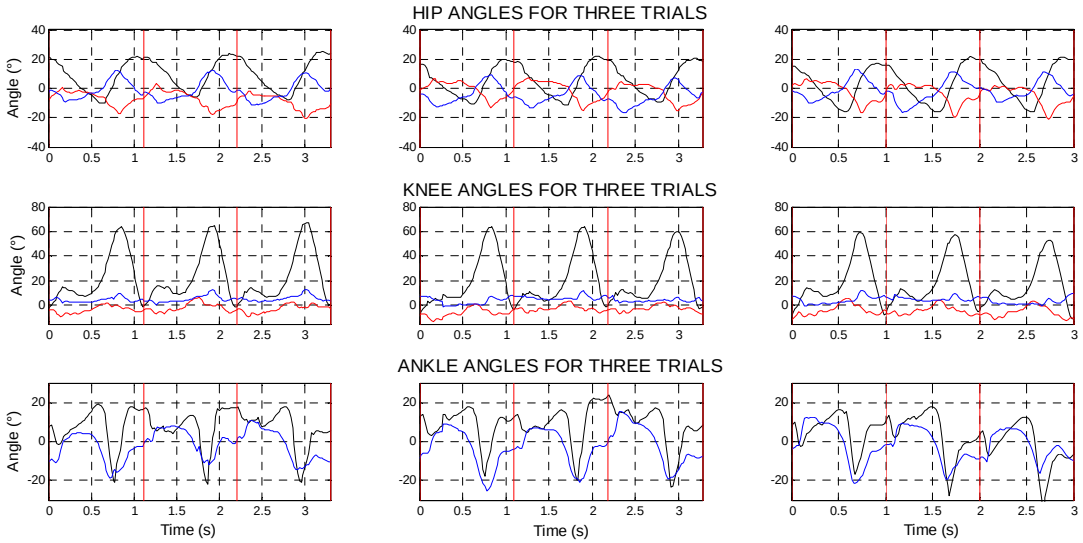

Figure 5.4 Three middle gait cycle from three trials of Subject # 1.

Discrete angular kinematic parameters were used in this dissertation to analyze the gait pattern in subjects without gait disabilities. In Table 5.1, the joint angle parameters are shown according to the study presented by Benedetti et al. (1998).

Table 5.1 Joint angles parameter for gait analysis.

Hip angles parameters (Deg)		**Knee angles parameters (Deg)**		**Ankle angles parameters (Deg)**	
H1	Flexion at heel strike	**K1**	Flexion at heel strike	**A1**	Flexion at heel strike
H2	Max. flex. at loading response	**K2**	Max. flex. at loading response	**A2**	Max. plant. flex. at loading response
H3	Max. ext. in stance phase	**K3**	Max. ext. in stance phase	**A3**	Max. dorsiflexion in stance phase
H4	Flexion at toe off	**K4**	Flexion at toe off	**A4**	Flexion at toe off
H5	Max. flex. In swing phase	**K5**	Max. flex. In swing phase	**A5**	Max. dorsiflexion in swing phase
H6	Total sagittal plane excursion	**K6**	Total sagittal plane excursion	**A6**	Total sagittal plane excursion
H7	Total coronal plane excursion	**K7**	Total coronal plane excursion	**A7**	Total coronal plane excursion
H8	Max. add. in stance phase	**K8**	Max. add. in stance phase	**A8**	Max. eversion in stance phase
H9	Max. abd. in swing phase	**K9**	Max. add. in swing phase	**A9**	Max. inversion in swing phase
H10	Total transverse plane excursion	**K10**	Total transverse plane excursion		
H11	Max. int. rot. in stance phase	**K11**	Max. int. rot. in stance phase		
H12	Max ext. rot. in swing phase	**K12**	Max ext. rot. in swing phase		

In Figure 5.5, the angular parameters H1-H5, K1-K5 and A1-A5 are shown as an example for Subject # 1. Note that those angular parameters correspond to movements on the sagittal plane. In Figure 5.6, the angular parameters H8-H9, K8-K9 and A8-A9 are shown for the Subject # 1. These parameters correspond to movements on the frontal plane. In Figure 5.7, the angular parameters H11-H12 and K11-K12 are shown for the Subject # 1. These parameters correspond to movements on the transverse plane.

Once the joint angles on three planes and the discrete angular kinematic parameters are computed, descriptive statistics was used to expose the results of each subject. In Figure 5.8, the mean and standard deviation of the joint angles using the nine gait cycles for Subject #1 are shown.

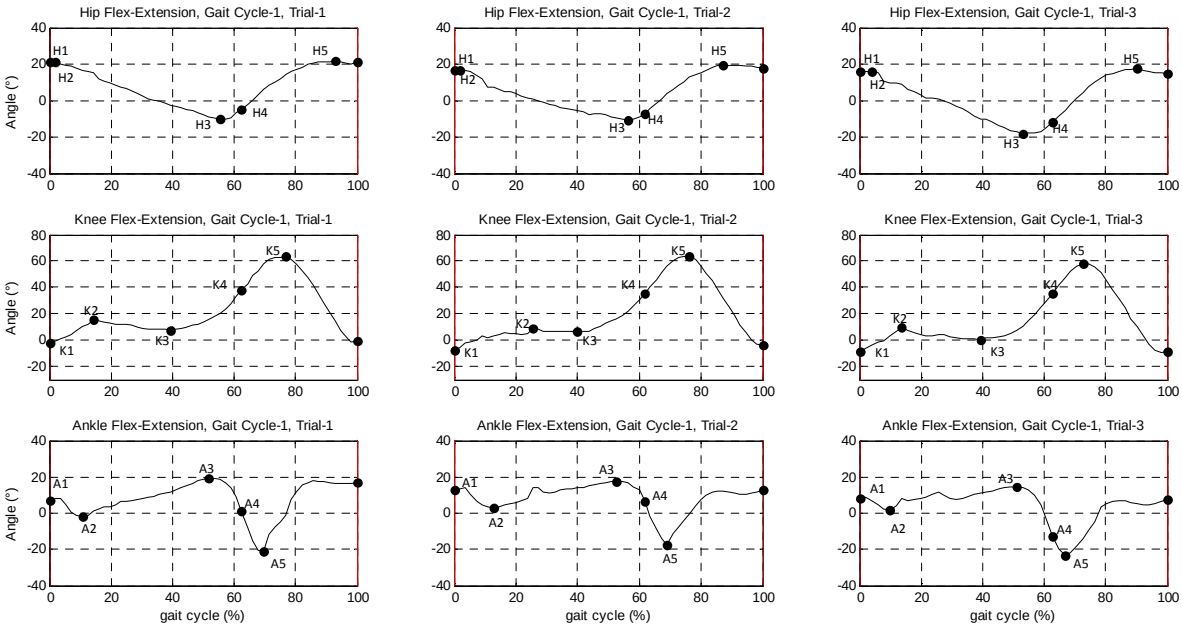

Figure 5.5 Joint flex-extension angles expressed in percentage of gait cycle and discrete angular kinematic parameters H1-H5, K1-K5 and A1-A5 in correspondence with the movements on sagittal plane.

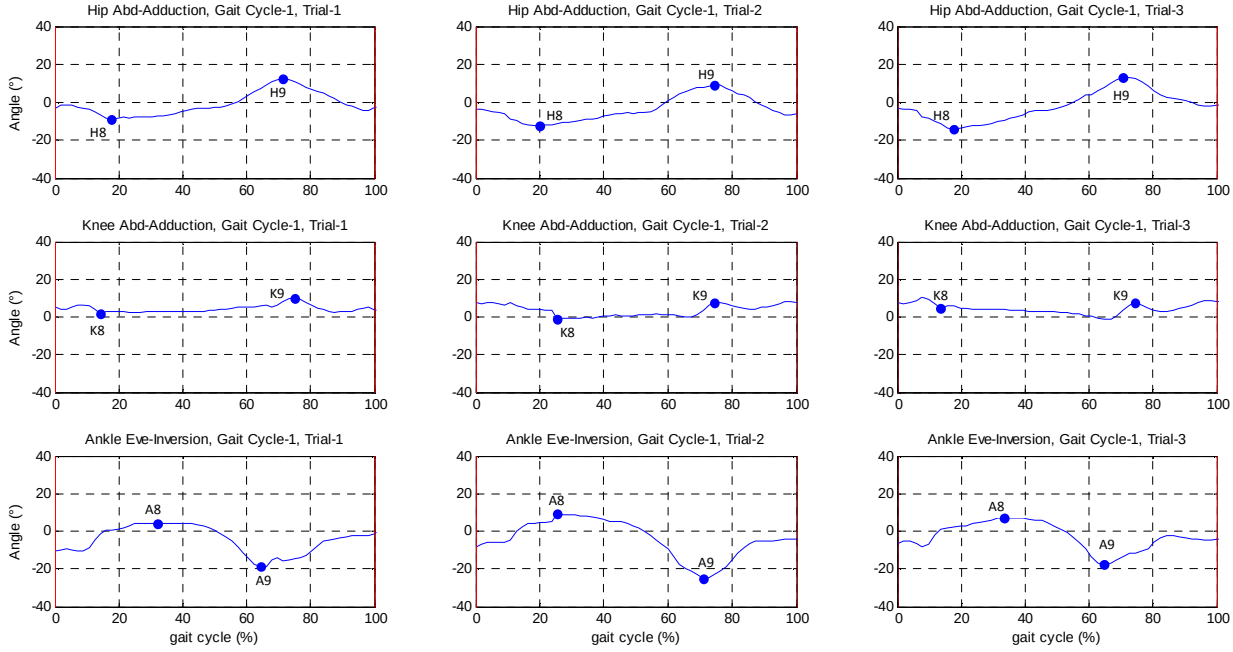

Figure 5.6 Joint abd-adduction angles expressed in percentage of gait cycle and discrete angular kinematic parameters H8-H9, K8-K9 and A8-A9 in correspondence with the movements on frontal plane.

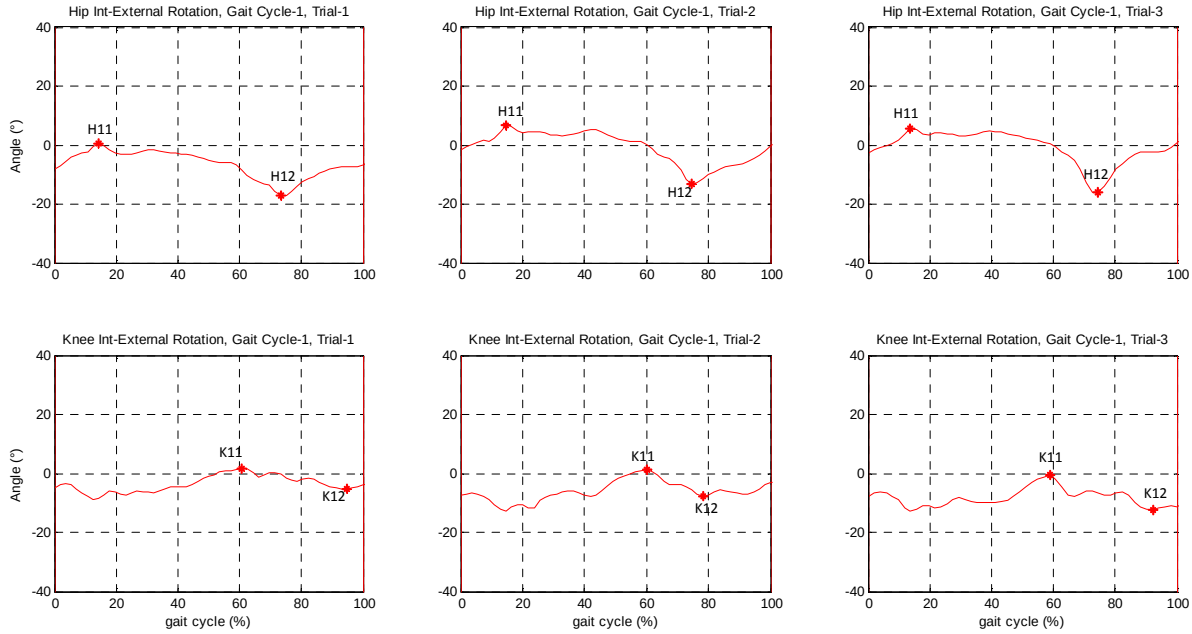

Figure 5.7 Joint int-external rotation angles expressed in percentage of gait cycle and discrete angular kinematic parameters H11-H12 and K11-K12 and in correspondence with the movements on transversal plane.

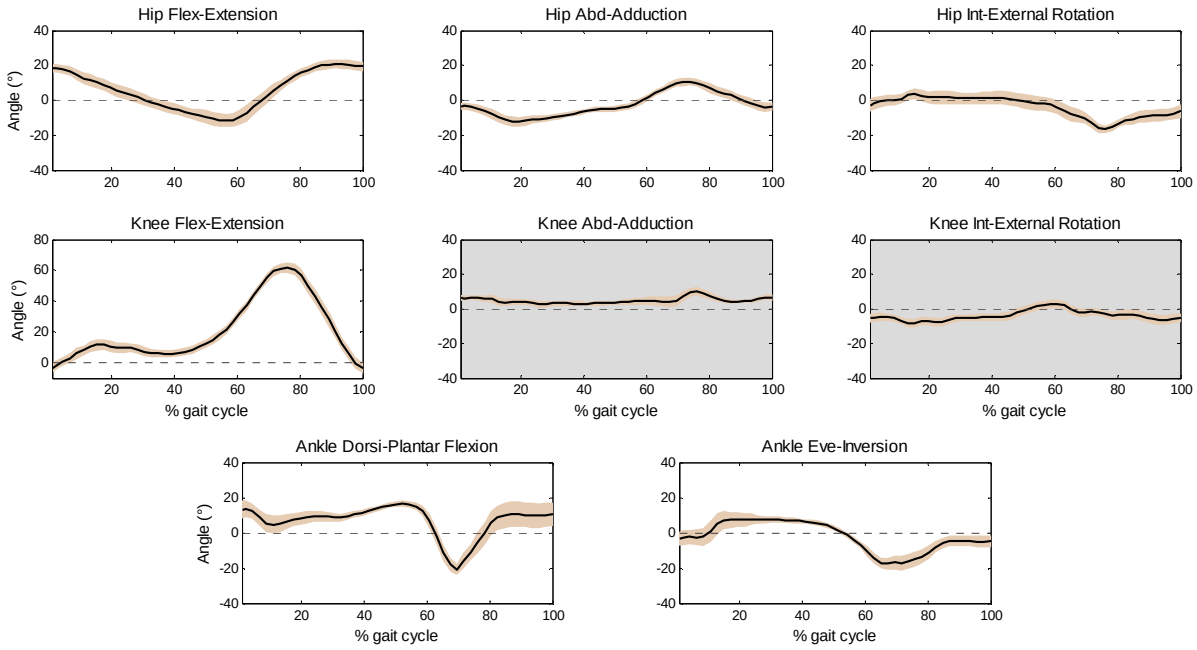

Figure 5.8 Joint angular kinematics in stride percentage (from HS to HS) of Subject # 1. Nine gait cycles were summarized by black curve (mean) and orange stripe (± std).

Observe that knee abd-adduction and int-external rotation plot are reported over a gray background because these rotations are not reliable due to the soft-tissue artifact (FERRARI et al., 2010; PALERMO et al., 2014). In Table 5.2, the mean and standard deviation of the discrete angular parameters (Subject # 1) obtained by the proposed algorithm are shown. The largest standard deviation (6.4 °) for the Subject # 1 is observed in ankle dorsi-plantar flexion.

Table 5.2 Mean and standard deviation of the gait analysis parameters for Subject # 1.

Parameter	Mean	± STD	Parameter	Mean	± STD	Parameter	Mean	± STD
H1 (°)	18,2	2,7	**K1 (°)**	-4,5	3,6	**A1 (°)**	12,9	5,4
H2 (°)	18,3	2,6	**K2 (°)**	12,9	2,5	**A2 (°)**	3,2	3,8
H3 (°)	-11,7	4,0	**K3 (°)**	5,6	2,7	**A3 (°)**	16,7	1,8
H4 (°)	-6,6	5,0	**K4 (°)**	38,5	3,2	**A4 (°)**	-4,0	6,4
H5 (°)	21,1	2,6	**K5 (°)**	62,0	3,4	**A5 (°)**	-21,4	3,2
H6 (°)	32,7	2,7	**K6 (°)**	66,8	2,5	**A6 (°)**	39,9	4,4
H7 (°)	23,6	2,4	**K7 (°)**	12,7	2,3	**A7 (°)**	28,1	5,3
H8 (°)	-12,6	2,8	**K8 (°)**	2,2	2,2	**A8 (°)**	9,3	3,3
H9 (°)	11,0	2,2	**K9 (°)**	10,1	2,5	**A9 (°)**	-18,8	3,9
H10 (°)	21,3	2,0	**K10 (°)**	12,3	2,5	Largest deviation ± 6,4° (Presented for A4)		
H11 (°)	4,0	3,1	**K11 (°)**	3,0	2,2			
H12 (°)	-16,9	2,3	**K12 (°)**	-6,9	2,8			

In Figure 5.9, the mean and standard deviation of the joint angles using the nine gait cycles for Subject # 2 are shown. The corresponding mean and standard deviation of the angular parameters for the Subject # 2 are presented in Table 5.3. The largest standard deviation (6.2°) for the Subject # 2 is observed in ankle eve-inversion.

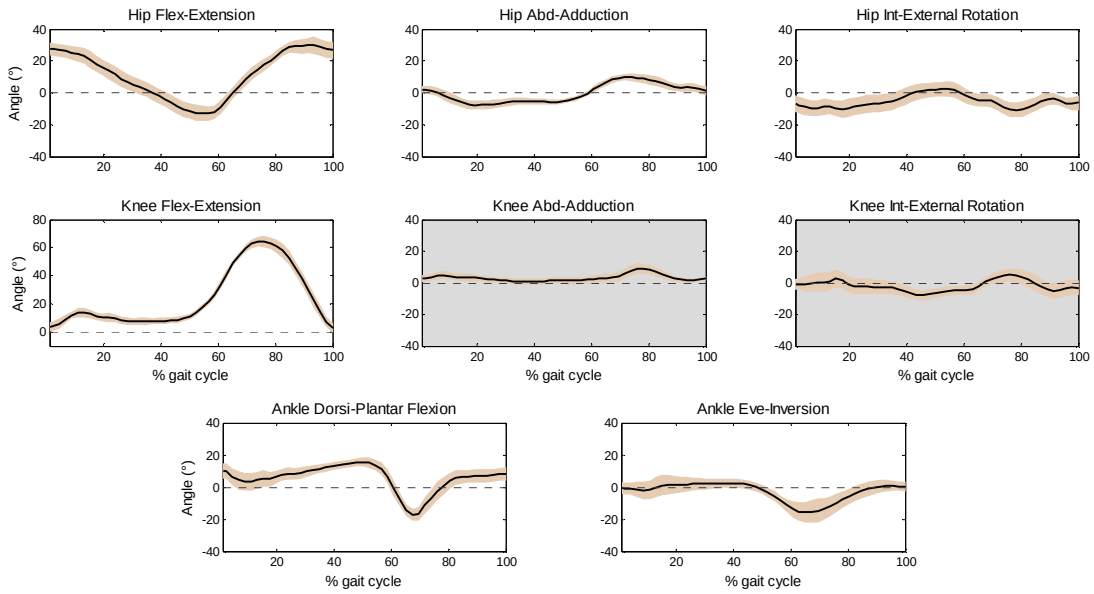

Figure 5.9 Joint angular kinematics in stride percentage (from HS to HS) of Subject # 2. Nine gait cycles were summarized by black curve (mean) and orange stripe (± std).

Table 5.3 Mean and standard deviation of the gait analysis parameters for Subject # 2.

Parameter	Mean	± STD	Parameter	Mean	± STD	Parameter	Mean	± STD
H1 (°)	27,8	4,1	**K1 (°)**	3,2	3,1	**A1 (°)**	9,9	4,8
H2 (°)	27,2	4,1	**K2 (°)**	14,7	3,6	**A2 (°)**	1,6	5,1
H3 (°)	-13,2	4,8	**K3 (°)**	7,1	2,3	**A3 (°)**	15,9	3,0
H4 (°)	-3,7	4,6	**K4 (°)**	43,2	4,7	**A4 (°)**	-8,8	5,3
H5 (°)	30,8	4,8	**K5 (°)**	64,8	3,6	**A5 (°)**	-18,7	3,7
H6 (°)	44,8	2,2	**K6 (°)**	67,2	4,3	**A6 (°)**	34,9	2,7
H7 (°)	18,0	1,6	**K7 (°)**	10,5	3,5	**A7 (°)**	21,4	5,6
H8 (°)	-8,1	2,6	**K8 (°)**	0,2	1,6	**A8 (°)**	3,9	4,0
H9 (°)	9,9	2,1	**K9 (°)**	9,3	3,4	**A9 (°)**	-16,8	6,2
H10 (°)	15,3	1,8	**K10 (°)**	14,1	0,7	Largest deviation ± 6,2° (Presented for A9)		
H11 (°)	2,6	4,8	**K11 (°)**	3,2	5,2			
H12 (°)	-11,1	4,6	**K12 (°)**	-6,1	4,2			

In Figure 5.10, the mean and standard deviation of the joint angles using the nine gait cycles for Subject # 3 are shown. The corresponding mean and standard deviation of the angular parameters for the Subject # 3 are presented in Table 5.4. The largest standard deviation (6.0°) for the Subject # 3 is observed in ankle eve-inversion.

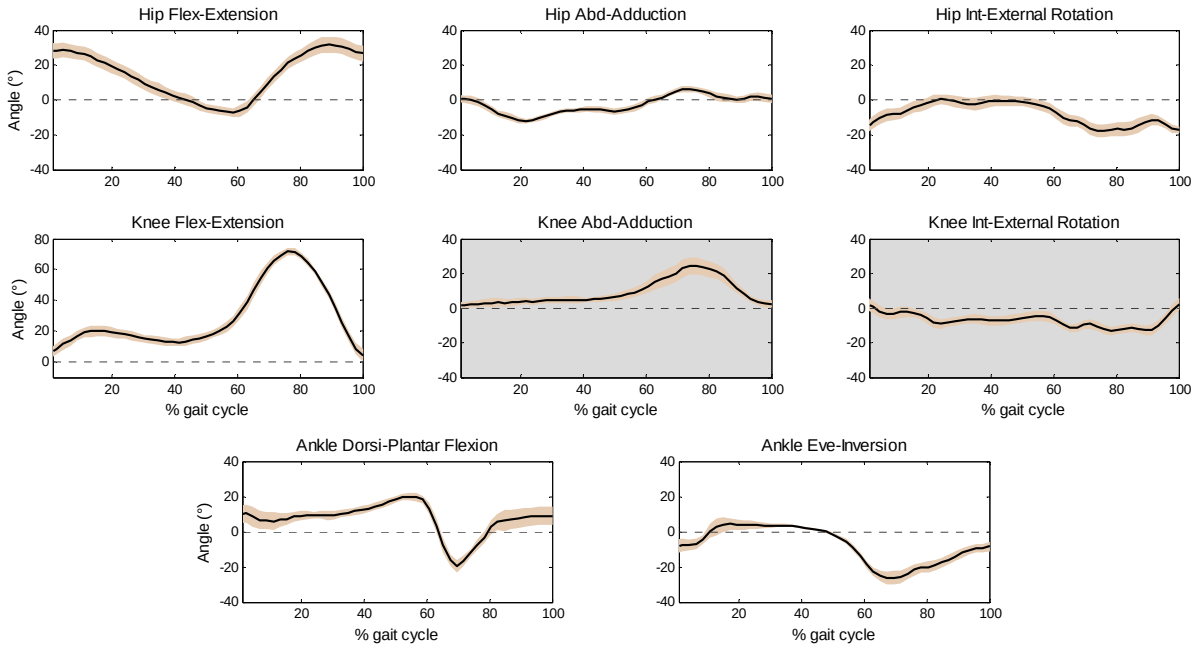

Figure 5.10 Joint angular kinematics in stride percentage (from HS to HS) of Subject # 3. Nine gait cycles were summarized by black curve (mean) and orange stripe (± std).

Table 5.4 Mean and standard deviation of the gait analysis parameters for Subject # 3.

Parameter	Mean	± STD	Parameter	Mean	± STD	Parameter	Mean	± STD
H1 (°)	28,2	4,7	**K1 (°)**	5,5	3,5	**A1 (°)**	9,5	5,2
H2 (°)	29,0	4,2	**K2 (°)**	20,9	3,7	**A2 (°)**	4,1	2,9
H3 (°)	-7,6	2,6	**K3 (°)**	12,4	2,5	**A3 (°)**	20,3	2,1
H4 (°)	-3,4	3,6	**K4 (°)**	40,2	5,5	**A4 (°)**	1,0	6,0
H5 (°)	32,2	4,5	**K5 (°)**	72,6	2,2	**A5 (°)**	-20,6	3,5
H6 (°)	40,6	3,2	**K6 (°)**	76,4	4,8	**A6 (°)**	40,9	2,4
H7 (°)	18,8	0,8	**K7 (°)**	26,2	4,8	**A7 (°)**	32,9	3,6
H8 (°)	-12,3	1,5	**K8 (°)**	1,0	1,9	**A8 (°)**	5,5	2,8
H9 (°)	6,5	1,6	**K9 (°)**	24,6	4,8	**A9 (°)**	-27,4	3,3
H10 (°)	21,4	2,8	**K10 (°)**	18,5	4,0	Largest deviation ± 6,0° (Presented for A4)		
H11 (°)	0,5	3,0	**K11 (°)**	2,8	3,5			
H12 (°)	-18,8	3,0	**K12 (°)**	-14,6	2,2			

In Figure 5.11, the mean and standard deviation of the joint angles using the nine gait cycles for Subject # 4 are shown. The corresponding mean and standard deviation of the angular parameters for the Subject # 4 are presented in Table 5.5. The largest standard deviation (10.4°) for the Subject # 2 is observed in knee int-external rotation, but such as previously mentioned, these rotations are not reliable. Thus, discarding those rotations, the largest standard deviation (7.2 °) is observed in ankle dorsi-plantar flexion.

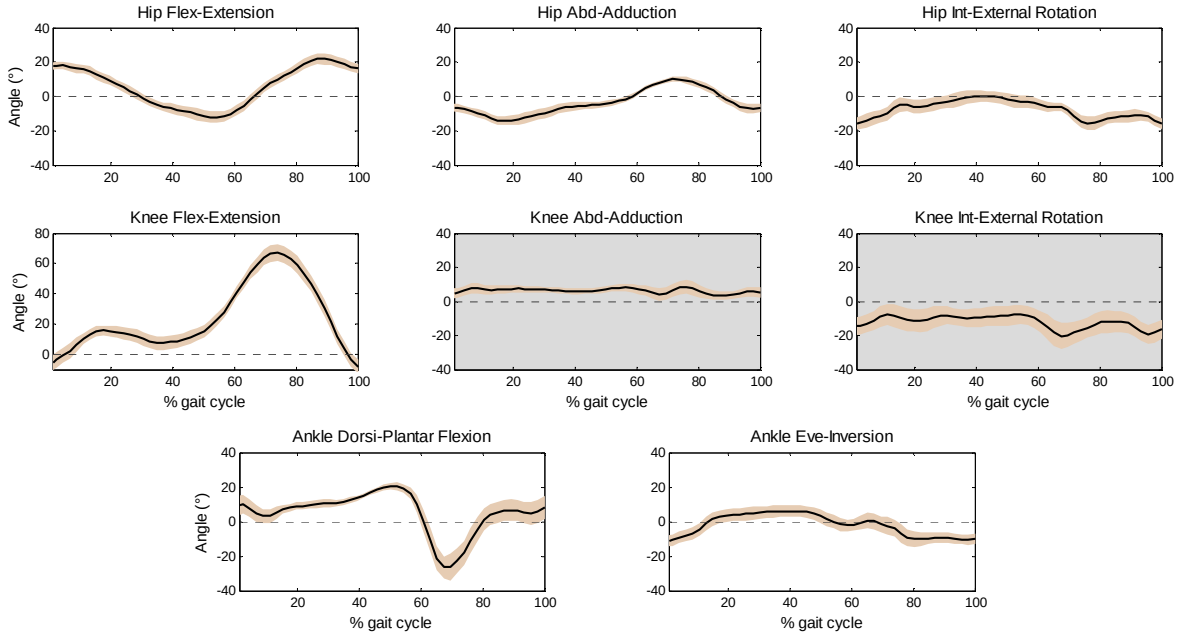

Figure 5.11 Joint angular kinematics in stride percentage (from HS to HS) of Subject # 4. Nine gait cycles were summarized by black curve (mean) and orange stripe (± std).

Table 5.5 Mean and standard deviation of the gait analysis parameters for Subject # 4.

Parameter	Mean	± STD	Parameter	Mean	± STD	Parameter	Mean	± STD
H1 (°)	17,4	2,0	**K1 (°)**	-7,0	5,0	**A1 (°)**	8,8	5,8
H2 (°)	18,3	2,3	**K2 (°)**	15,9	3,3	**A2 (°)**	2,1	4,2
H3 (°)	-12,2	3,3	**K3 (°)**	7,0	4,2	**A3 (°)**	20,6	2,0
H4 (°)	-4,9	3,6	**K4 (°)**	49,1	4,9	**A4 (°)**	-13,4	7,2
H5 (°)	21,9	3,1	**K5 (°)**	67,5	5,3	**A5 (°)**	-28,1	6,9
H6 (°)	34,4	2,1	**K6 (°)**	76,6	4,1	**A6 (°)**	48,7	6,2
H7 (°)	25,1	2,0	**K7 (°)**	13,3	3,2	**A7 (°)**	20,9	1,7
H8 (°)	-14,7	2,8	**K8 (°)**	2,8	1,6	**A8 (°)**	6,6	3,3
H9 (°)	10,4	1,5	**K9 (°)**	10,0	2,9	**A9 (°)**	-12,5	3,3
H10 (°)	20,3	2,7	**K10 (°)**	29,0	10,4	Largest deviation ± 7,2° (Presented for A4)		
H11 (°)	0,6	3,3	**K11 (°)**	-6,4	5,8			
H12 (°)	-16,5	3,1	**K12 (°)**	-22,1	5,8			

In Figure 5.12, the mean and standard deviation of the joint angles using the nine gait cycles for Subject # 5 are shown. The corresponding mean and standard deviation of the angular parameters for the Subject # 5 are presented in Table 5.6. The largest standard deviation (5.4°) for the Subject # 5 is observed in ankle flex-extension.

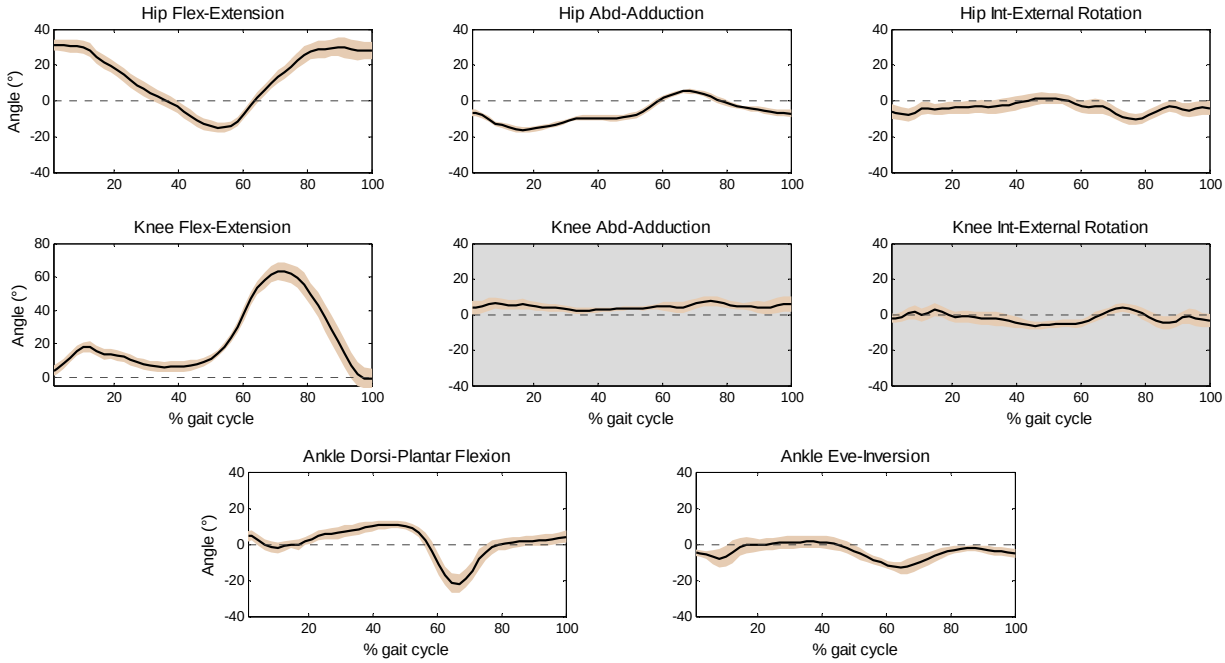

Figure 5.12 Joint angular kinematics in stride percentage (from HS to HS) of Subject # 5. Nine gait cycles were summarized by black curve (mean) and orange stripe (± std).

Table 5.6 Mean and standard deviation of the gait analysis parameters for Subject # 5.

Parameter	Mean	± STD	Parameter	Mean	± STD	Parameter	Mean	± STD
H1 (°)	31,2	3,2	**K1 (°)**	2,9	3,1	**A1 (°)**	3,9	3,0
H2 (°)	29,9	3,9	**K2 (°)**	18,1	3,0	**A2 (°)**	-2,0	3,1
H3 (°)	-15,0	2,8	**K3 (°)**	6,1	3,1	**A3 (°)**	10,9	2,2
H4 (°)	-2,7	2,6	**K4 (°)**	38,2	3,8	**A4 (°)**	-11,3	5,4
H5 (°)	29,4	4,7	**K5 (°)**	63,3	5,1	**A5 (°)**	-21,9	5,2
H6 (°)	47,6	1,6	**K6 (°)**	67,1	3,7	**A6 (°)**	34,6	4,2
H7 (°)	21,9	1,7	**K7 (°)**	11,5	1,1	**A7 (°)**	17,0	2,5
H8 (°)	-16,3	1,5	**K8 (°)**	2,2	1,7	**A8 (°)**	1,3	3,3
H9 (°)	5,2	1,4	**K9 (°)**	7,1	2,8	**A9 (°)**	-13,3	3,5
H10 (°)	13,1	3,3	**K10 (°)**	12,2	2,1	Largest deviation ± 5,4° (Presented for A4)		
H11 (°)	1,5	3,0	**K11 (°)**	-3,0	3,7			
H12 (°)	-10,4	3,3	**K12 (°)**	4,0	2,4			

5.3. Discussion

In this M. Sc. Dissertation, a sensor-to-body calibration procedure for gait analysis based on IMUs was proposed. The procedure is based on the data processing collected before the walking trial. The proposed strategy was designed for simplicity and ease-of-use in a clinical setting.

The proposal is based on the correcting of the IMU orientations with the gravity vector and walking direction. Similar procedures have been proposed in the literature, nevertheless, performing movements keeping a firm upright posture to determine the direction of rotation axis (as proposed by CUTTIE et al. (2010)), or to maintain the same orientation between two postures (as proposed by PALERMO et al. (2014)), may not be simple task to be performed by subjects with motor disabilities or without the help of specialist.

In order to compare and verify that the obtained joint angles (mean and standard deviation) are consistent with those presented in the reference literature (BENEDETTI et al., 1998; PICERNO et al., 2008; FAVRE et al., 2009; FERRARI et al., 2010; PALERMO et al., 2014), including both signal behavior and the similar intervals at which it occurs, the results presented by Benedetti et al. (1998) are shown in Table 5.7. It is worth mentioning that the study conducted by Benedetti et al. (1998) used Elite system (BTS, Milano, Italy), a system based on optical cameras.

Table 5.7 Mean and standard deviation of the gait analysis parameters by Benedetti et al. (1998).

Parameter	Mean	± STD	Parameter	Mean	± STD	Parameter	Mean	± STD
H1 (°)	26,7	5,36	**K1 (°)**	0,39	4,87	**A1 (°)**	-3,99	5,97
H2 (°)	28,9	5,7	**K2 (°)**	17,93	7,65	**A2 (°)**	-12,67	4,93
H3 (°)	-9,98	5,09	**K3 (°)**	4,91	4,56	**A3 (°)**	10,92	5,67
H4 (°)	-3,68	5,75	**K4 (°)**	36,61	7,59	**A4 (°)**	-12,59	8,44
H5 (°)	29,82	4,81	**K5 (°)**	65,65	5,23	**A5 (°)**	-22,64	6,89
H6 (°)	39,8	4,28	**K6 (°)**	60,74	5,09	**A6 (°)**	33,73	6,85
H7 (°)	11,06	2,64	**K7 (°)**	10,6	3,8	**A7 (°)**	13,3	5,02
H8 (°)	-5,4	3,3	**K8 (°)**	3,07	3,61	**A8 (°)**	3,24	4
H9 (°)	5,45	3,28	**K9 (°)**	-4,05	10,42	**A9 (°)**	-9,16	4,44
H10 (°)	13,58	3,98	**K10 (°)**	13,9	5,09			
H11 (°)	3,42	4,87	**K11 (°)**	5,25	5,3			
H12 (°)	-8,48	5,95	**K12 (°)**	-8,36	5,8			

The sensor-to-body calibration procedure has proved to be suitable to estimate joint angles of the hip, knee and ankle in healthy subjects during free walking. According to the results of each subject, it is possible to identify characteristics of each individual.

Even though the system limitations mentioned in Section 4.3, the sensor-to-body calibration procedure is suitable to estimate the behavior of human joints, especially on the sagittal plane (flexion-extension) where the largest amplitude of movements occurs. By comparing the information obtained in this dissertation with the literature (BENEDETTI et al., 1998, CUTTI et al. 2010; PALERMO et al., 2014), it is clear that the angular patterns are coherent and within the intervals established by mean and standard deviations. Some examples are shown in Table 5.6, where the results in this dissertation are included within the findings of Benedetti et al. (1998).

Table 5.8 Mean and standard deviation of discrete angular kinematic parameters compared with the literature.

	Findings of Benedetti et al. (1998)		**This dissertation**	
Parameter	Mean	± STD	Mean	± STD
H1 (°)	26,7	5,36	24,6	3,34
H3 (°)	-9,98	5,09	-11,94	3,50
H5 (°)	29,82	4,81	27,08	3,94
K1 (°)	0,39	4,87	0,94	3,66
K3 (°)	4,91	4,56	7.64	2,96
K5 (°)	65,65	5,23	66,1	3,92
A3 (°)	10,92	5,67	16,88	2,22
A5 (°)	-22,64	6,89	-22,14	4,50

The knee motions on the frontal and transverse planes were not consistent with the findings of Benedetti et al. (1998). However, previous research has shown that movements in these planes have a broader range of variation, which includes the interval of our results (CUTTI et al., 2010; PALERMO et al., 2014).

Interestingly, the results obtained with the developed algorithm presented low standard deviations, which means that estimated measures were consistent across trials. Further investigation on the reliability of this procedure and also internal/external validity of the results will be performed in the future.

5.4. Conclusion

A novel, simple and fast calibration procedure is the main contribution presented in this chapter to address the problem of body-to-sensor alignment in IMU-based gait analysis. Such procedure provides tridimensional kinematics of hip, knee and ankle with only four IMUs, without resorting to any additional tools or predefined movements. The procedure require the sensor placed on the pelvis aligned with walking direction and the way to place the other sensors is easier and without concern for accurate positions.

Even though the sensor system presents limitations, this procedure is suitable to estimate the angular displacements of human joints, especially on the sagittal plane. On this plane the joint maximum possible motion occurs, and it is interesting to mention that recent robotic devices used in gait rehabilitation as exoskeletons act on the limbs to follow trajectories on this plane.

The obtained results are coherent with those found on the literature (BENEDETTI et al., 1998, CUTTI et al. 2010; PALERMO et al., 2014). The experiments allow analyzing characteristics of the individuals in free walking. This procedure also presents the potential to become an alternative to high-cost camera-based systems allowing the possibility of performing the analysis of human gait outside the laboratory, in more realistic scenarios.

Chapter 6. Conclusions and Future Works

6.1. Conclusions

In Chapter 1 of this dissertation, different mobility diseases that affect the human gait were identified. Evidently, when gait patterns are affected by certain pathology, this condition deprives the individual of having an independent development in the community. In this context, recent technologies have been developed to assist patients in rehabilitation and help to restore its motor ability. Regardless of the area of action, either for diagnosis, treatment definition and/or prescription of assistive devices, it has been proved that movement analysis is a helpful tool to evaluate and analyze the motor capacity, since the beginning of the clinical intervention until the assessment of patient's progression and evolution during rehabilitation.

In addition, there is a trend regarding the use of wearable sensors to accomplish the task of movement assessment. The number of devices and commercial solutions based on inertial sensors is increasing, which is driving the development of better fusion algorithms, signal processing and analysis techniques in order to improve accuracy and repeatability of the acquired data.

Defining an appropriated measurement protocol and providing a sensor-to-body calibration procedure is a fundamental problem of the IMU-based gait analysis. Thus, the objective of this M.Sc. dissertation was to develop a calibration algorithm to align the IMUs' local frames with the anatomically defined segment frames in order to estimate joint angular kinematics of ankle, knee and hip.

A brief description of the human gait was presented in Chapter 2 with the aim to identify characteristics that allow defining a gait pattern, initially in healthy subjects. From kinematics, angular displacement of the body segments axes was found as one of the parameters of most interest in movement studies. Thus, in this M.Sc. dissertation an algorithm to calculate the joint angles was implemented.

A general review of the commercial technologies used in capture motion was also presented in Chapter 2. Wearable and non-wearable systems present advantages and disadvantages depending on the application. Optical camera-based systems continue being the gold standard technology to estimate position and orientation of human limbs in motion analyzing research,

considering its high accuracy, walking analysis protocols and standards to place markers, which have been widely accepted by the clinical community.

Nevertheless, higher cost, fixed, complex and time-consuming set-ups and need of a precise placement of markers are some of the principal hampering factors that hinder the use of these optical technologies in routine clinical applications. In conclusion, there is a need of developing systems ease-to-use, more friendly, portables, with relatively lower cost and that can be used in external environments. Specially, because of healthcare is a task projected in future to be performed at home.

Different approaches to accomplish the sensor-to-body alignment also are presented at the end of Chapter 2. However, the proposed procedures present some limitations: difficulty in defining a common reference frame and heading drift when the system is based only on accelerometers and gyroscopes and use of additional tools or devices as cameras. Also, the procedures require predefined user's movements keeping firm postures or maintaining the same orientation between two postures. These movements may not be simple tasks to be performed by subjects with motor disabilities. In conclusion, a novel, simple and fast calibration procedure was proposed in this M.Sc. dissertation to address the problem of body-to-sensor alignment in IMU-based gait analysis. Such procedure provides tridimensional kinematics of hip, knee and ankle with only four IMUs, without resorting to any additional tools or predefined movements.

A static orientation assessment method was presented in Chapter 3 and validated in Chapter 4. This method was performed with the aim to know the initial state of the system and identify the IMUs that present the lower errors. The system presents some limitations, and significant errors were found when comparing the orientation of pairs of sensors and in measuring the same global frame regardless of the orientation in space. This factor may be more critical in analyzing movements in secondary planes (frontal and transverse planes).

The proposed sensor-to-body calibration procedure was simulated and experimentally validated in Chapter 4. The method was tested using a two-semi sphere and goniometer configuration. The aim of this experiment was proving that independent of the position of the sensors on a segment, the sensor-to-segment calibration procedure can estimate the angles imposed by the goniometer. In simulations, the results were as expected, however, in experimental validation, errors were exhibited due to the sensor system limitations.

A method to identify events of human gait was also implemented. Using the angular velocity calculated from the IMU sensor placed on the foot, events, such as heel strike (HS) and toe off (TO), were identified. This method allows separating the gait cycles to further analysis.

An important characteristic of the proposed method is to be able to detect the two events (HS and TO) that define the beginning of the stance and swing phases. The analysis of the moments of occurrence of these events may help to identify problems in the gait pattern.

In addition, an algorithm to detect discrete angular kinematic parameters was developed. These parameters were selected in order to compare the obtained results with those presented by Benedetti et al. (1998). This last study is a complete reference of gait analysis that uses camera-based system. By comparing the information obtained in this dissertation with the literature, it is evident that the angular patterns are coherent and within the intervals established by mean and standard deviations.

The sensor-to-body calibration procedure was tested in five volunteers without gait disabilities in Chapter 5. A sensor placement protocol was proposed, which was able to estimate the joint angular displacements in free walking, fulfilling the main objective of this M.Sc. dissertation.

The obtained results including both signal behavior and the similar intervals at which it occurs are consistent with those presented in the literature. Interestingly, the obtained results presented low standard deviations, which indicates that estimated measurements were consistent across trials.

Characteristics of the individuals in free walking can be analyzed using the proposed procedure. This procedure also presents the potential to become an alternative to camera-based systems allowing the possibility of performing the analysis of human gait outside the laboratory, in more realistic scenarios.

6.2. Contributions

The main contribution of this dissertation was to develop a sensor-to-body calibration procedure in order to resolve the alignment problem using IMUs for gait analysis. The procedure allows estimating the angles of joints without regardless of location IMUs on the segment. The calibration procedure is fast and performed at the beginning of each experiment. Also, the complete system provides a tool easy-to-use, versatile and portable, which can be used in ambulatory and routine clinical applications. Other contributions involve the development of algorithms to detect gait events as heel strike and toe off and discrete angular kinematic parameters. This system uses only four IMU sensors to estimate lower limb joint angles and the result were found coherent with those presented in the literature.

6.3. Publications

The following publications in conferences proceedings were obtained as direct results of this work:

- **VARGAS**, L. S.; ELIAS, A.; FRIZERA NETO, A.; BASTOS, T. Calibration Procedure and Definition of Anatomic References for Gait Analysis Based on Inertial Sensors. In: Proceedings of the 1st International Workshop on Assistive Technology, 2015. Pp. 15-18.
- **VARGAS**, L. S.; ELIAS, A.; FRIZERA NETO, A.; ROCON, E. Body to Sensor Calibration Procedure for Lower Limb Joint Angle Estimation Applied to IMU-based Gait Analysis. In: Anais do XXIV Congresso Brasileiro de Engenharia Biomédica CBEB 2014, 2014. Pp. 777-780.
- BOTELHO, T.; SOPRANI, D.; SCHNEIDER, P.; CARVALHO, C.; **VARGAS**, L.; FRIZERA, A. Uma Proposta de Protocolo de Colocação de Sensores Inerciais Utilizando Alinhamento Virtual para Aplicações em Análise de Movimento de Membros Inferiores. In: Anais do V Encontro Nacional de Engenharia Biomecânica – ENEBI, 2015.

6.4. Future work

The following tasks are indicated as possible future works of this M.Sc. dissertation:

- An investigation on the reliability of the proposed procedure and internal/external validity of the results involving significant number of subjects.
- Testing the procedure in patients with motor disabilities to estimate the benefits of the method in identifying different pathologies.
- Testing the procedure in patients using assistive devices, such as robotic smart walkers and exoskeletons to monitor the patient's evolution.
- Testing the calibration procedure in parallel with optical camera-based systems to perform a comparative study and identify the main benefits and limitations.
- Studying and implementing fusion data algorithm to improve the orientation data accuracy.
- Developing a wearable sensor networks involving inertial sensors and other technologies, such a polymeric optical fiber, improving the fusion data and providing a more robust system to continuous monitoring of patients.

References

ALBARBAR, A.; MEKID, S.; STARR, A. G.; PIETRUSZKIEWICZ, R. **Suitability of MEMS accelerometers for condition monitoring: an experimental study**. Sensors, 8(2), 784–799, 2008.

ALFONSO, M. R. **Desenvolvimento de Sensor MARG para Análise de Movimento**. Dissertação (Mestrado). Universidade Federal do Espírito Santo, 2014.

ALONGE, F.; CUCCO, E.; D'IPPOLITO, F.; PULIZZOTTO, A. **The use of accelerometers and gyroscopes to estimate hip and knee angles on gait analysis**. Sensors, 14(5), 8430–8446, 2014.

BAAN, H.; DUBBELDAM, R.; NENE, A. V.; VAN DE LAAR, M. F. J. **Gait analysis of the lower limb in patients with rheumatoid arthritis: a systematic review**. Seminars in Arthritis and Rheumatism, 41(6), 768–788, 2012.

BAE, J.; TOMIZUKA, M. **A tele-monitoring system for gait rehabilitation with an inertial measurement unit and a shoe-type ground reaction force sensor**. Mechatronics, 23(6), 646–651, 2013.

BAKER, R. **Gait analysis methods in rehabilitation**. Journal of Neuroengineering and Rehabilitation, 3, 4, 2006.

BAKER, R.; RODDA, J. **All you ever wanted to know about the conventional gait model but were afraid to ask.** (Hugh Williamson Gait Laboratory, Ed.). Melbourne: Women and Children's Health, 2003.

BENEDETTI, M. G.; CATANI, F.; LEARDINI, A.; PIGNOTTI, E.; GIANNINI, S. **Data management in gait analysis for clinical applications**. Clinical Biomechanics, 13(3), 204–215, 1998.

BENEDETTI, M. G.; D'APOTE, G.; FACCIOLI, S.; COSTI, S.; FERRARI, A. **Equinus foot classification in cerebral palsy: an agreement study between clinical and gait analysis assessment**. European Journal of Physical and Rehabilitation Medicine, 47(2), 213–221, 2011.

BIOMECHANICAL SOLUTIONS. **Motion Anaylsis**, Biomechanical Products, 2015. Available at: http://bme.gr/index.php?option=com_content&view=article&id=42&Itemid=223.

BIOMETRICS LTD. **Goniometer and Torsiometer**. SG series, 2015 Available at: http://www.biometricsltd.com/gonio.htm.

BTS BIOENGINEERING. **BTS G-WALK: Wireless Digital Gait Analysis System**, 2012a Available at: http://www.btsbioengineering.com/wp-content/uploads/2012/07/BTS_GWALK_UK_A4.pdf.

BTS BIOENGINEERING. **BTS G-WALK: A new approach to walking analysis. White Paper,** 2012b. Available at: http://www.btsbioengineering.com/wp-content/uploads/2012/07/BTSWP_G-WALK-0514_UK.pdf.

BTS BIOENGINEERING. **BTS SMART-DX**, 2014 Available at: http://www.btsbioengineering.com/wp-content/uploads/2014/02/BTSBRO_SMART-DX-1113UK_LQ.pdf.

BTS BIOENGINEERING. **BTS GAITLAB**, 2015 Available at: http://www.btsbioengineering.com/products/integrated-solutions/bts-gaitlab/.

BOFFANO, M.; BERTOLO, C.; AGOSTINI, V.; CARLONE, M.; KNAFLITZ, L.; MARCANTONIO, L.; PIANA, R. **Limb reconstruction with knee mega-prosthesis in patients with distal femir primary tumors: gait analysis and alignment evaluation**. Proceedings of 27th Annual Meeting of the European Musculo-Skeletal Oncology Society, 67, 2014.

BÔRTOLE, M. **Robotic exoskeleton with an assist-as-needed control strategy for gait rehabilitation after stroke**. Univerdidad Carlos III de Madrid, 2014.

BOVI, G.; RABUFFETTI, M.; MAZZOLENI, P.; FERRARIN, M. **A multiple-task gait analysis approach: kinematic, kinetic and EMG reference data for healthy young and adult subjects**. Gait & Posture, 33(1), 6–13, 2011.

BRODIE, M. A.; WALMSLEY, A.; PAGE, W. **The static accuracy and calibration of inertial measurement units for 3D orientation**. Computer Methods in Biomechanics and Biomedical Engineering, 11(6), 641–648 2008.

CAPPOZZO, A.; CATANI, F.; DELLA CROCE, U.; Leardini, A. **Position and orientation in space of bones during movement: anatomical frame definition and determination**. Clinical Biomechanics, 10(4), 171–178, 1995.

CARSE, B.; MEADOWS, B.; BOWERS, R.; ROWE, P. **Affordable clinical gait analysis: an assessment of the marker tracking accuracy of a new low-cost optical 3D motion analysis system**. Physiotherapy, 99(4), 347–351, 2013.

CELESTINO, M. L.; GAMA, G. L.; BARELA, A. M. F. **Gait characteristics of children with cerebral palsy as they walk with body weight unloading on a treadmill and over the ground**. Research in Developmental Disabilities, 35(12), 3624–3631, 2014.

CESERACCIU, E.; SAWACHA, Z.; COBELLI, C. **Comparison of markerless and marker-based motion capture technologies through simultaneous data collection during gait: proof of concept**. PLoS ONE, 9(3), 1–7, 2014.

CIFUENTES, C.; BRAIDOT, A.; RODRIGUEZ, L.; FRISOLI, M.; SANTIAGO, A.; FRIZERA, A.; **Development of a wearable ZigBee sensor system for upper limb rehabilitation robotics**. In Biomedical Robotics and Biomechatronics (BioRob), 2012 4th IEEE RAS & EMBS International Conference on, 1989-1994, 2012

CIMOLIN, V.; GALLI, M.; VIMERCATI, S. L.; ALBERTINI, G. **Use of the gait deviation index for the assessment of gastrocnemius fascia lengthening in children with cerebral palsy**. Research in Developmental Disabilities, 32(1), 377–381, 2011.

CLARK, R. A.; PUA, Y. H.; BRYANT, A. L.; HUNT, M. A. **Validity of the Microsoft Kinect for providing lateral trunk lean feedback during gait retraining**. Gait & Posture, 38(4), 1064–1066, 2013.

COLLAZOS, C. A.; ARGOTHY, R. E. **Physical modeling of normal and pathological gait using identification of kinematic parameters.** International Journal of Biology and Biomedical Engineering, 8, 179–183, 2014.

COMTEMPLAS GMBH. T**EMPLO Clinical Gait Analysis**, 2015. Available at: http://www.contemplas.com/clinical_gait_analysis.aspx

CUTTI, A. G.; FERRARI, A.; GAROFALO, P.; RAGGI, M.; CAPPELLO, A.; FERRARI, A. **"Outwalk": a protocol for clinical gait analysis based on inertial and magnetic sensors.** Medical and Biological Engineering and Computing, 48(1), 17–25, 2010.

CUTTI, A. G.; GIOVANARDI, A.; ROCCHI, L.; DAVALLI, A.; SACCHETTI, R. **Ambulatory measurement of shoulder and elbow kinematics through inertial and magnetic sensors**. Medical and Biological Engineering and Computing, 46(2), 169–178, 2008.

DAVIS, R. B.; ÕUNPUU, S.; TYBURSKI, D.; GAGE, J. R. **A gait analysis data collection and reduction technique**. Human Movement Science, 10(5), 575–587, 1991.

DE MITS, S.; SEGERS, V.; WOODBURN, J.; ELEWAUT, D.; DE CLERCQ, D.; ROOSEN, P. **A clinically applicable six-segmented foot model.** Journal of Orthopaedic Research, 30(4), 655–661, 2012.

DE ROSSI, S. M. M.; VITIELLO, N.; LENZI, T.; RONSSE, R.; KOOPMAN, B.; PERSICHETTI, A.; CARROZZA, M. C. **Sensing pressure distribution on a lower-limb exoskeleton physical human-machine interface**. Sensors, 11(1), 207–227, 2011.

DEPARTAMENTO ADMINISTRATIVO NACIONAL DE ESTADÍSTICA – DANE. **Censo General 2005**. Población Adulta Mayor, 2005. Available at: https://www.dane.gov.co/censo/files/presentaciones/poblacion_adulto_mayor.pdf

DERAWI, M. O.; ALI, H.; CHEIKH, F. A. **Gait recognition using time-of-flight sensor**. BIOSIG, (September), 187–194, 2011.

DI MARCO, R.; ROSSI, S.; PATANÈ, F.; CAPPA, P. **Technical quality assessment of an optoelectronic system for movement analysis**. Journal of Physics: Conference Series, 588(1), 2015.

DIEBEL, J. **Representing attitude: Euler angles, unit quaternions, and rotation vectors**. Matrix, 58, 1–35, 2006.

FAVRE, J.; AISSAOUI, R.; JOLLES, B. M.; DE GUISE, J. A.; AMINIAN, K. **Functional calibration procedure for 3D knee joint angle description using inertial sensors**. Journal of Biomechanics, 42(14), 2330–2335. 2009.

FAVRE, J.; JOLLES, B. M.; AISSAOUI, R.; AMINIAN, K. **Ambulatory measurement of 3D knee joint angle**. Journal of Biomechanics, 41(5), 1029–1035, 2008.

FERRARI, A.; CUTTI, A. G.; GAROFALO, P.; RAGGI, M.; HEIJBOER, M.; CAPPELLO, A.; DAVALLI, A. **First in vivo assessment of "Outwalk": a novel protocol for clinical gait analysis based on inertial and magnetic sensors**. Medical and Biological Engineering and Computing, 48(1), 1–15, 2010.

FREED, A.; CHAN, A. D. C.; LEMAIRE, E. D.; PARUSH, A. **Wearable EMG analysis for rehabilitation (WEAR) - Surface electromyography in clinical gait analysis**. Proceedings of 2011 IEEE International Symposium on Medical Measurements and Applications, 2011.

FULLER, D. A.; KEENAN, M. A. E.; ESQUENAZI, A.; WHYTE, J.; MAYER, N. H.; FIDLER-SHEPPARD, R. **The impact of instrumented gait analysis on surgical planning: treatment of spastic equinovarus deformity of the foot and ankle**. Foot and Ankle International, 23(8), 738–743, 2002.

GALINSKI, D.; DEHEZ, B. **Evaluation of initialization procedures for estimating upper limb kinematics with MARG sensors**. Proceedings of the IEEE RAS and EMBS International Conference on Biomedical Robotics and Biomechatronics, (1), 1801–1806, 2012.

GEERTSEN, S. S.; KIRK, H.; LORENTZEN, J.; JORSAL, M.; JOHANSSON, C. B.; NIELSEN, J. B. **Impaired gait function in adults with cerebral palsy is associated with reduced rapid force generation and increased passive stiffness**. Clinical Neurophysiology, 2015.

GIL-AGUDO, A.; PÉREZ, S.; FORNER, A.; PÉREZ, E.; CRESPO, B.; DEL AMA, A. **Gait kinematic analysis in patients with a mild form of central cord syndrome**. Journal of Neuroengineering and Rehabilitation, 8(1), 7, 2011.

GIPSMAN, A.; RAUSCHERT, L.; DANESHVAR, M.; KNOTT, P. **Evaluating the reproducibility of motion analysis scanning of the spine during walking.** Advances in Medicine, 2014, 9, 2014.

GRAGG, J.; CLOUTIER, A.; YANG, J. **Optimization-based posture reconstruction for digital human models**. Computers and Industrial Engineering, 66(1), 125–132, 2013.

GROOD, E. S.; SUNTAY, W. J. **A joint coordinate system for the clinical description of three-dimensional motions: application to the knee.** Journal of Biomechanics Engineering, 105(2), 136–144, 1983.

HAMILL, J.; KNUTZEN, K. M. **Biomechanical basis of human movement.** Medicine & Science in Sports & Exercise (3rd ed.), 2009.

HANSON, A. J. **Visualizing quaternions.** Elsevier, 2006.

HARISH, K. M.; GALLACHER, B. J.; BURDESS, J. S.; NEASHAM, J. A. **Simple parametric resonance in an electrostatically actuated microelectromechanical gyroscope: theory and experiment**. Journal of Mechanical Engineering Science, 222(1), 43–52, 2008.

HARTMANN, M.; KREUZPOINTNER, F.; HAEFNER, R.; MICHELS, H.; SCHWIRTZ, A.; HAAS, J. P. **Effects of juvenile idiopathic arthritis on kinematics and kinetics of the lower extremities call for consequences in physical activities recommendations.** International Journal of Pediatrics, 2010.

HERNÁNDEZ-CASTILLO, A.; ÁLVAREZ-CAMACHO, M.; SÁNCHEZ-ARÉVALO, F. M. **Protocolo para el análisis funcional de prótesis para pacientes con amputación parcial de pie.** Revista Mexicana de Ingeniería Biomédica, 34(1), 97–107, 2013.

HSU, A. L.; TANG, P. F.; JAN, M. H. **Analysis of impairments influencing gait velocity and asymmetry of hemiplegic patients after mild to moderate stroke.** Archives of Physical Medicine and Rehabilitation, 84(8), 1185–1193, 2003.

HUNT, M. A.; BIRMINGHAM, T. B.; GIFFIN, J. R.; JENKYN, T. R. A**ssociations among knee adduction moment, frontal plane ground reaction force, and lever arm during walking in patients with knee osteoarthritis.** Journal of Biomechanics, 39(12), 2213–2220, 2006.

INSTITUTO BRASILEIRO DE GEOGRAFIA E ESTATÍSTICA. - IBGE. **Censo Demográfico 2010**, 2010. Available at: http://www.ibge.gov.br/home/estatistica/populacao/censo2010/ default_sinopse.shtm

JURMAN, D.; JANKOVEC, M.; KAMNIK, R.; TOPIC, M. **Calibration and data fusion solution for the miniature attitude and heading reference system**. Sensors and Actuators, 138(2), 411–420, 2007.

KADABA, M. P. **Repeatability of kinematic, kinetic, and electromyographic data in normal adult gai**t. Annals of Allergy, 66(1), 3, 1989.

KADABA, M. P.; RAMAKRISHNAN, H. K.; WOOTTEN, M. E. **Measurement of lower extremity kinematics during level walking**. Journal of Orthopaedic Research, 8(3), 383–392, 1990.

KAVANAGH, J. J.; BARRETT, R. S.; MORRISON, S. **Upper body accelerations during walking in healthy young and elderly men.** Gait & Posture, 20(3), 291–298, 2004.

KAVANAGH, J. J.; MORRISON, S.; JAMES, D. A.; BARRETT, R. **Reliability of segmental accelerations measured using a new wireless gait analysis system**. Journal of Biomechanics, 39(15), 2863–2872, 2006.

KIRSHBLUM, S. C.; BURNS, S. P.; BIERING-SORENSEN, F. B.; DONOVAN, W.; GRAVES, D. E.; JHA, A.; WARING, W. **International standards for neurological**

classification of spinal cord injury. The Journal of Spinal Cord Medicine, 43(6), 535–546, 2011.

KUMAR, N.; PANKAJ, D.; MAHAJAN, A.; KUMAR, A.; SOHI, B. S. **Evaluation of normal gait using electro-goniometer**. Journal of Scientific and Industrial Research, 68(8), 696–698, 2009.

LANGFELDER, G.; BUFFA, C.; FRANGI, A.; TOCCHIO, A.; LASALANDRA, E.; LONGONI, A. **Z -axis magnetometers for MEMS inertial measurement units: using an industrial process**. IEEE Transactions on Industrial Electronics, 60(9), 3983–3990.2013.

LAUDANSKI, A.; BROUWER, B.; LI, Q. M**easurement of lower limb joint kinematics using inertial sensors during stair ascent and descent in healthy older adults and stroke survivors**. Journal of Healthcare Engineering, 4(4), 555–576, 2013.

LUINGE, H. J.; VELTINK, P. H. **Measuring orientation of human body segments using miniature gyroscopes and accelerometers.** Medical and Biological Engineering and Computing, 43(2), 273–282, 2005.

LUINGE, H. J.; VELTINK, P. H.; BATEN, C. T. M. **Ambulatory measurement of arm orientation**. Journal of Biomechanics, 40(1), 78–85, 2007.

MANCA, M.; LEARDINI, A.; CAVAZZA, S.; FERRARESI, G.; MARCHI, P.; ZANAGA, E.; BENEDETTI, M. G. **Repeatability of a new protocol for gait analysis in adult subjects**. Gait & Posture, 32(2), 282–284, 2010.

MELIM R. **Desenvolvimento de Sistema de Análise da Marcha Humana Utilizando Sensores Inerciais e Câmera de Profundidade**. Dissertação (Mestrado). Universidade Federal do Espírito Santo, 2013.

MERCHÁN-BAEZA, J. A.; GONZÁLEZ-SÁNCHEZ, M.; CUESTA-VARGAS, A. I. **Reliability in the parameterization of the functional reach test in elderly stroke patients: a pilot study.** BioMed Research International, 2014, 8–11, 2014.

METSIS, V.; JANGYODSUK, P.; ATHITSOS, V.; IVERSEN, M.; MAKEDON, F. **Computer aided rehabilitation for patients with rheumatoid arthritis.** Proceedings of 2013 International Conference on Computing, Networking and Communications, 97–102, 2013.

MOHAMED, A. A.; BABA, J.; BEYEA, J.; LANDRY, J.; SEXTON, A.; MCGIBBON, C. A. **Comparison of strain-gage and fiber-optic goniometry for measuring knee kinematics during activities of daily living and exercise.** Journal of Biomechanical Engineering, 134(8), 084502, 2012.

MONTERO-ODASSO, M.; CASAS, A.; HANSEN, K. T.; BILSKI, P.; GUTMANIS, I.; WELLS, J. L.; BORRIE, M. J. **Quantitative gait analysis under dual-task in older people with mild cognitive impairment: a reliability study.** Journal of Neuroengineering and Rehabilitation, 6, 35, 2009.

MOTION WORKSHOP. **Shadow Wireless. Motion Version 2.2**, 2015. Available at: http://www.motionshadow.com/manual/Shadow%20Wireless.pdf

MURO-DE-LA-HERRAN, A; GARCÍA-ZAPIRAIN, B.; MÉNDEZ-ZORRILLA, A. **Gait analysis methods: an overview of wearable and non-wearable systems, highlighting clinical applications**. Sensors, 14(2), 3362–3394, 2014.

NGUYEN, H. A.; MEUNIER, J. **Gait analysis from video: camcorders vs. kinect.** Image Analysis and Recognition, 66–73, 2014.

NISHIDA, M.; WATANABE, K.; MATSUMOTO, M.; TOYAMA, Y.; NAGURA, T. **Asymmetric trunk kinematics during gait is seen between concave side and convex side in adolescent idiopathic scoliosis**. Scoliosis, 10(Suppl 1), 2015.

O'DONOVAN, K. J.; KAMNIK, R.; O'KEEFFE, D. T.; LYONS, G. M. **An inertial and magnetic sensor based technique for joint angle measurement**. Journal of Biomechanics, 40(12), 2604–2611, 2007.

OLIVARES, A. L.; SAGARÓ, R.; RODRÍGUEZ, C.; REYES, M. A.; DÍAZ, C. **Evaluación integral de prótesis ortopédicas transfemorales**. Ingenierías, 13(47), 17–24, 2010.

OLIVARES, A. L.; VÁZQUEZ, L. B.; NOVO, C. D.; CASTILLO, L. G.; ZAMORA, R. S. **Análisis de la funcionabilidad de prótesis ortopédicas transfemorales**. Revista Cubana de Ortopedia Y Traumatología, 25(2), 102–116, 2011.

OLSEN, E.; ANDERSEN, P. H.; PFAU, T. **Accuracy and precision of equine gait event detection during walking with limb and trunk mounted inertial sensors**. Sensors, 12(6), 8145–8156, 2012.

PALERMO, E.; ROSSI, S.; MARINI, F.; PATANÈ, F.; CAPPA, P. **Experimental evaluation of accuracy and repeatability of a novel body-to-sensor calibration procedure for inertial sensor-based gait analysis**. Measurement: Journal of the International Measurement Confederation, 52(1), 145–155, 2014.

PARVATHY, S. S.; MASOCHA, W. **Gait analysis of C57BL/6 mice with complete Freund's adjuvant-induced arthritis using the CatWalk system**. BMC Musculoskeletal Disorders, 14(1), 14, 2013.

PASTORINO, M.; ARREDONDO, M. T.; CANCELA, J.; GUILLEN, S. **Wearable sensor network for health monitoring: the case of Parkinson disease**. Journal of Physics: Conference Series, 450, 2013.

PICERNO, P.; CEREATTI, A.; CAPPOZZO, A. **Joint kinematics estimate using wearable inertial and magnetic sensing modules**. Gait & Posture, 28(4), 588–595, 2008.

PICERNO, P.; CEREATTI, A.; CAPPOZZO, A. **A spot check for assessing static orientation consistency of inertial and magnetic sensing units**. Gait & Posture, 33(3), 373–378, 2011.

POLHEMUS. **G4 User Manual,** 2013 Available at: http://polhemus.com/_assets/img/G4_User_Manual_URM10PH238-D.pdf

QUALISYS. **Gait analysis and Rehabilitation**. Efective solutions for gait anaylsis, 2015. Available at: http://www.qualisys.com/applications/biomechanics/gait-analysis-and-rehabilitation/

QIU, S.; HOU, J.; YANG, Y.; JI, R.; HU, H.; WANG, Z. **Ambulatory estimation of 3D walking trajectory and knee joint angle using MARG Sensors**. Proceedings of International Conference on Innovative Computing Communication Technology, 2014.

RABUFFETTI, M.; CRENNA, P. **A modular protocol for the analysis of movement in children**. Gait & Posture, 20, S77–S78, 2004.

RODRÍGUEZ-MARTÍN, D.; PÉREZ-LÓPEZ, C.; SAMÀ, A.; CABESTANY, J.; CATALÀ, A. **A wearable inertial measurement unit for long-term monitoring in the dependency care area**. Sensors, 13(10), 14079–14104, 2013.

ROERDINK, M.; COOLEN, B.; CLAIRBOIS, B. E.; LAMOTH, C. J. C.; BEEK, P. J. **Online gait event detection using a large force platform embedded in a treadmill**. Journal of Biomechanics, 41(12), 2628–2632, 2008.

ROETENBERG, D.; BATEN, C. T. M.; VELTINK, P. H. **Estimating body segment orientation by applying inertial and magnetic sensing near ferromagnetic materials**. IEEE Transactions on Neural Systems and Rehabilitation Engineering, 15(1), 469–471, 2007.

ROETENBERG, D.; LUINGE, H. J.; BATEN, C. T. M.; VELTINK, P. H. **Compensation of magnetic disturbances improves inertial and magnetic sensing of human body segment orientation.** IEEE Transactions on Neural Systems and Rehabilitation Engineering, 13(3), 395–405, 2005.

SABATINI, A. M.; MARTELLONI, C.; SCAPELLATO, S.; CAVALLO, F. **Assessment of walking features from foot inertial sensing**. Biomedical Engineering, IEEE Transactions, 52(3), 486–494, 2005.

SABATINI, A. M. **Quaternion-based extended Kalman filter for determining orientation by inertial and magnetic sensing**. IEEE Transactions on Biomedical Engineering, 53(7), 1346–1356, 2006.

SATO, T. O.; HANSSON, G. A.; COURY, H. J. C. G. **Goniometer crosstalk compensation for knee joint applications**. Sensors, 10, 9994–10005, 2010.

SCIAVICCO, L.; SICILIANO, B. **Modelling and control of robot manipulators** (2nd ed.). Springer, 2000.

SENDEN, R.; SAVELBERG, H. H. C. M.; GRIMM, B.; HEYLIGERS, I. C.; MEIJER, K. **Accelerometry-based gait analysis: an additional objective approach to screen subjects at risk for falling**. Gait & Posture, 36(2), 296–300, 2012.

SIMON, S. R. **Quantification of human motion: gait analysis - benefits and limitations to its application to clinical problems**. Journal of Biomechanics, 37(12), 1869–1880, 2004.

SINGH, R. **Effect of combined training program on gait parameters after bilateral total hip arthroplasty: a case study**. Journal of Novel Physiotherapies, 2(07), 2–4, 2012.

STOKDIJK, M.; BIEGSTRAATEN, M.; ORMEL, W.; DE BOER, Y. A.; VEEGER, H. E. J.; ROZING, P. M. **Determining the optimal flexion-extension axis of the elbow in vivo - a study of interobserver and intraobserver reliability**. Journal of Biomechanics, 33(9), 1139–1145, 2000.

STT SYSTEMS. **STT-IBS WIRELESS INERTIAL SENSOR AND DEVELOPER'S SDK**, 2013. Available at: http://www.stt-systems.com/downloads/stt-ibs/STT_IBS_brochure_en.pdf

SUGIYAMA, D.; NISHIMURA, K.; TAMAKI, K.; TSUJI, G.; NAKAZAWA, T.; MORINOBU, A.; KUMAGAI, S. **Impact of smoking as a risk factor for developing rheumatoid arthritis: a meta-analysis of observational studies**. Annals of the Rheumatic Diseases, 69(1), 70–81, 2010.

TADANO, S.; TAKEDA, R.; MIYAGAWA, H. T**hree dimensional gait analysis using wearable acceleration and gyro sensors based on quaternion calculations.** Sensors, 13(7), 9321–9343, 2013.

TAO, W.; LIU, T.; ZHENG, R.; FENG, H. **Gait analysis using wearable sensors**. Sensors, 12(2), 2255–2283, 2012.

TECHNAID. **Manual de Usuario Tech MCS V3**. Revision: 8 de Agosto 2014.

TIEN, I.; GLASER, S. D.; AMINOFF, M. J. **Characterization of gait abnormalities in Parkinson's disease using a wireless inertial sensor system**. 2010 Annual International Conference of the IEEE Engineering in Medicine and Biology Society, 3353–3356, 2010.

TONG, K.; GRANAT, M. H. **A practical gait analysis system using gyroscopes**. Medical Engineering and Physics, 21(2), 87–94, 1999.

UNITED NATIONS, Department of Economic and Social Affairs, Population Division. **World Population Ageing 2013**. United Nations: New York, NY, USA, 2013. Available at:http://www.un.org/en/development/desa/population/publications/pdf/ageing/WorldPopulationAgeing2013.pdf.

VAN DEN NOORT, J. C.; FERRARI, A.; CUTTI, A. G.; BECHER, J. G.; HARLAAR, J. **Gait analysis in children with cerebral palsy via inertial and magnetic sensors**. Medical & Biological Engineering & Computing, 51(4), 377–86, 2013.

VAUGHAN, C. L.; DAVIS, B. L.; O'CONNOR, J. C. **Dynamics of human gait** (2nd ed., Vol. 731). Cape Town: Kiboho, 2013.

VELTINK, P. H.; DE ROSSI, D. **Conversations in BME**. IEEE Engineering in Medicine and Biology Magazine, (June), 37–43, 2010.

VICON. **Bonita B10**, 2015. Available at: http://www.vicon.com/products/camera-systems/bonita

WHITTLE, M. W. **Gait analysis: an introduction** (4th ed.). Butterworth Heinemann, 2007.

WINTER, D. A. **Biomechanics and motor control of human movement.** Motor Control. John Wiley & Sons, 2009.

WOLTRING, H. J. **Data processing and error analysis.** (A. Cappozzo, N. Berme, & Biomechanics of Human Movement, Eds.). Worthington: Bertec Corporation, 1990.

WREN, T. A. L.; KALISVAART, M. M.; GHATAN, C. E.; RETHLEFSEN, S. A.; HARA, R.; SHENG, M.; KAY, R. M. **Effects of preoperative gait analysis on costs and amount of surgery**. Journal of Pediatric Orthopedics, 29(6), 558–563, 2009.

WU, G.; SIEGLER, S.; ALLARD, P.; KIRTLEY, C.; LEARDINI, A.; ROSENBAUM, D.; STOKES, I. **ISB RECOMMENDATION ON DEFINITIONS OF JOINT COORDINATE SYSTEM OF VARIOUS JOINTS FOR THE REPORTING OF HUMAN JOINT MOTION - PART I: ANKLE, HIP AND SPINE**. JOURNAL OF BIOMECHANICS, 35(4), 20, 2002.

XUE, Z.; MING, D.; SONG, W.; WAN, B.; JIN, S. **Infrared gait recognition based on wavelet transform and support vector machine**. Pattern Recognition, 43(8), 2904–2910, 2010.

XSENS TECHNOLOGIES. **MTw Development Kit. Wireless Motion Trackers**, 2014. Available at: https://www.xsens.com/wp-content/uploads/2013/11/mtw-leaflet.pdf

YANG, C. C.; HSU, Y. L. **A review of accelerometry-based wearable motion detectors for physical activity monitoring**. Sensors, 10(8), 7772–7788, 2010.

YANG, C. C.; HSU, Y. L.; SHIH, K. S.; LU, J. M. **Real-time gait cycle parameter recognition using a wearable accelerometry system**. Sensors, 11(8), 7314–7326, 2011.

YANG, S.; KONG, L. **Research on characteristic extraction of human gait**. Proceedings of 3rd International Conference on Bioinformatics and Biomedical Engineering, 2–5, 2009.